OREGON HEALTH & SCIENCE UNIVERSITY

SCHOOL OF MEDICINE—GRADUATE STUDIES

THE ECOPHYSIOLOGICAL DRIVERS OF PRODUCTION AND CELLULAR FUNCTION OF THE CYANOBACTERIAL NEUROTOXIN *B*-*N*-METHYLAMINO-L-ALANINE IN BUOYANT FRESHWATER CYANOBACTERIA

By

Stuart W. Dyer

A DISSERTATION

Presented to the Institute of Environmental Health
and the Oregon Health & Science University
School of Medicine
in partial fulfillment of
the requirements for the degree of

Doctor of Philosophy

March 2019

TABLE OF CONTENTS

List of figures

List of tables

List of abbreviations

- Ψ_s: cellular solute potential
- π: osmotic pressure
- ε: Young's elastic modulus of cell mechanics
- aaRS: aminoacyl-tRNA synthetase
- AD: Alzheimer's disease
- AEG: N-(2-Aminoethyl)glycine—an isomer of BMAA
- ALS: amyotrophic lateral sclerosis
- AMPA: a-amino-3-hydroxy-5-methyl-4-isoxazolepropionic acid
- BMAA: β-N-methylamino-L-alanine
- CCMs: carbon concentrating mechanisms
- CCP: critical collapse pressure—an applied force associated with the mechanical failure of GVs, and for which the rate of GV collapse is the greatest
- Chl-a: chlorophyll-a
- CLSM: confocal laser scanning microscopy/micrographs
- CTD: conductivity, temperature, and depth
- CyanoHABs: HABs dominated by one or more species of cyanobacteria
- Cyanotoxins: cyanobacterial toxins—atypical molecules and peptides produced by cyanobacteria that elicit toxic effects in other organisms
- DAB: 2,4-Diaminobutyric acid—an isomer of BMAA
- DAP: 2,3-Diaminopropionic acid
- DIC: differential interference contrast
- DNS: dansyl moiety
- DVM: diel vertical migration
- EPA: Environmental Protection Agency
- EPS: extracellular polymeric substances
- ETC: electron transport chain
- FTIR: Fourier-transform infrared
- GOE: Great Oxidation Event
- GOGAT: glutamine oxoglutarate aminotransferase

- GS: glutamine synthase
- GV: gas vesicle
- GVP: gas vesicle protein
- HAB: Harmful Algal Bloom
- HPLC: high performance liquid chromatography
- HPMA: 2-Hydroxypropyl methacrylate
- IR: infrared
- LED: light-emitting diode
- Lp: hydraulic conductivity of the cell surface
- MALDI-TOF: matrix-assisted laser desorption/ionization, time-of-flight
- mGluR5: metabotropic glutamate receptor 5
- MS/MS: tandem mass spectrometry
- MS: mass spectrometry
- NFTs: neurofibrillary tangles
- NMDA: N-methyl-D-aspartate
- NMR: nuclear magnetic resonance
- NTU: nephelometric turbidity units
- PC: phycocyanin
- PDC: Parkinsonism-dementia complex
- Pe: mean effective CCP of GVs in turgid cells
- PE: phycoerythrin
- psi: pounds per square inch—1 psi = 6.895 kPa
- PST: pressure sensitive turbidity, the integrand of turbidity as a function of pressure with respect to pressure
- Pt: turgor pressure
- R2: coefficient of determination for regression fittings
- RFU: relative fluorescence units
- S: standard error about the mean for regression fittings
- SD: standard deviation about a mean
- SE: propagated standard error of replicate measurements

- TEM: transmission electron microscopy
- UV-B: ultraviolet radiation with a wavelength of 280-320 nm
- UVR: ultraviolet radiation

Abstract

In recent decades, cyanobacteria-dominated Harmful Algal Blooms (cyanoHABs) have increased in regularity and persistence, leading to increased concerns over water quality and human health. The buoyant cyanobacteria that form cyanoHABs are the main producers of cyanobacterial toxins (cyanotoxins), and the biochemical role of the well-documented cyanotoxins (e.g., microcystin and saxitoxin) is a focus of ongoing research, as identifying function is a prerequisite to enumerating the ecological drivers of toxin production. The atypical amino acid, β-*N*-methylamino-L-alanine (BMAA), diverges from other cyanotoxins in that it lacks acute toxicity, and as such, has received comparatively less attention from scientists and regulatory agencies. However, mounting evidence suggests that environmental and food web exposure to BMAA is causal to the increased incidence of a histopathologically distinct form of Alzheimer's disease (AD) and/or amyotrophic lateral sclerosis/Parkinsonism-dementia complex (ALS/PDC) observed in multiple geographically isolated populations. As BMAA is the only cyanotoxin thus far detected in axenic cultures of representative species from all five cyanobacteria "Orders," the compound may play a fundamental role within the canonical cyanobacterial metabolon, warranting investigation into its metabolic function. To date, conclusive evidence of an ecological function, biosynthetic pathway, or environmental driver of production has not been presented for BMAA.

This work seeks to address gaps in our understanding of the environmental drivers of production and the ecophysiological role of BMAA within buoyant freshwater cyanobacteria. The first objective is to develop a more robust method for the quantification and disambiguation of BMAA from its structural isomers, N-(2-Aminoethyl)glycine (AEG), and 2,4-Diaminobutyric acid (DAB), within complex biological matrices via dansyl derivatization and HPLC-MS/MS detection. The second and third objectives address the ecophysiological role BMAA plays in

controlling buoyancy, cellular aggregation, and vertical migration in buoyant freshwater cyanobacteria—necessitating the design and development of an automated pressure nephelometer for assaying gas vesicle (GV) physiomechanical properties. The final objective is to investigate the relationship between BMAA prevalence and cyanoHAB population dynamics and bloom succession in a natural setting.

Validation of the HPLC-MS/MS method for BMAA quantification and implementation using environmental samples is demonstrated, advancements in the pressure nephelometry measurement allowing for species delineation of buoyant cyanobacteria in mixed microbial assemblages are expounded on, and evidence is presented from laboratory culture studies using *Microcystis aeruginosa* PCC7806, and environmental time series measurements from a seasonally recurrent freshwater cyanoHAB dominated by *Microcystis* sp. that BMAA is involved in the regulation of bloom dynamics. We demonstrate decreased GV critical collapse pressure (CCP) in cyanobacteria and increased colony formation due to BMAA, in both laboratory culture experiments and environmental HAB settings, and correlate these adaptations with enhanced nutrient scavenging efficiency and the mitigation of photooxidative stressors encountered during diel vertical migration (DVMs) cycles. Further, we propose that a population wide decrease in CCP due to BMAA culminates in bloom collapse when the hydrostatic pressure experienced during DVMs exceeds the CCP of the dominant gas vacuolate populations. Commentary on a proposed mechanism for the observed decrease in CCP due to BMAA is given and environmental factors proposed to drive BMAA production are presented. This work advances our understanding of public health exposure risks to BMAA, presents a new methodology for HAB monitoring and the mitigation of threats from cyanoHABs, and contributes to a more detailed understanding of the ecophysiology of freshwater cyanobacteria.

1. Introduction

1.1 Overview and significance of cyanobacteria

1.1.1 Evolutionary history and adaptive radiation of Cyanobacteria

Modern cyanobacteria are photosynthetic prokaryotes with evolutionary roots that extend back to the origins of photosynthesis in Earth's early history (Brocks et al., 1999). Morphological, geochemical, and isotopic studies of fossilized filamentous microbes found in rock samples from Pilbara craton, Western Australia, indicate that phototrophy arose in, and descended from, procyanobacteria approximately 3.5 billion years ago (Altermann & Kazmierczak, 2003). Photosynthetic oxygen production led to Earth's transition away from a reducing atmosphere and eventually to a climate that supports aerobic respiration (Bekker et al., 2004). It is likely that photosynthesis in modern cyanobacteria (Figure 1.1), first arose through vertical gene transfer from these early procyanobacteria, with the core metabolism of extant cyanobacteria having retained genes and proteins that evolved during the transition from reductive to oxidative environmental conditions (Nozaki et al., 2004; Schirrmeister et al., 2012).

Owing to their extensive evolutionary history and genetic malleability, cyanobacteria as a group possess relatively sophisticated life history strategies, including recent evidence suggesting the potential for lithoautotrophic metabolism—harkening to their ancient origins (Puente-Sanchez et al., 2018). Evolutionary radiation of cyanobacteria is evident in their ubiquitous niche occupation across aquatic, terrestrial, and subterranean ecosystems, their existence as free living cells and colonies, and their role as symbionts within multiple host systems (Stucken et al., 2010; Kuo-Dahab et al., 2018). Conservative estimates attribute more than 25% of global primary production to cyanobacteria, as well as diverse ecosystem functions

including their dominant role in the formation and maintenance of cryptobiotic crusts and as the primary source of new nitrogen to the oligotrophic oceans (Flombaum et al., 2013).

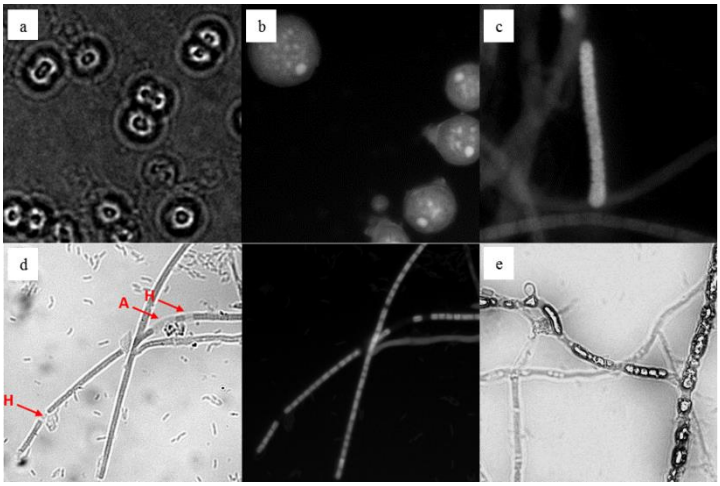

Figure 1.1*:* Due to the overwhelming genomic similarity between cyanobacteria species, functional classifications are regularly employed and are frequently based on morphotype. The five "Orders," of cyanobacteria based on morphotypes include: (I) unicellular or nonfilamentous, reproducing via binary fission—e.g. *Microcystis* sp.; (II) unicellular or nonfilamentous, reproducing via multiple fission, or multiple+binary fission—e.g. *Stanieria* sp.; (III) uniseriate, unbranched, undifferentiated trichomes, reproducing via binary fission in one plane—e.g. *Pseudanabaena* sp.; (IV) uniseriate, unbranched trichomes, reproducing via binary fission in one plane and containing differentiated cell types—i.e. heterocysts (H) and akinetes (A)—e.g. *Dolichospermum* sp. (formerly *Anabaena*); and (V) multiseriate and/or branching trichomes, reproducing via irregular binary fission patterns and containing differentiated cell types—e.g. *Nostochopsis* sp. Classification based on the systematic outline proposed by Boone et al., (2001).

1.1.2 Cyanobacteria Harmful Algal Blooms

In freshwater habitats cyanobacteria are known to form blooms that result from rapid growth in one or more species to the point where water quality is adversely affected. These Harmful Algal Blooms (HABs) can be a nuisance for recreational activities, but more importantly are associated with food web perturbations through the depletion of dissolved oxygen, shading of the water column leading to decreased species richness, and the production of toxic metabolites that cause illness and death in eukaryotic and prokaryotic organisms (Zimmer & Ferrer, 2007; Kaplan et al., 2012). The regularity and severity of cyanobacterial HABs (cyanoHABs) have increased in recent decades, in tandem with anthropogenic eutrophication and a warming climate (Jöhnk et al., 2008, Santer et al., 2019). Under eutrophic conditions, the species richness and diversity of phytoplankton assemblages undergo a transmogrification during the warm summer months, with cyanobacteria regularly becoming the dominant phytoplankton as a result of their favorable carbon uptake kinetics and the use of buoyancy-mediated vertical migration in stratified water column conditions (Walsby, 1994; Shapiro, 1997; Johnk et al., 2008). A recent socioeconomic report released by the EPA (EPA 820-F-15-096) regarding occurrences like the 2011/14 Lake Erie cyanoHABs highlighted the need for improved environmental management, and concluded that controlling anthropogenic nutrient pollution is more cost-effective than managing the effects of blooms once a bloom state has been established (Michalak et al., 2013). During the 2014 Lake Erie HAB, a persistent surface scum formed and the presence of microcystin was detected in the drinking water supply for Toledo, OH at concentrations above the EPA exposure thresholds for both external exposure and ingestion. This single HAB event impeded public access to drinking water for several weeks and caused a

widespread depression in local industry and tourism, resulting in a fiscal costs upwards of a billion dollars (EPA 820-F-15-096).

1.1.3 Thermal stratification of the water column and cyanobacterial dominance

Within lentic water bodies, prolonged periods of warm weather result in thermal stratification of the water column, leading to the formation and stabilization of distinct and immiscible water layers due to density differences between the layers (Figures 1.2 & 5.7), (Monismith et al., 1990). As aquatic photoautotrophs must balance their access to nutrient and energy pools, and thermal stratification enhances the spatiotemporal separation between nutrient and energy pools, buoyant cyanobacteria undergo diel vertical migration (DVM) cycles in order to fulfill their full nutritional complement (Figure 1.3), (Walsby, 1994; Molot et al., 2014). Regulated flotation as a mode of taxis greatly benefits cyanobacteria residing within thermally-stratified systems, as the rate of gas vesicle (GV) driven vertical migration increases in tandem with water temperature—ultimately far surpassing the rate of vertical migration observed in motile microbes—and increasing surface water temperatures drive increases in the depth and stability of thermocline boundary layers (Ibelings et al., 1994; Brookes & Ganf, 2001). Increasing aquatic temperatures caused by increasingly warm atmospheric conditions are predicted to increase stratification in freshwater environments, thus perpetuating the selective advantage of gas vacuolate cyanobacteria over non-buoyant phototrophs in the competition for nutrients at depth and light near surface boundary layers (Elliott et al., 2006; Johnk et al., 2008; Gao et al., 2016).

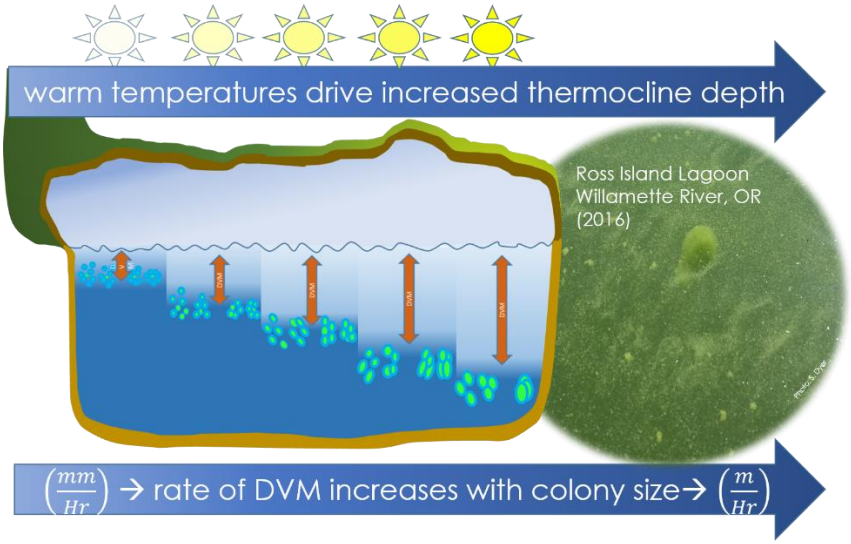

Figure 1.2: Persistent warm temperatures drive increases in the depth of seasonal thermocline boundary layers, generating a selective advantage in colonial, gas vacuolate cyanobacteria experiencing diel vertical migrations (DMVs) by increasing the rate of vertical migration.

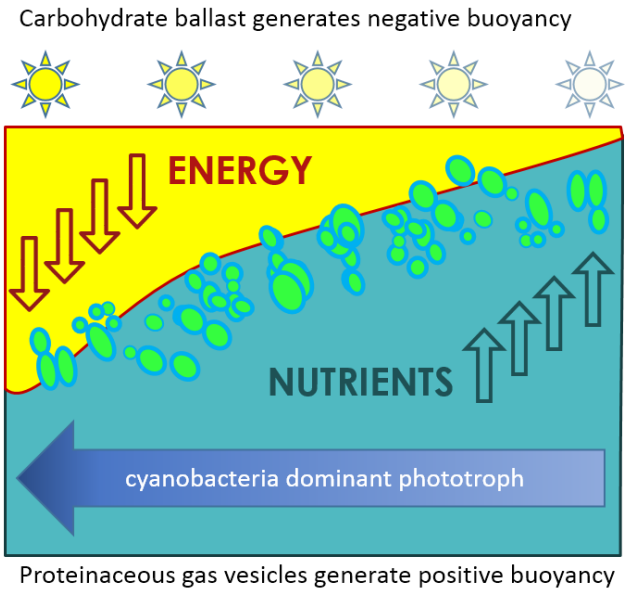

Figure 1.3: Buoyancy mediated DMVs and colonial aggregation in cyanobacteria populations increase access to nutrients at depth and light near air-water interfaces. The selective advantage of buoyant cyanobacteria over motile phytoplankton scales in tandem with the depth of the seasonal thermocline.

1.1.4 Enhanced stress associated with HAB formation

Surface scum formation may be a key aspect of the competitive advantage that cyanobacteria gain over other phytoplankton in lentic aquatic systems—while also contributing to their toxin production potential (Van de Waal et al., 2011; Meissner et al., 2015). In the 1993 Squaw Lake basin experiments, the annual formation of cyanobacterial climax communities was found to occur irrespective of initial inorganic carbon availability (Shapiro, 1997). However, within the dense bloom states generated by eutrophic conditions, past a certain population threshold metabolic adaptations unique to buoyant cyanobacteria provide an intense selective advantage, as CO_2 concentrations are depleted to the degree that only cyanobacteria are able to continue carbon acquisition and photosynthetic growth (Price et al., 2008; Daley et al., 2012). The rapid drawdown of dissolved carbon species also results in elevated pH, leading to enhanced GV synthesis and delayed degradation of the RNA transcripts associated with GV structural proteins, further amplifying the prevalence and dominance of buoyant cyanobacteria at air-water interfaces (Paerl & Ustach, 1984; Gao et al., 2016). Based on these considerations and supported by experimental observations, under specific conditions cyanobacteria benefit greatly from being as close to the air-water interface as possible, as the rate of diffusion of CO_2 in air is approximately five orders of magnitude more rapid than the rate of diffusion in water, and β-cyanobacteria in particular, are able to directly uptake CO_2 via a vectoral-diffusion mechanism mediated by the carbonic anhydrase-like $NDH_{I_{3/4}}$ transport systems (Figge et al 2001; Maeda et al., 2002; Zhang et al., 2004). Further commentary on the organization of the cyanobacterial carbon concentrating mechanisms (CCMs) and their role in the development and succession of HAB states is given in Chapter 7.

Despite the benefit of increased access to photosynthetic feedstocks, localized bloom formation near surface boundary layers creates deficits in the availability of nutrients needed for balanced growth and exposes cells to high levels of UV-radiation (UVR), which can lead to cellular level stress (Kaebernick et al., 2000; Downing et al., 2011; Zilliges et al., 2011). Surface trapping and the associated disruption of normal DVM cycles is due in part to the formation of aggregated morphologies (Ibelings et al., 1994). The development of aggregated morphologies, coupled with high rates of photosynthesis, often result in the nucleation of dissolved oxygen gas and the formation of oxygen bubbles within the anionic, extracellular polymeric substances (EPS) matrices of the cyanobacterial aggregates (Dervaux et al., 2015). Due to these considerations, the formation of surface scums is not easily reversed and leads to unfavorable conditions for the cells, especially during periods of elevated O_2 concentration in concert with high solar fluence rate—factors associated with enhanced photochemical damage to DNA and protein systems, and increased production of cyanotoxins (Garcia-Pichel, 1998; Van de Waal et al., 2011; Meissner et al., 2015).

1.2 *Gas Vesicles in Cyanobacteria*

1.2.1 Background

Gas vesicles are gas-filled, proteinaceous inclusion bodies devoid of lipids or carbohydrates that form regularly repeating amyloid fibril structures from the self-assembly of small amphiphilic GvpA monomers, resulting in a cylindrical bicone assembly consisting of a continuous cross β-sheet with strongly hydrophobic, and hydrophilic, interior and exterior faces, respectively (Blaurock & Walsby, 1976; Strunk et al., 2011; Ezzeldin et al., 2012). GvpA synthesis and the production of GVs has been demonstrated for a diverse range of aquatic and terrestrial prokaryotes, including many species of bloom forming cyanobacteria, as well as

extremophilic methanogens, arsenic-methylating halophiles, pathogenic human enterobacteria, and antibiotic producing actinomycetes (McMaster et al., 1996; Pfeifer, 2006; van Keulen, 2006). A high degree of GvpA sequence similarity between diverse organisms has been noted (65.8% between *Anabaena flos-aquae* and *Halobacterium sp. NRC-1*), and the physiological role of providing buoyancy in cyanobacteria has been identified (Walsby, 1994). The function of GVs in other microbes—especially for enterobacteria, and benthic and soil bacterium—remains to be elucidated, as does the tertiary structure of GvpA and the quaternary structure of intact GVs—due to the lack of a well refined atomic structure for both GvpA and the larger GV assembly (Walsby, 1994; Li & Cannon, 1998; Bently et al., 2002).

1.2.2 GvpA structural features in cyanobacteria

Determination of the regulatory mechanisms associated with buoyancy modulation in gas-vacuolate organisms is been hindered by the lack of a well refined atomic structure for both GvpA and the larger GV assembly. However, elucidation of key structural features and identification of potential regulatory mechanisms associated with GV function in cyanobacteria can be made based on a combination of results from prior studies, including: (i) fiber-based (solution) x-ray crystallography of GVs (Blaurock & Walsby, 1976); (ii) MALDI-TOF mass spectrometry analysis of GV and GvpA proteolysis products (Belenky et al., 2004; Dunton et al., 2006), (iii) 2D NMR characterizations of GvpA secondary structure and solvent accessibility (Sivertsen et al., 2009/10), (iv) FTIR spectroscopy-assisted structural modeling of GvpA secondary structure (Strunk et al., 2011), and (v) TEM analysis of the effects of point mutations in GvpA, and deletions from the C-terminus of GvpA, on GV structural integrity and GV shape (Strunk et al., 2011).

Examining GvpA sequence alignments for a number of freshwater cyanobacteria reference strains, and the associated secondary structure predictions, we see that the core 51-residue segment (S9-A60 of the consensus sequence, containing α-helix-I and both β-sheet regions), is highly conserved among species from all five cyanobacterial morphotypes (Figures 1.1 & 1.4). The C-terminus containing α-helix-II is variable among cyanobacterial orthologs (Figure 1.4), and a high degree of variability in both sequence identity and length exist in this segment of GvpA among the enterobacteria and halobacteria known to produce GVs (Walsby, 1994; Pfeifer, 2012). In addition to sequence similarity, the overall topology of GvpA monomers, as determined from the 2D NMR and fiber x-ray crystallography studies of Sivertsen et al., (2010) and Blaurock & Walsby (1976), respectively, is highly conserved between homologs.

Within the continuous β-sheet portion of GVs, all charged and aromatic residues are proposed to be oriented on one face of the GVs (Figures 1.4 & 1.5), where the formation of salt bridges and pi-stacking occur between adjacent GvpA monomers at conserved aspartate/glutamate/arginine and tryptophan residues, respectively (Sievertsen et al., 2010; Ezzeldin et al., 2012). The four residue translation of protein primary sequence occurring over two monomers within the β-sheet portion of GvpA gives rise to a 36° slant to the GV ribs (Sivertsen et al., 2009). This slant orients the ribs at a 54° angle to the long axis of the GVs, and results in optimal structural loading of the GVs (analogous to a filament wound vessel), where the longitudinal and circumferential stresses are perfectly balanced—maximizing both protein investment and structural integrity (Walsby, 1994). In addition to their remarkable structural characteristics, the alternating pattern of non-polar and polar residues within the β-sheet portion of GVs is also of note, as this pattern has been shown to be amyloidogenic, and as such, to be

evolutionarily unfavorable, while GVs are highly functional proteinaceous organelles (Broome & Hecht, 2000).

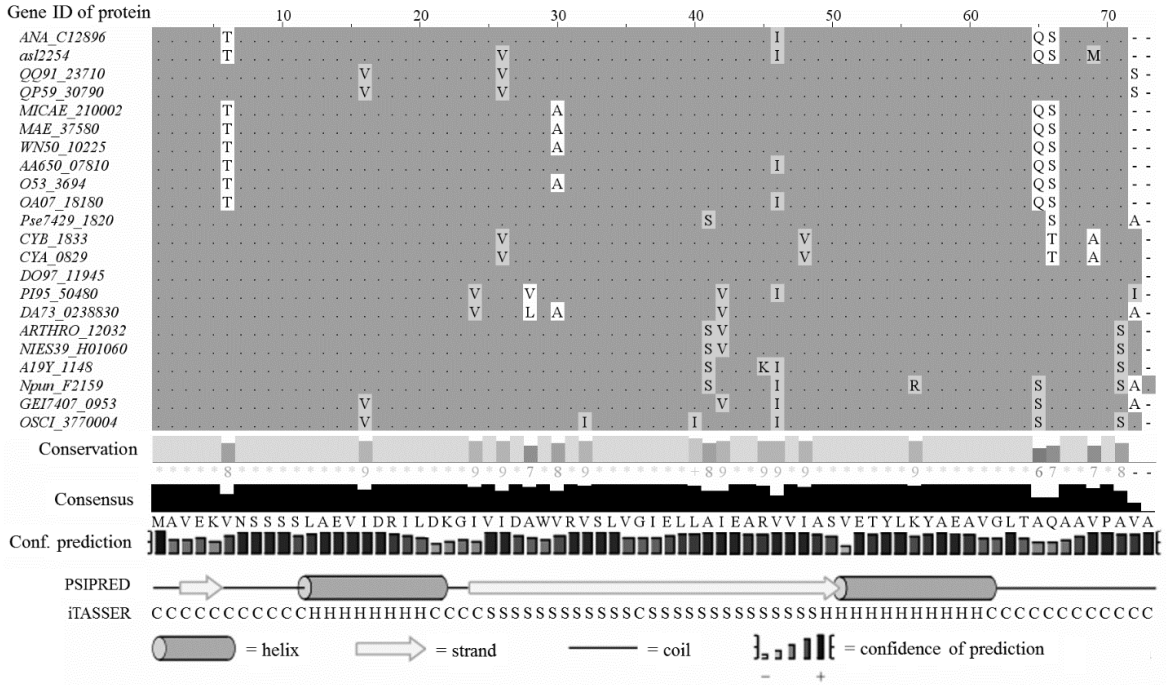

Figure 1.4: Sequence alignment (Clustal), and predicted secondary structure elements (PSIPRED & iTASSER), of the consensus sequence for gas vesicle protein A (GvpA) derived from freshwater cyanobacteria reference strains (KDRI database).

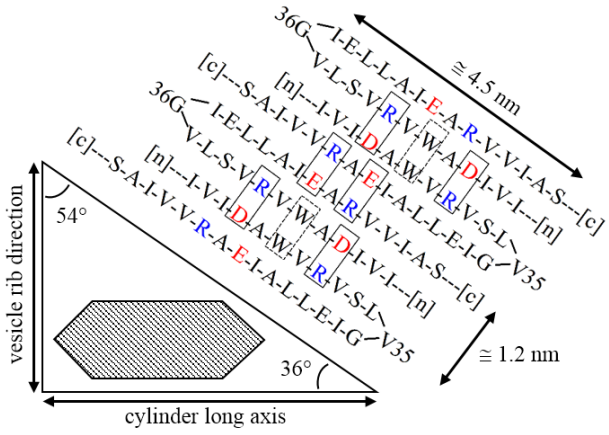

Figure 1.5: Predicted topology of gas vesicle ribs formed by the β-sheet portion of GvpA based on the consensus sequence (Figure 1.4).

1.2.3 Gas vesicles and the evolution of cyanobacteria

The high degree of GvpA homology between cyanobacterial species, including representatives from all five morphological subtypes (Figures 1.1 & 1.4), implies an early evolutionary origin for planktonic modes of life arising from the presence of GVs (Garcia-Pichel, 1998). The advent of multicellularity in cyanobacteria is proposed to have occurred shortly before the great oxidation event (GOE), (Schirrmeister et al., 2013). Prior to the GOE and the formation of a stratospheric ozone shield, exposure to UVR was greatly increased (Gargia-Pichel, 1998). However, with the advent of oxygenic photosynthesis and the associated transition away from a reducing atmosphere, the chemical equilibria for a majority of the redox-active dissolved metal species capable of absorbing UVR shifted toward the formation of insoluble precipitates, resulting their large-scale removal from aquatic environments (Scott et al., 2008). This stepwise removal of dissolved, reactive metal species further increased the risk of exposure to UVR in planktonic populations—specifically to the UV-B wavelengths (280-320 nm) associated with direct photochemical DNA and protein damage (Gargia-Pichel, 1998). For the planktonic populations that existed during this period, the complete avoidance of UVR would have required migration to deep-water refuges, with the 1% light limit for UV-B wavelengths predicted to have fallen at depths of greater than eleven meters (Gargia-Pichel, 1998). However, based on the fossil evidence of stromatolite formations estimated to be 3.4-billion-years-old, planktonic populations were likely present in shallow, evaporitic waters during this time, where UVR exposure would have been a constant threat (Altermann & Kazmierczak, 2003). Further, the homology of DNA repair mechanisms between extant Bacteria, Archaea, and Eukaryota, and the host of UV sun-screening compounds produced by cyanobacteria, indicates that DNA and protein damage due to UVR were sustained and ecologically relevant stressors in the early

evolution of planktonic cyanobacteria (Häder & Tevini, 1987). Based on the early evolution of GVs—prior to divergence from a last common cyanobacterial ancestor, the present-day homology of the core cyanobacterial metabolon, and the profound UVR-associated stressors present during the evolution of oxygenic photosynthesis in cyanobacteria, it is likely that buoyancy regulation mechanisms in cyanobacteria are conserved and strongly responsive to solar flux and UVR exposure (as discussed in Chapter 5).

1.2.4 Gas vesicles and pressure nephelometry

First described in Walsby's examination of gas vacuolate cyanobacteria (Walsby, 1971), the physical properties of GVs can be examined via pressure nephelometry, from which a number of metrics with important ecological consequences can be derived. In bacteria possessing a cell wall, the variable osmolarity of the cell's interior vs the osmotic pressure (π) exerted by the external milieu establishes a turgor pressure (Pt) based on the solute potential of the cell (Ψ_s) and the hydraulic conductivity of the cell surface (Lp) (Kiil, 1989; Rojas & Huang, 2018). This turgor pressure is balanced by stress in the cell wall, in a relationship described by Young's elastic modulus (ε)—a measure of three-dimensional stiffness possessing the same units as turgor (i.e. force per unit area) that is most regularly employed in cell physiology to describe volume-to-turgor relationships (Figure 1.6), while also furnishing information about the mechanical properties of cells (Guz et al., 2014). Cell turgor and the associated mechanics are intricately linked to: osmoregulation, cellular elongation and differentiation events, the regulation of endocytosis and signal transduction pathways, and several other cellular level processes (Epstein et al., 1990; Whatmore & Reed, 1990; Beauzamy et al., 2014; Wood, 2015). Thus, changes in turgor can be closely monitored and deviations from a baseline value can be used to track changes in cellular metabolism—with recent reports utilizing shifts in turgor from

baseline values as a marker for cellular abnormalities correlated with human disease (Castellani et al., 2001).

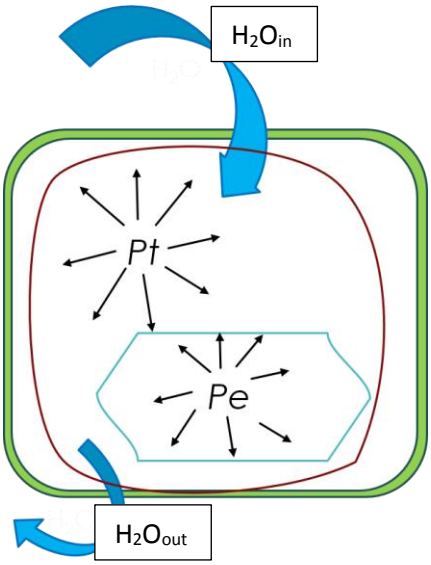

Figure 1.6: The transport of water into gas vacuolate cyanobacteria is driven by osmotic gradients; the resultant turgor pressure (Pt) against the plasma membrane (red) is balanced by stress in the cell wall (green). The effective critical collapse pressure (Pe) of gas vesicles (teal) is affected by Pt and varies among cyanobacteria species.

1.3 The Atypical Amino Acid β-N-methylamino-L-alaine (BMAA)

1.3.1 Background

Unique among the various cyanotoxins, BMAA (IUPAC: L-2-amino-3-(*N*-methylamino)propionic acid; 2-amino-3-(methylamino)propanoic acid; α-amino-β-(methylamino)propanoic acid) is a non-proteinogenic amino acid derivative (Figure 1.7), that has been isolated from representative species of all five cyanobacteria "Orders," suggesting an evolutionary origin predating the advent of multicellularity in cyanobacteria and the divergence from the last common cyanobacterial ancestor (Cox et al., 2005; Schirrmeister et al., 2015). The

evolutionary conservation of BMAA production across cyanobacterial morphotypes indicates that the compound may play a fundamental role within the canonical cyanobacterial metabolon. Further differentiating BMAA from known cyanotoxins is its apparent lack of acute toxicity (Cox et al., 2005; Chernoff et al., 2017; Manolidi et al., 2019). Protein associated and free cytoplasmic BMAA are regularly detected in environmental samples, with reports indicating that BMAA remains present for the duration of the bloom forming season, from concentrations below the limit of detection up to thousands of micrograms per gram of dry cell weight, with peak concentrations appearing in tandem with bloom senescence (Cox et al., 2005; Jonasson et al., 2010; Pip et al., 2016; Chapters 2 & 5 of this dissertation). The primary human health concern due to prolonged BMAA exposure is the compounds potential role as an etiological agent of multiple neurodegenerative diseases, including forms of amyotrophic lateral sclerosis (ALS) and related disorders (Spencer et al., 2005; Chernoff et al., 2017; Scott & Downing, 2018).

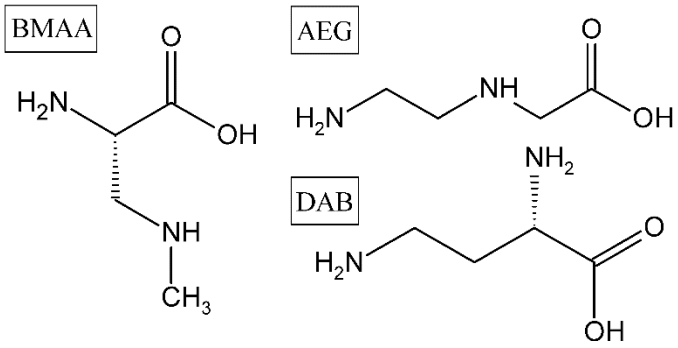

Figure 1.7: Structure of BMAA and the co-occurring cyanobacterial isomers, N-(2-Aminoethyl)glycine (AEG) and 2,4-Diaminobutanoic acid (DAB).

1.3.2 Metabolic responses to BMAA in cyanobacteria

Despite an increased interest in the biochemistry of BMAA, the majority of studies to date have focused on the effects the compound elicits in animal models and eukaryotic cell lines

(Liu et al., 2009; Chernoff et al., 2017; Scott & Downing 2018). Hence, there is a need for greater understanding of the ecophysiological drivers of BMAA production by cyanobacteria, especially within the broader context of regularly occurring HABs.

Previous research has identified a biochemical role for BMAA in nitrogen metabolism. Application of exogenous BMAA at micromolar concentrations to cyanobacterial cultures of *Nostoc* sp. PCC7120 and *Anabaena* sp. PCC7120 abolished heterocyst differentiation and resulted in the loss of nitrogenase activity (Berntzon et al., 2013; Popova et al., 2018). Further, the BMAA-associated prevention of biological N_2 fixation resulted in a nitrogen starvation response, typified by glycogen accumulation and the development of a chlorotic state due to the degradation of phycobilisome accessory pigments (Berntzon et al., 2013; Hickman et al., 2013). In addition to eliciting a nitrogen starvation-like response, using cultures of *Synechocystis* sp. J341 and *Microcystis* sp. PCC7806 grown on ^{15}N-labeled nitrogen sources, Downing et al., (2011) demonstrated that nitrogen starvation results in the de novo production of BMAA. In the *Synechocystis* sp. analyzed, the first statistically significant increase in BMAA concentration occurred approximately 48 h after nitrogen deprivation and continued to increase over a 120 h period; ^{15}N-BMAA was appropriately detected as a propyl chloroformate derivative via HPLC-MS/MS (Downing et al., 2011; Chernoff et al., 2017). Further, based on $^{15}NH_4^+$ spike experiments of nitrogen starved cultures that had been grown on $^{14}NH_4^+$, and the timeline for the appearance of ^{15}N within proteinogenic amino acids as compared to the delayed appearance of ^{15}N-BMAA, it was proposed that BMAA synthesis does not occur via the primary transamination reactions associated with nitrogen assimilation (Figure 1.8), and the synthesis of the proteinogenic amino acids (Downing et al., 2011). Thus, BMAA production appears to be

linked to cellular nutrient stress, and is likely produced as a breakdown product, or as was recently indicated by Faassen et al., (2016), is released from a bound reservoir.

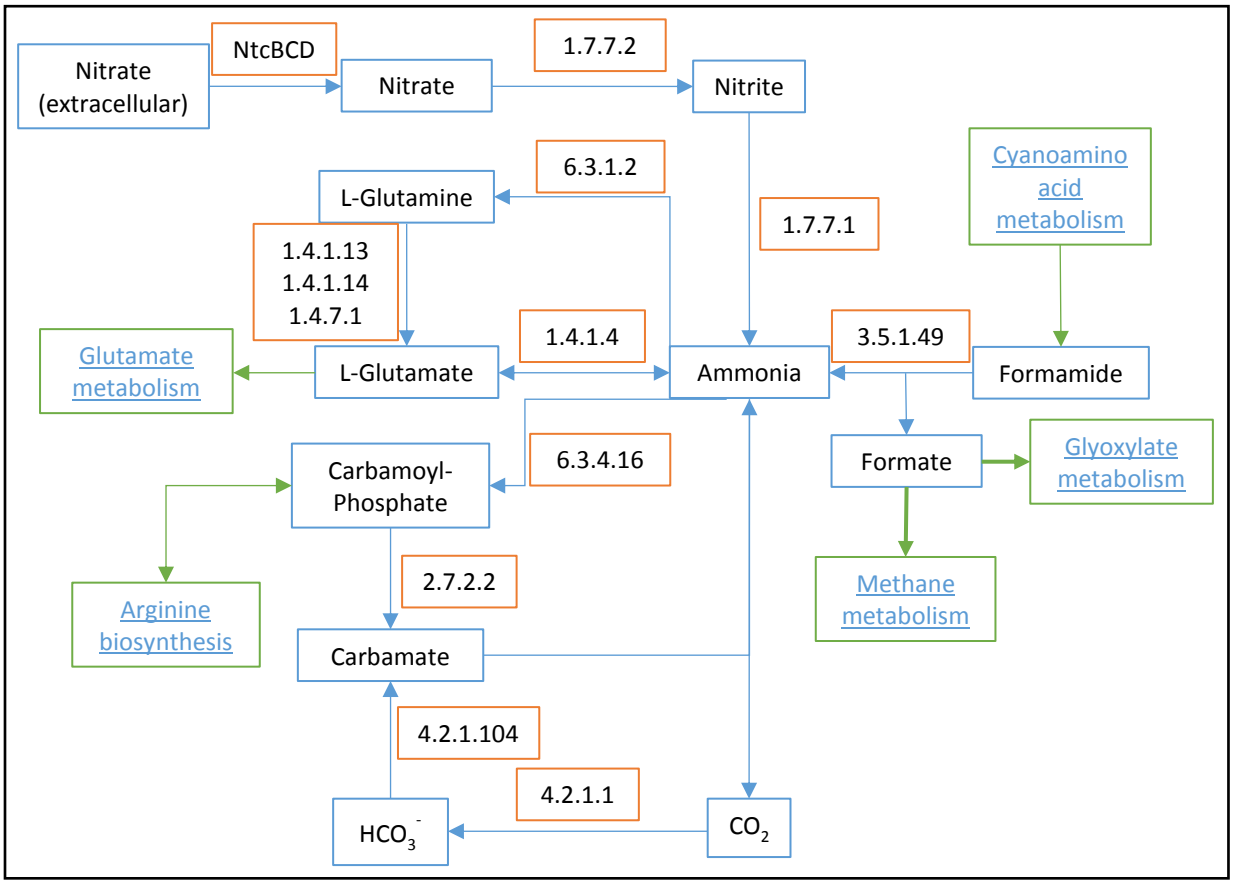

Figure 1.8: Nitrogen assimilation and metabolic pathways associated with amino acid biosynthesis in *Microcyatis aeruginosa*; (orange boxes) enzyme commission (EC) number of reaction step; (green boxes) closely associated metabolic pathways (Kanesiha & Goto, 2000; KEGG)—URLs for metabolic pathways from KEGG database given in references).

The nitrogen assimilation pathway in cyanobacteria is dependent on a limited number of proteins and metabolites, central to which are the glutamine synthetase/glutamine oxoglutarate aminotransferase (GS/GOGAT) pathways (Figure 1.8; EC numbers 6.3.1.2 and 1.4.1.13, respectively) and the α-ketoacid, 2-oxoglutarate (Flores & Herrero, 2005). Moreover, 2-

oxoglutarate (2OG) is the primary response regulator of the global nitrogen control transcription factor, NtcA, which has been shown to be autoregulatory (Vazquez-Bermudez et al., 2002; Ginn et al., 2010). When cells become nitrogen limited, the synthesis of glutamate from glutamine slows, resulting in the accumulation of 2OG and reductant in the form of NAD(P)H (Klotz et al., 2015). Nitrogen starvation also drives protein degradation, involving the deamination of amino acids and deamidation of asparagine and glutamine in early steps, both of which increase intracellular free acids, particularly 2OG (Schwarz & Grossman, 1998). This increase in 2OG would generally activate the NtcA regulon, resulting in the induction of genes coding for ammonia permeases and ABC nitrate/nitrite transporters—in the absence of nitrogen this is an impossible response (Muro-Pastor et al., 2001). Instead, in order to overcome the redox imbalance and meet cellular Carbon:Nitrogen (C:N) requirements, nitrogen starved cyanobacteria will shift their metabolism and begin accumulating glycogen and other carbon stores in order to consume the excess reductant (Hickman et al., 2013). This type of metabolic regulation is also observed in excessively illuminated cells (where solar photon flux overwhelms the donor side of photosystem-II), resulting in the induction of cyanobacterial carbon-concentrating mechanisms (CCMs) in order to consume excess reductant and increase cellular density (Daley et al., 2012; Shibata et al., 2001; Woodger et al., 2005). A more detailed description of the metabolic systems associated with inorganic carbon and nitrogen biochemistry in cyanobacteria, and how BMAA may be involved in their regulation, is provided in Chapter 7.

The finding that BMAA treatment—even in nutrient replete cells—produces a cellular response akin to nitrogen limitation, and results in metabolic alterations geared towards the generation of energy reserves, resulting in increased cellular density, hints at a role in buoyancy modulation in response to cellular redox imbalances. Nitrogen starvation in diazotrophic

cyanobacteria would typically result in the induction of N_2 fixation, however the finding that BMAA inhibits nitrogenase activity and heterocyst differentiation further suggests metabolic alterations geared toward sinking or cellular migration away from surface boundary layers (Ernst & Böger, 1985; Berntzon et al., 2013). In summary, it is here proposed that stress responses to environmental stimuli associated with UVR exposure and the positioning of buoyant cyanobacterial populations near surface boundary layers, and attempts to balance energy supply and consumption with nutrient access, are the primary ecophysiological drivers of BMAA production, and that upon production, BMAA alters the buoyant state of gas vacuolate populations. This postulate is discussed extensively in Chapter 5.

1.3.2 Human health impacts of BMAA

Following World War II, during the US occupation of Guam, a 100-fold enrichment in the incidence of neurolathyrism and Amyotrophic lateral sclerosis/Parkinsonism-dementia complex (ALS/PDC)—as compared to the rest of the world—was noted within multiple, geographically isolated, indigenous populations—later termed, "Guam-PD" (Gajdusek, 1963; Spencer et al., 2005). Screening of the Chamorro population revealed that the enrichment in ALS/PDC appeared to lack a genetic basis, indicating that environmental exposure to some unknown agent was to blame. The efforts of multiple medical anthropologists ultimately led to the isolation and identification of BMAA within cycad seeds—a dietary staple for both the Chamorro and the flying foxes they considered a culinary delicacy (Spencer, 1987). Further evidence of the bioaccumulation and biomagnification of BMAA led to the hypothesis that Guam-PD was a result of prolonged exposure to BMAA, and that cyanobacterial BMAA production (as a symbiont with cycads) resulted in food web incorporation and led to the

elevated incidence of ALS/PDC observed in other geographically isolated populations within the region (Banack & Cox, 2003; Cox et al., 2003; Monson et al., 2003; Murch et al., 2004).

Physical evidence for the development of ALS/PDC in response to prolonged dietary BMAA exposure was recently demonstrated, where Vervet monkeys fed a diet of BMAA-dosed fruit formed neurofibrillary tangles (NFTs) and β-amyloid plaques—diagnostic hallmarks of AD (Cox et al., 2016). A recent study in a rat model indicated that a single neonatal exposure to BMAA, administered via subcutaneous injection during a critical neurogenesis period, was sufficient to produce the combined suite of histopathological abnormalities observed in patients suffering from Guam-PD (Scott & Downing, 2018). Evidence has also implicated BMAA as an excitotoxin and agonist of metabotropic glutamate receptor 5 (mGluR5), resulting in enhanced cellular stress and dysregulation of ion channel activity in mixed cortical cell cultures containing neuronal cells (Liu et al., 2009). In addition to the proposed excitotoxic effects, BMAA ingestion has been shown to inactivate/desensitize NMDA and AMPA receptors, resulting in attenuated postsynaptic responses to excitatory ions, Ca^{2+} in particular (Koenig et al., 2016). Modulation in the activity and function of mGluR5 via glutamate binding is also involved in the regulation of protein kinase activity and Ca^{2+} release form intercellular stores, and hyperphosphoralation and changes in Ca^{2+} regulation have been shown to occur in response to BMAA exposure (Xiao et al., 2006).

Despite increasing evidence for the hypothesis that BMAA is a causative agent in the development of a form of human neurodegenerative disease, it is not without its critics. As recently stated by Cernoff et al., in their 2017 critical review of the topic, "before public health actions are taken based on the [BMAA-ALS/PDC] hypothesis, it is imperative that fundamental

issues and inconsistencies concerning the central assumptions are discussed and resolved." These fundamental issues include:

- Issues with the measurement and quantification of BMAA
- Evidence for BMAA formation by most species of cyanobacteria
- Evidence for BMAA misincorporation into proteins

1.4 – Dissertation overview

This thesis addresses gaps in our understanding of the environmental drivers of production and the ecophysiological role of BMAA within freshwater cyanobacteria as it relates to buoyancy regulation and cellular stress responses. The first objective, covered in Chapter 2, addresses the identified issues associated with the detection and quantification of BMAA within complex biological matrices via development of a dansyl derivatization and HPLC-MS/MS detection method. This method improves the detection limits for BMAA, and reduces uncertainties associated with HPLC-MS/MS detection arising from internal standard variability. Chapter 3 describes the development and implementation of an improved pressure nephelometry system for the in vivo characterization of gas vesicle physical properties, the measurement of cellular growth rate, and the quantification of cell turgor in gas vacuolate organisms. Chapter 4 describes instrument refinements and data analysis tools for the pressure nephelometry method that allow for the in situ identification and quantification of gas-vacuolate cyanobacteria species in natural samples as a means to track population dynamics within HABs. Finally, Chapter 5 investigates the relationship between BMAA prevalence and cyanoHAB population dynamics, and presents laboratory and environmental time series evidence for a causal link between BMAA and buoyancy regulation in gas vacuolate cyanobacteria.

2. Improved quantification of the cyanobacterial metabolite, β-N-methylamino-L-alanine (BMAA) using HPLC-MS/MS detection of its dansyl chloride derivative referenced to a ^{15}N-labeled internal standard[1]

2.1 Abstract

Environmental exposure to the cyanotoxin, β-*N*-methylamino-L-alanine (BMAA), has been implicated as the etiological agent of a human neurodegenerative disease possessing the combined neuropathologies of amyotrophic lateral sclerosis/Parkinsonism-dementia complex (ALS/PDC). However, the hypothesis linking dietary exposure to BMAA in isolated populations to their elevated incidence of ALS/PDC has been criticized due to methodological issues that include a failure to separate BMAA from co-eluting and/or isobaric compounds during quantification. We developed an improved HPLC-MS/MS quantification method for the total fraction of the dansyl chloride (DNS) derivatives of BMAA, 2,4-Diaminobutyric acid (DAB), and *N*-(2-Aminoethyl)glycine (AEG). The use of ^{15}N-labelled BMAA as a stable isotope-labeled (SIL) internal standard (^{15}N-BMAA) provides a direct comparison for quantification of total BMAA, and generates a more robust (>20:1 peak area) and stable (25.8% vs 68.2% mean deviation of peak area) MS quantification transition as compared to the deuterated analogue, $^{2}H_3$-BMAA, used in prior studies. Partial method validation using ^{15}N-BMAA as a SIL internal standard provided high accuracy and precision (R^2>0.999; S=0.004) over a wide range of L-BMAA concentrations (0–100 μg g^{-1} lyophilized material), with improved lower limits of quantification (LLOQ) and detection (LOD) of 23 and 2.4 ng g^{-1} lyophilized material, respectively. BMAA was detected at several sites in the Lower Columbia River (USA) above the

[1] Dyer, S.W., J.A. Needoba, & T.D. Peterson. *Analytical Methods*: submitted 02/08/19 (in review)

LOD, and at concentrations ranging from 23.5±4.5 to 63.3±18.1 ng g^{-1} lyophilized-material. Use of dansyl chloride derivatization provides a less expensive alternative to 6-aminoquinolyl-*N*-hydroxysccinimidyl carbamate (AQC)-based methods. We note that the use of deuterated SIL standard variants and the derivatization buffer pH used in prior studies may have led to over estimates of total BMAA concentration and therefore contributed to the historic disagreement regarding the prevalence and abundance of BMAA.

2.2 Introduction

Cyanobacteria are ubiquitously distributed across Earth's aquatic, terrestrial, and subterranean environs, and account for ~25% of global primary production (Puente-Sánchez et al., 2018). However, many aspects of cyanobacterial metabolism remain obscure. This is especially true for cyanobacterial toxins (cyanotoxins), which include a diverse array of non-essential amino acids and secondary metabolites. Cyanotoxins often contain atypical chemical moieties that elicit toxic effects in both eukaryotic and prokaryotic organisms. One cyanotoxin that has garnered great interest in recent years is the non-essential amino acid, BMAA (Zimmer & Ferrer, 2007; Kaplan et al., 2012; Neilan et al., 2013).

An increasing body of evidence suggests that the enriched prevalence of Alzheimer's Disease (AD), and Amyotrophic Lateral Sclerosis/Parkinsonism Dementia Complex (ALS/PDC) endemic to discrete geographic locations in the Western Pacific is a direct result of prolonged environmental and dietary exposure to BMAA (Cox et al., 2003; Murch et al., 2004; Spencer & Palmer, 2005). The histopathological presentation of the disease state related to BMAA is distinct from typical neurodegenerosis, possessing a combination of traits distinct to AD, ALS and/or PDC that do not regularly occur in tandem (Scott & Downing, 2017). Bolstering the epidemiological findings, laboratory studies in *Drosophila* sp., mouse, rat, and non-human

primate models with dietary exposure to, and/or subcutaneous injection of, BMAA produced alterations in transmembrane regulatory networks and ion channels, and the development of neuropathologies consistent with AD/ALS/PDC (Xiao et al., 2006; Liu et al., 2009; Koenig et al., 2015; Cox et al., 2016; Metcalf et al., 2017; Scott & Downing, 2017). Further, bioaccumulation and magnification through food webs has been demonstrated, with concentrations of BMAA, AEG, and DAB comparable to those used in prior toxicology studies being detected in the edible portions of commercial seafood, as well as a number of health food supplements derived from cyanobacteria (Brand et al., 2010; Jonasson et al., 2010; Jiao et al., 2014; Glover et al., 2015; Manolidi et al., 2019).

Given the seriousness of the potential threat to public health, the BMAA hypothesis has received a high degree of scrutiny (Chernoff et al., 2017). In particular, a number of issues related to the quantification of BMAA have been raised. Initial detection of BMAA in environmental and tissue samples based on liquid chromatography (LC) and spectroscopic detection suffered from poor specificity, due to the co-elution of fluorescently tag, primary and secondary amine-bearing compounds present in the BMAA fraction (Lage et al., 2016; Foss et al., 2018). More recently, quantification of underivatized BMAA using LC coupled to mass spectrometry (MS) suffered from enhanced background interference due to co-elution of isobaric compounds (i.e. DAB and AEG) as well as other low molecular weight, polar organics present in environmental samples; as a result, there was poor quantitative agreement among studies (Rosén & Hellenäs, 2008; Duncan, 2012; Faassen et al., 2012; Foss et al., 2018).

Derivatization of BMAA using dansyl chloride (DNS) constitutes a cost-effective method for BMAA detection via HPLC-MS/MS, with the reduced polarity from the DNS tag enhancing the elution profile and separation of small polar compounds via reversed phase liquid

chromatography. In addition, dansylation generates a larger and more reactive surface for fragmentation—enhancing the signal-to-noise ratio—and results in characteristic mass spectrometry fragmentation patterns, a crucial prerequisite for the disambiguation of BMAA from isobaric compounds and constitutional isomers (Weber, 1952; Jiang et al., 2014; Roy-Lachapelle et al., 2015).

In order to assess exposure risks from environmental and dietary sources, accurate quantification of total BMAA (i.e. protein associated, bound, and soluble bound fractions) within the producing organisms is essential (Faassen et al., 2016; Rosén et al., 2016). This work was conducted to provide partial method validation for the HPLC-MS/MS analysis of DNS-BMAA adducts utilizing ^{15}N-BMAA as a SIL standard for the quantification of total BMAA. In addition to providing a comparison between ^{15}N-BMAA and the previously utilized SIL standard, $^{2}H_3$-BMAA, we demonstrate pH-dependent reactivity of nucleophilic targets during derivatization; previous dansyl derivatization of BMAA was carried out at less alkaline pH, which could have influenced measurement sensitivity.

Utilizing ^{15}N-BMAA as a SIL standard, BMAA, AEG, DAB, and ANA-a were screened for in environmental samples collected during 2016 and 2017 from off-channel sites along the Lower Columbia River, USA, that have recently experienced cyanobacterial blooms.

2.3 Materials and methods

2.3.1 Standards, reagents, and stock solutions

L-BMAA hydrochloride (BMAA; CAS #:16012-55-8), purity ≥97% (NMR), L-2,4-Diaminobutyric acid hydrochloride (DAB; CAS #:1482-98-0), purity ≥98% (TLC), dansyl chloride (DNS; CAS #: 605-65-2), purity ≥99% (HPLC), sodium tetraborate (Borax; CAS

#:1330-43-4), purity ≥99%, and trichloroacetic acid (TCA; CAS 3:76-03-9), ACS reagent ≥99%, were purchased from Millipore Sigma (St. Louis, MO, USA). The stable isotope-labelled internal standards (^{15}N-BMAA and $^{2}H_3$-BMAA), purity ≥98% (NMR), were synthesized at the Oregon Health & Science University Medicinal Chemistry Core (Portland, OR, USA). *N*-(2-Aminoethyl)glycine (AEG; CAS #:24123-14-6) purity ≥97% (non-aqueous titration) was purchased from TCI America (Portland, OR, USA). (±)-Anatoxin A fumarate (ANA-a; CAS #:64285-06-9; ab120013), purity ≥98% (RP-HPLC/NMR), was purchased from Abcam Life Sciences (Cambridge, MA, USA). A certified analytical standard solution of saxitoxin dihydrochloride (STX; CAS #:35554-08-6), was purchased from Abraxis, Inc. (Warminster, PA, USA). Analytical/HPLC grade solutions of hydrochloric acid (HCl; CAS #: 7647-01-0), water (H2O; CAS #:7732-18-5), and acetonitrile (ACN; CAS #:75-05-8) were purchased from Fisher Scientific (Waltham, MA, USA). Sodium hydroxide (NaOH; CAS #:1310-73-2), purity ≥98%, was purchased from Acros Organics (NJ, USA).

HPLC-grade solvents and solutions were utilized during sample workup for each of the triplicate standard curves generated on separate days, and for the analysis of environmental samples. Starting from solid compounds, aqueous stock solutions of ^{15}N-BMAA, $^{2}H_3$-BMAA, BMAA, AEG, DAB, and ANA-a were prepared at a concentration of 5 ng μL^{-1} the day prior to sample workup, parafilmed, and stored at -20°C per manufacturer recommendations. For standard curve samples, serial dilutions of the BMAA stock solution were performed to generate working stocks with concentrations ranging from 0.01 to 1.0 ng μL^{-1}.

For all cyanotoxin stock solutions, and for all sample handling after the spike of cyanotoxin standards, siliconized centrifuge tubes were used, as BMAA and its isomers form very stable coordination complexes with cationic species, and are known to adhere to metal

impurities present in glassware (Cohen, 2012; Glover et al., 2012). All working stock solutions were allowed to equilibrate to room temperature prior to use, and all compound spikes were performed analytically by mass.

In order to control for matrix effects, a commercially available health food supplement consisting of lyophilized *Spirulina* sp. (Sunfood Superfoods: El Cajon, CA, USA) was used for all standard curve and positive control samples.

2.3.2 Environmental samples

Environmental samples were collected during the summer months of 2016 and 2017 in off-channel habitats of the Lower Columbia River (USA). Whole water surface samples and biofilm scrapings were collected in sterile 50 mL centrifuge tubes, which were then frozen and stored at -20°C until sample analysis. The material was lyophilized (Freezone4; Labconco Co., Kansas City, MO, USA), transferred to siliconized centrifuge tubes, and stored at -20°C until sample workup.

2.3.2 Sample preparation

Lyophilized samples (matrix and environmental cellular material) were homogenized and 1–3 mg of sample was transferred into tared siliconized centrifuge tubes, to which 20 mM HCl at a volume of 100 μL mg^{-1} sample was added. The centrifuge tubes were parafilmed and subjected to three-to-five freeze-thaw cycles in liquid N_2 to promote cell lysis. Following lysis, the samples were allowed to equilibrate to room temperature, at which point analyte standards were spiked analytically by mass to final concentrations ranging from 0.01–100 ng mg^{-1} lyophilized material (for standard curve samples), and SIL standards were spiked at 50 ng mg^{-1} lyophilized material for all samples. Following compound spikes, the centrifuge tubes were parafilmed and vortexed

(3x for ~10 sec per cycle) and allowed to equilibrate for >30 min. Following equilibration, samples were transferred by pipette to screw-cap high-recovery glass vials with PTFE septa. The centrifuge tubes were rinsed with an additional 100 μL of 20 mM HCl, vortexed, and the rinse was combined with the sample prior to the addition of 6M HCl at a volume of 200 μL mg^{-1} lyophilized material. The glass vials were then placed into a heated sand bath (110°C) and left for 20-24 h to enact proteolysis. After proteolysis, the vials were removed and allowed to cool to room temperature before transferring the hydrolysate to new siliconized centrifuge tubes. The hydrolysis vials were rinsed with 100 μL of 20 mM HCl, vortexed, and the rinse was combined with the hydrolysate, which was then condensed via rotary evaporation under strong vacuum at room temperature (Eppendorf Vacufuge™ with an inline glass solvent trap (-50°C) connected to an Edwards RV8 vacuum pump). The evaporation product is quite resinous and strongly adheres even to the siliconized centrifuge tubes; therefore, an additional clean-up and condensation step was performed. Samples were resuspended in 200 μL of 20 mM HCl and transferred to Ultrafree-MC 0.22 μm centrifugal filters (Millipore, Burlington, MA, USA), centrifuge tubes were rinsed with 100 μL of 20 mM HCl, vortexed, and the rinse was combined with the samples which were then centrifugally filtered (12,000 x g, 4 min). Following filtration the samples were flash frozen and condensed via lyophilization. The lyophilized filtrate was then stored at -20°C until derivatization.

2.3.3 Dansyl derivatization

Dansylation of target compounds was performed with modifications to the reaction conditions reported in previous methods (Salomonsson et al., 2013; Roy-Lachapelle et al., 2015). The lyophilized filtrate was resuspended in 10 μL H_2O mg^{-1} lyophilized-material, to which 50

μL buffer (0.2M Borax/NaOH, pH=10.2) mg^{-1} lyophilized-material was added. The samples were vortexed (~10 sec), 50 μL DNS reagent (7 mg mL^{-1} ACN) mg^{-1} lyophilized material was added, and samples were vortexed for an additional ~10 sec prior to placing the centrifuge tubes into a heated aluminum block (60°C) for 15 min. Subsequent to derivatization, an additional filtration step was performed (Ultrafree-MC 0.22 μm; 12,000 x g, 4 min) to remove excess salts and unreacted DNS. The filtrate was transferred to HPLC vials with polycarbonate caps and PTFE septa prior to HPLC-MS/MS analysis.

2.3.4 HPLC-MS/MS analysis

For MS/MS analysis, an Applied BioSystems 4000 QTRAP triple-quadrupole, linear ion trap hybrid MS was utilized (SCIEX, Framingham, MA, USA). The UPLC separation of compounds prior to MS analysis was carried out via an in-line Prominence system (Shimadzu Corp. Somerset, NJ, USA), utilizing a Gemini NX-C18 110Å (100 x 2.00 mm; 3 μm) column (Phenomenex, Torrance, CA, USA). Reverse phase separation and MS/MS detection of DNS labelled compounds were performed as in previous reports, utilizing the transitions given in Table 2.1, while compound elution times varied from previous reports and resulted in better isomer separation with minimal overlap (Salomonsson et al., 2013; Roy-Lachapelle et al., 2015).

2.4 Results and discussion

2.4.1 Dansyl derivatization

First proposed by Weber (1952), the formation of stable, fluorescent conjugates using DNS as a derivatizing reagent has widely been used in protein and amino acid analysis (Figure 2.1). In addition to providing a stable fluorescent tag, DNS derivatization improves the elution profile and separation of analytes via reverse phase liquid chromatography, and allows for the

disambiguation of isobaric, constitutional isomers via characteristic mass spectrometry fragmentation patterns (Figure 2.2/Table 2.1).

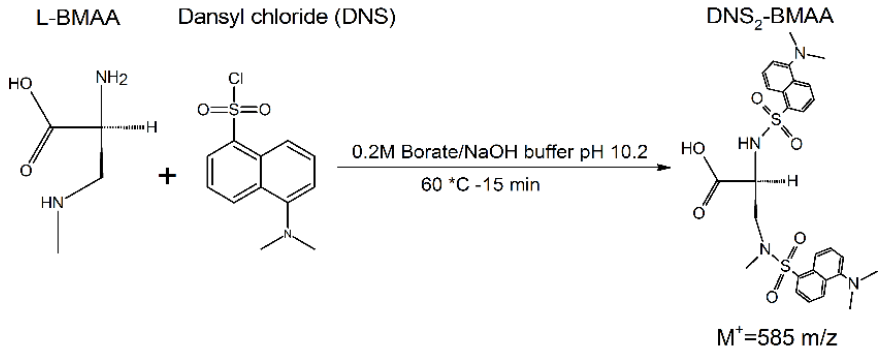

Figure 2.1: Reaction scheme for dansylation of BMAA. Quantification of BMAA via MS/MS based on 585>277 m/z transition with compound verification based on 585>71.

Table 2.1: HPLC-MS/MS detection parameters for dansylated target compounds

Analyte	Parent ion (*m/z*)	Quantification ion (*m/z*)	Confirmation ion (*m/z*)	RT (min)
BMAA	585.0	277.0	71.0	3.75±0.01
^{15}N-BMAA	586.0	278.0	72.0	3.74±0.01
$^{2}H_3$-BMAA	588.0	280.0	74.0	3.74±0.03
DAB	585.0	251.3	88.0	3.60±0.03
AEG	585.0	306.3	131.0	3.90±0.02
ANA-a	399.2	149.1	131.1	4.14±0.04

2.4.2 pH effects of the dansylation of polyamines

The rate of DNS hydrolysis is constant and negligible up to a pH of 9.5, above which the rate of hydrolysis increases exponentially (Gros & Labouesse, 1969). For complete dansylation of polyamines to occur, all amines within the polyamine must first be in a deprotonated, nucleophilic state (Peng et al., 1977; Heimbecher et al., 1997; Heimbecher et al., 1998). In their

study on the dansylation of the pentaamine pentaazapentacosane · 5 HCl (PAPC), (pKa: 8.6; 9.4; 10.3; 11.0; 11.8), Heimbecher et al., (1997), failed to detect partially dansylated products at any pH examined and no perdansylated PAPC (DNS_5-PAPC) was detected when the derivatization buffer pH was <9.5. The reaction yield of DNS_5-PAPC markedly increased over a pH range of 9.5 to 11.0. As the rate of DNS-amino acid formation is dependent on the starting amino acid concentration, the pH of the derivatizing solvent must approximate the pKa of the least DNS-reactive moiety while remaining low enough to avoid total loss of DNS by hydrolysis, particularly when analytes are present at low concentrations (Gros & Labouesse, 1969).

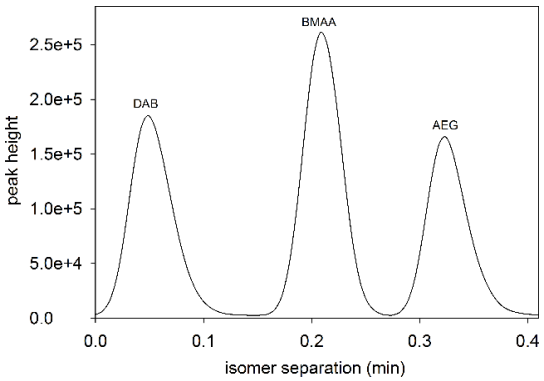

Figure 2.2: Elution profile of dansyl fragment from parent isomer in positive control sample (585>170 m/z), analytical standards of target compounds spiked into reference matrix at 50 ng mg^{-1} lyophilized material.

In our studies, reaction conditions of 0.2 M boric acid/NaOH buffer, pH of 10.2 at 60°C for 15 min were found to be optimal for DNS derivatization of BMAA, AEG, and DAB; in contrast, dansylation was highly variable when the derivatization buffer had a pH ≤ 9.5 or under shorter reaction times (Fig. 2.3). In addition, the pH of boric acid/sodium hydroxide buffers markedly decreases (ΔpH up to 2) during equilibration with atmospheric CO_2, making it essential that the buffer is prepared immediately prior to use (Fawcett & Acree, 1929).

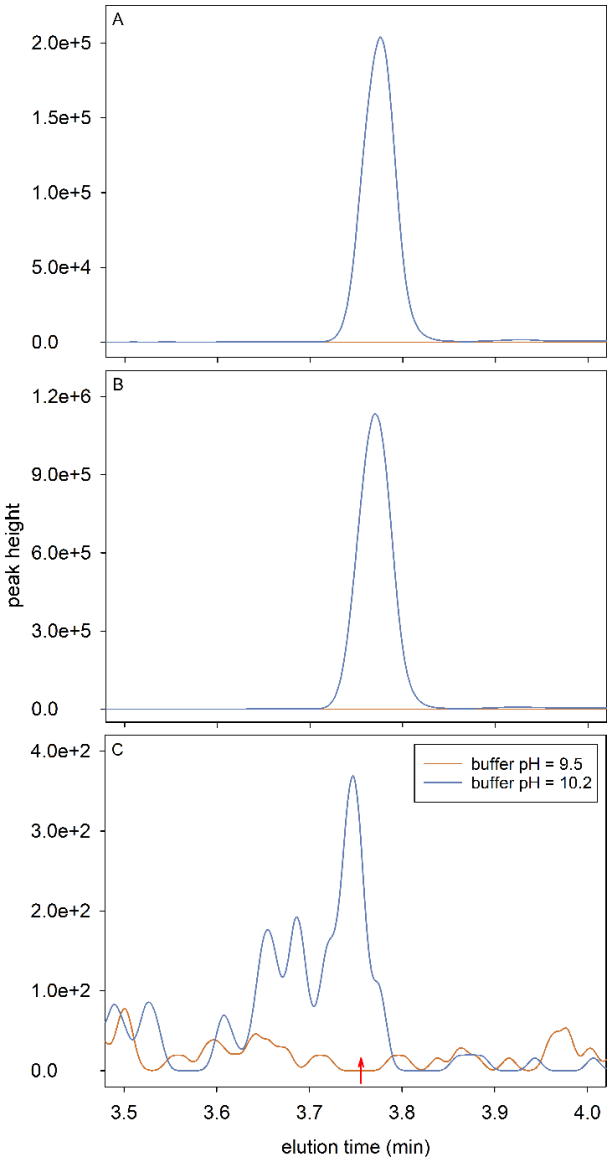

Figure 2.3: HPLC-MS/MS detection and elution profile of quantification peak (arrow) as a function pH for: (A) $^{2}H_3$-BMAA standard at 100 ng mg^{-1} lyophillized material, (B) analytical BMAA standard at 100 ng mg^{-1} lyophillized material, (C) endogenous BMAA detected in an environmental sample.

It is important to note that the pK_a values of accessible reactive amine groups are higher in free compounds than they would be in proteins or peptides, for which DNS and AQC

derivatization methods were initially developed. Following protein hydrolysis, the DNS-reactive amine groups in free compounds possess pK_a values in the range of 8.8–11.0 (Nelson & Cox, 2013). Considerations of buffer pH for BMAA dansylation are highlighted by nucleophilic reactions of the pyridoxal 5'-phosphate (PLP)-dependent enzyme, L-Methionine γ-lyase (EC 4.4.1.11), where reactivity ($\log(V_{max}/K_m)$) as a function of the pK_a of the conjugate acid produced by the β-replacement reaction of BMAA, demonstrates that that the reactivity of BMAA as a nucleophile ($pK_{aapparent}$=9.76) is much lower than would be expected, falling between that of methylamine (pKa≅35.0) and methylammonium (pK_a≅10.7) (Takada et al., 2014). Thus, the derivatization pH should be more alkaline than has been reported for DNS-based BMAA quantification; this may also be the case for AQC-derivatization and analysis.

As in previous studies utilizing DNS derivatization for cyanotoxin analysis, we attempted to detect DNS-labelled saxitoxin (DNS-STX), (Roy-Lachapelle et al., 2015). However, even in the absence of a matrix and when directly analyzing an analytical STX standard utilizing buffers at both pH 9.5 and 10.2, no transitions corresponding to DNS-STX were observed (data not shown), as was the case in the prior study. This further highlights the pH requirement for DNS derivatization of the cyanotoxins analyzed, as the less nucleophilic STX amine (pK_{a2}=11.28) presumably precluded derivatization under the reaction conditions employed, and may indicate that the derivatization buffer pH utilized in prior studies contributed to the historic disagreement regarding environmental concentrations of BMAA, DAB, and AEG, as all three possess an amine group with pK_a>10 (Rogers & Rapoport, 1980; Zimmerman et al., 2016).

2.4.3 Temperature effects on the dansylation reaction

Reaction conditions of 60 °C for 15 min were found to be necessary for dansylation of all target compounds, with lower reaction temperatures and/or shorter derivatization times failing to

generate the desired products (data not shown). Dansylation of amines is known to proceed at room temperature (Weber, 1952). However, increased reaction temperature was found to improve the yield of DNS-BMAA—likely due to metal complexation by BMAA with multiple species present in the complex environmental samples analyzed. Multiple studies have shown that BMAA readily chelates biologically-important divalent cations to form stable coordination complexes, with estimates that ratios of 23:1 and 135:1 would be required to cause 50% BMAA-dissociation from/glutamate-ligation to Zn^{2+} and Cu^{2+} metal centres, respectively (Nunn et al., 1989). The extent of BMAA-divalent cation complexation was also demonstrated in Glover et al., (2012), where dilute solutions of TCA, $MgCl_2$, NaCl, $CuCl_2$, $ZnCl_2$, or artificial ocean water reduced BMAA-attributable MS transitions by 78.0-99.7%.

In order to counteract the increased loss of DNS due to hydrolysis resulting from increases in reaction pH and temperature, an increased DNS concentration was utilized (7 mg mL^{-1} ACN). Previous studies noted that a DNS concentration of 5 mg mL^{-1} ACN, as opposed to the concentration of 1 mg mL^{-1} ACN, generated quantification transitions with twice the intensity; however, the lower concentration was ultimately utilized due to concerns over chromatographic interference (Salomonsson et al., 2013). Increased interference from salts resulting from the increased DNS concentration we utilized were abrogated by a centrifugal filtration step subsequent to derivatization, which was found to improve the elution profile of target compounds without affecting signal strength.

2.4.4 SIL internal standard stability and variability

The use of ^{15}N-BMAA as a SIL internal standard and the increased derivatization-buffer pH employed are improvements on a previously reported method for the quantification of BMAA that utilized deuterated internal standards, and/or isotope labelled compounds other than

BMAA (Fig. 2.4)—including $^{2}H_3$-DAB, $^{2}H_3$-BMAA, and $^{2}H_3$,^{15}N2-BMAA (Glover et al., 2015; Roy-Lachapelle et al., 2015; Faassen et al., 2016).

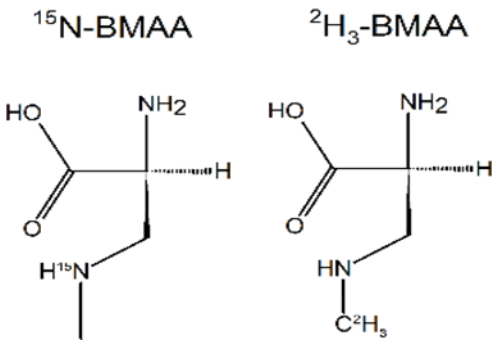

Figure 2.4: SIL internal standards used for HPLC-MS/MS assays

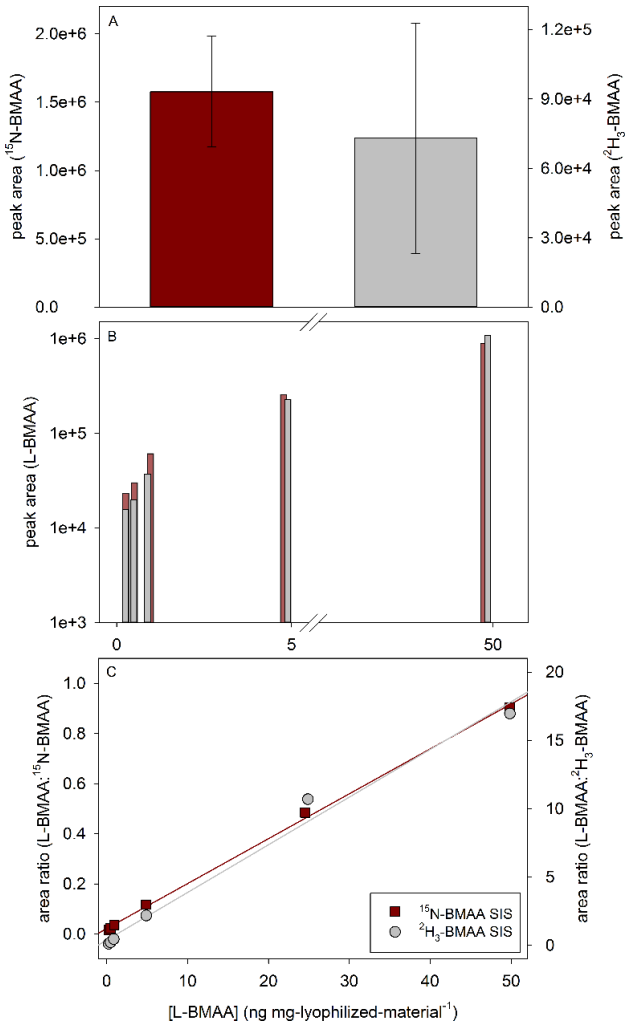

Figure 2.5: Comparison of ^{15}N-BMAA to $^{2}H_3$-BMAA as SIL standards in replicate samples for DNS analysis of BMAA via HPLC-MS/MS, SIL standard spiked into reference matrix at 50 ng mg^{-1} lyophilized material: (A) mean peak area and mean deviation of quantification transitions from replicate samples (n>15); (B) peak area of BMAA quantification transition from standard curves based on ^{15}N-BMAA vs $^{2}H_3$-BMAA SIL standards; (C) area ratio (BMAA:SIL standard)

The quantification transition of ^{15}N-BMAA generates a much more robust (>20:1 peak area) and stable (25.8% vs 68.2% mean deviation of peak area) signal than $^{2}H_3$-BMAA (Figure 2.5A), and does not interfere with the detection of BMAA despite the decreased mass separation between ^{15}N-BMAA and BMAA vs. $^{2}H_3$-BMAA and BMAA (Figure 2.5B).

The decreased response ratio and large variability in signal strength observed for the deuterated SIL internal standard are presumably due to hydrogen-deuterium (H/D) exchange of the deuterium-tagged γ-methyl group of $^{2}H_3$-BMAA during sample work up for total BMAA, resulting in both decreased SIL standard concentration and variability thereof (Fig. 2.5C).

Under both acidic and basic aqueous conditions—such as those that occur during the proteolysis and derivatization steps of the sample workup procedure for total BMAA, respectively—H/D exchange of methyl protons with water is known to occur (Zoltewicz & Kandetzki, 1971; Kim & Lim, 1991; Lo et al., 2007). Under neutral to acidic conditions BMAA forms very stable coordination complexes with divalent cations, with diaminoethane-like ML_2 binding geometry being preferred (Fig. 2.6A); this likely facilitates the H/D exchange of γ-methyl protons in $^{2}H_3$-BMAA with water (Lo et al., 2007; Glover et al., 2012). Additionally, under more basic conditions and in the presence of bicarbonate—as occurs during sample derivatization—BMAA spontaneously forms carbamate adducts, with the more favourable β-carbamate adduct rapidly cyclizing (Fig. 2.6B) to form a stable 1-methyl-2oxoimidazolidine-4-carboxylic acid (cycBMAA) intermediate, which further promotes H/D exchange (Zoltewicz & Kandetzki, 1971; Kim & Lim, 1991; Downing & Downing, 2016; Zimmerman et al., 2016).

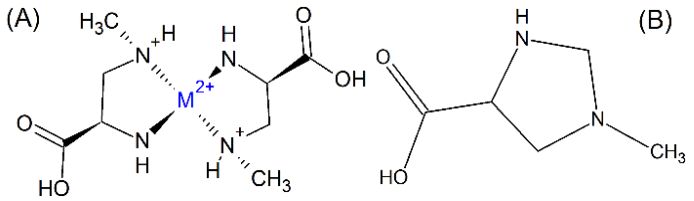

Figure 2.6: (A) predicted predominant BMAA coordination complex formed in the presence of divalent cations, (B) 1-methyl-2oxoimidazolidine-4-carboxylic acid (cycBMAA) intermediate formed from β-carbamate adduct of BMAA—compound formation likely favoured during dense bloom states when elevated pH activates BMAA β-amine as a nucleophile.

The equilibrium dynamics of BMAA and the associated carbamate adducts have only recently received attention as important contributors to the metabolism and function of BMAA in cyanobacteria, however, they may be key aspects of, and contributors to, the human neurodegenerative diseases associated with prolonged BMAA exposure. The dominant metabolite of the commonly prescribed, non-centrally acting angiotensin converting enzyme inhibitor, imidapril, is 1-methyl-2oxoimidazolidine-4-carboxylic acid (cycBMAA) (Matsuoka et al., 1992). Moreover, the activity of cycBMAA was shown to be 1.5–8 times more potent than thyroid-stimulating hormone as an inducer of T3/T4 production, resulting in increased metabolic cycling and hyperthyroidism—a known cause of reversible dementia that is strongly associated with increased Alzheimer's risk (Tan et al., 2008; Fazal et al., 2017).

2.4.5 Method implementation using environmental samples from off-channel sites of the Lower Columbia River, USA

The modified method was evaluated using nine sets of triplicate environmental samples, with quantification and verification of BMAA, AEG, DAB, and ANA-a based on the parameters given in Table 2.1. In all sample sets, BMAA was detected at concentrations above the limit of

detection (LOD), and for all but one site, was detected above the lower limit of quantitation (LLOQ); with measured concentrations ranging from 23.5±4.5 to 63.3±18.1 ng g^{-1} lyophilized material. The highest BMAA concentrations occurred at sites where cyanobacteria dominated the phytoplankton assemblage.

For six of the nine sample sets examined, DAB was present as concentrations above the LOD. However, only two of the sample sets produced quantifiable results, occurring in the sample sets in which the highest concentrations of BMAA were measured (Table 2.2). For all samples examined, neither AEG nor ANA-a were found above the limits of detection.

Table 2.2: Method application using Lower Columbia River, USA, environmental samples

Site	Date	[BMAA]	[DAB]
		(ng g^{-1} lyophilized material)	
Ilwaco Slough	06/28/16	34.0±5.7	ND
Welch Island	05/10/17	24.5±17.5	ND
Whites Island	07/06/16	<LLOQ (~4.5±0.5)	<LLOQ (~5.9±4.1)
Whites Island	06/21/17	28.5±1.5	<LLOQ (~6.2±3.5)
Campbell Slough	06/30/16	23.5±4.5	ND
Campbell Slough	06/20/17	50.5±9.5	26.7±12.0
Franz Lake Slough	06/30/16	33.0±11.4	<LLOQ (~10.2±7.0)
Franz Lake Slough	06/30/16	38.7±13.1	<LLOQ (~16.6±11.2)
Franz Lake Slough	06/20/17	63.3±18.1	36.6±2.1

2.5 Conclusions

As the human health impacts resulting from exposure to the cyanobacterial metabolite, BMAA, are postulated to be cumulative and since the regularity and severity of cyanobacteria blooms continues to increase, the development of cost effective methods for the accurate detection and quantification of BMAA is of paramount importance. Here, we demonstrate two areas where methodological uncertainties can originate and propose solutions to each: (1) reaction pH and (2) choice of appropriate internal standard. For the first requirement, it is critical that alkaline pH be maintained during DNS derivatization of BMAA, AEG, and DAB to improve reaction yields, as evidenced in the larger MS/MS quantification peak area observed under more alkaline conditions. Regarding the SIL standard selection, a ^{15}N-labelled internal standard resulted in much smaller signal loss compared to a ^{2}H-labelled standard, since the latter can undergo H/D-exchange during sample workup for total BMAA. Overcoming methodological issues may resolve some of the historic disagreement regarding the presence and concentration of BMAA in environmental and tissue samples.

3. High-resolution pressure nephelometry: utilizing gas vesicles as a robust and expanded means of determining growth and metabolic fluxes in planktonic cyanobacteria[2]

3.1 Abstract

Previous work has demonstrated that the physical properties of intracellular bacterial gas vesicles (GVs) can be analyzed *in vivo* using pressure nephelometry, and that the relative pressure at which GVs collapse is a measure of the physiological condition of the organism. In analyzing the buoyant state of GV-containing cyanobacteria, hydrostatic pressure within a sample cell is increased in a stepwise manner, where the concomitant collapse of GVs and resultant decrease in suspended cells are detected by changes in nephelometric scattering. As buoyancy modulation in cyanobacteria acts as the physiochemical link between nutrient and energy pools in stratified water column conditions, and the production of cyanotoxins has been linked to stressors associated with the disruption metabolic cycles linked to diel vertical migrations, pressure nephelometry is a powerful tool for monitoring the ecophysiological state of cyanobacteria. We have designed an automated pressure nephelometer that utilizes Vis-IR spectra to accurately quantify GV collapse pressure and cell turgor pressure. Herein we demonstrate that GV collapse pressure is stable under balanced growth—providing a rapid means of assaying population dynamics—and introduce pressure sensitive turbidity as a more robust metric than photopigment fluorescence for quantifying bloom forming cyanobacteria with complex phytoplankton populations. Applications of this instrument focus on physiological and ecological studies of cyanobacteria, for example HAB dynamics and the drivers associated with algal toxin production in aquatic ecosystems.

[2] Dyer, S.W., & J.A. Needoba. *Applied & Environmental Microbiology*: submitted 01/12/19 (responding to reviewers)

3.2 Importance

The increased prevalence of bloom forming cyanobacteria and associated risk of exposure to cyanobacterial toxins through drinking water utilities and recreational waterways are growing public health concerns. Cost effective, early detection methodologies specific to cyanobacteria are crucial for mitigating these risks; with currently available instrumentation suffering from poor detection limits and a lack of organism specificity. Here we present a multiplexed instrument capable of quantifying the relative abundance of cyanobacteria within complex environmental samples based on the signal generated from the presence of intracellular gas vesicles specific to bloom forming cyanobacteria. Additionally, the measurement furnishes information about the metabolic status and nutrient history of the cyanobacterial population—important factors for routine waterway monitoring and the mitigation of human health threats due to cyanobacterial blooms.

3.3 Introduction

Over their extended evolutionary course, cyanobacteria have developed a surfeit of metabolic strategies and modes of taxis enabling them to colonize, and thrive in, every niche and environement found on the globe (Puente-Sánchez et al., 2018). The planktonic cyanobacteria that regularly dominate Harmful Algal Blooms (HABs) utilize regulated flotation via buoyancy modulation to access limiting nutrients from depth, especially in stratified water column conditions (Jarrell & McBride, 2008; Paerl & Huisman, 2008). For planktonic cyanobacteria, positive buoyancy results from the synthesis of gas vesicle proteins (GVPs) that self-associate to form hollow, gas-filled inclusion bodies termed gas vesicles (GVs), while negative buoyancy results from an increase in dense cellular material accumulated via photosynthetic carbon fixation. A comprehensive review of gas vesicle structure and function, as well as more recent

molecular characterizations, can be found in Walsby (1994), and Mlouka et al., (2004) and Pfeifer (2012), respectively.

Regulated flotation as a mode of taxis greatly benefits cyanobacteria residing within thermally-stratified, lentic systems, as the rate of GV-driven vertical migration increases in tandem with water temperature—ultimately far surpassing the rate of vertical migration observed in motile microbes—and increasing surface water temperatures drive increases in the depth and stability of thermocline boundary layers (Ibelings et al., 1994; Brookes & Ganf, 2001). Increasing water temperatures caused by a warmer climate are predicted to strengthen stratification in freshwater environments, and therefore promote the growth of cyanobacteria that use buoyancy-mediated migration (Santer et al., 2019). Together, these changes are expected to generate a selective advantage in gas vacuolate cyanobacteria over non-buoyant phototrophs in the competition for nutrients at depth and light near surface boundary layers (Elliot et al., 2006; Jöhnk et al., 2008; Dervaux et al., 2015). Previous studies have demonstrated that toxin producing cyanobacteria gain a competitive advantage over their non-toxin-producing counterparts under the high light and oxidative stress conditions that develop within blooms, and that bloom states promote the induction of cyanobacterial carbon concentrating mechanisms (CCMs), stressosome responses, and osmoregulatory systems that synergistically act to alter bulk metabolite fluxes—further promoting cyanobacterial dominance and increased food web perturbations, as well as the risk of human exposure to cyanotoxins (Pané-Farré et al., 2005; Marles-Wright et al., 2008; Van de Waal et al., 2011; Daley et al., 2012; Rohrlack et al., 2013; Meissner et al., 2015). Thus, pressure nephelometry—which is able to rapidly and inexpensively assay GV characteristics and analyze cellular energetic status via determination of cell turgor—is a promising and underutilized methodology for the analysis of cyanobacterial physiology, the

monitoring of HAB dynamics, and the mitigation of human health threats associated with cyanobacterial blooms.

The physical properties of GVs can be examined via pressure nephelometry, from which a number of metrics with important ecological consequences can be derived (Walsby, 1971; Walsby, 1980). In bacteria possessing a cell wall, the variable osmolarity of the cell's interior vs the osmotic pressure (π) exerted by the external milieu establishes a turgor pressure (Pt) based on the solute potential of the cell (Ψ_s) and the hydraulic conductivity (Lp) of the cell surface (Kiil, 1989; Rojas & Huang, 2018). This turgor pressure is balanced by stress in the cell wall, in a relationship described by Young's elastic modulus (ε)—a measure of three-dimensional stiffness possessing the same units as turgor (i.e. force per unit area) that is most regularly employed in cell physiology to describe volume-to-turgor relationships, while also furnishing information about the mechanical properties of cells (Guz et al., 2014). Cell turgor and the associated mechanics are intricately linked to osmoregulation, cellular elongation and differentiation events, regulation of endocytosis and signal transduction pathways, etc., (Epstein et al., 1990; Whatmore & Reed, 1990; Wood, 2015). Thus, the close monitoring of turgor and the determination of deviations from a baseline value can be used as indicators for changes in cellular metabolism. Change in turgor pressure as an indicator of cellular metabolic status is likely a universal phenomenon, for example, recent reports have utilized turgor pressure deviations as markers for cellular abnormalities correlated with human disease (Castellani et al., 2001; Guz et al., 2014).

In order to provide buoyancy, the absolute (Pc) critical collapse pressure (CCP) of GVs (i.e. the innate critical pressure in the absence of turgor) must exceed Pt, thus providing a means of describing the mean *effective* CCP (Pe) of intact GVs within turgid cells, resulting in the relationship: $Pe = Pc - Pt$. The implication of this is that a non-permeable solute that exerts a

known osmotic pressure (i.e. sucrose: π = -2.75 MPa mol^{-1} at 20°C) can be used to remove Pt by increasing the external osmolarity, and if Pe is measured over a range of external solute concentrations such that the resultant Pt ranges between unity and zero, and if Pt decreases linearly with increases in π without causing cell lysis, then Pt, Ψ_s, Lp, and ε can all be directly calculated via pressure nephelometry, resulting in a snapshot of metabolic status (Walsby, 1980; Holland & Walsby, 2009).

While pressure nephelometry is a robust means of directly determining cellular turgor and the CCP of GVs in cyanobacteria, a linear relationship between Pt and π across the range of sucrose concentrations needed to fully remove turgor has yet to be demonstrated. Previously, this technique required the concentration of cells via accelerated flotation in order to produce a detectable signal, was unable to quantify cellular abundance, and was hindered by the available technology for pressure regulators, light sources and nephelometric detectors. Here we present an updated pressure nephelometer design that: a) improves precision in the measurement of CCP and critical collapse pressure distribution (CPD), b) demonstrates the stability of CCP and CPD during balanced growth, c) provides evidence of a linear decrease in CCP across the full range of turgor, d) introduces pressure sensitive turbidity (PST) as a quantitative metric for the abundance of gas vacuolate organisms, and e) demonstrates that PST can be directly used to track cyanobacterial growth and explore cyanobacterial physiology.

3.4 Methods

3.4.1 Automated Pressure nephelometer

The basic premise of pressure nephelometry for the applications described above is to increase the pressure applied to suspensions of cyanobacterial cells and concomitantly monitor

cell abundance via nephelometric scattering (Figure 3.1). As the applied pressure increases and GVs collapse, cells sink out of the interrogation region and the measured turbidity decreases. In practice, gas vacuolate cells in a monoculture sink out over a narrow pressure range within the broader range examined (0-150 psi), owing to the biomechanical properties of their GVs, resulting in characteristic and reproducible CCP and CPD values. Our programmable pressure nephelometer is comprised of six main systems: a pressure source equipped with a coarse pressure regulator, a secondary electronic proportional pressure transducer (EPP4; Parker Hannifin, Richland, MI, USA), a programmable multifunction I/O module for system synchronization (X-series DAQ; National Instruments, Austin, TX, USA), a collimated chip-on-board (COB) infrared (IR) light-emitting-diode (LED) light source (LZ4-IR; LED Engin, San Jose, CA, USA), and a wavelength-resolved CCD-based spectrophotometer (USB-Flame; Ocean Optics, Largo, FL, USA). All systems are programmatically controlled and communicate via the multifunction I/O module, and all spectral acquisition and processing is automated via a suite of LabView^{TM} virtual instruments (see Figure 3.2).

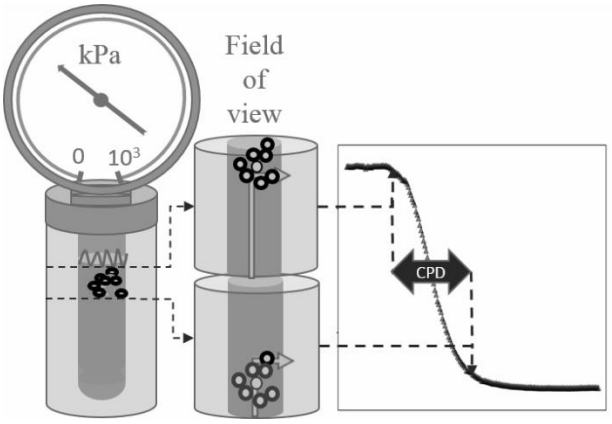

Figure 3.1: Visualization of the pressure nephelometer interrogation region—placed just below the air-water interface. In dense monocultures, scattering decreases as GVs collapse and cells fall out of the field of view (5 mm), resulting in a sigmoid collapse pressure distribution.

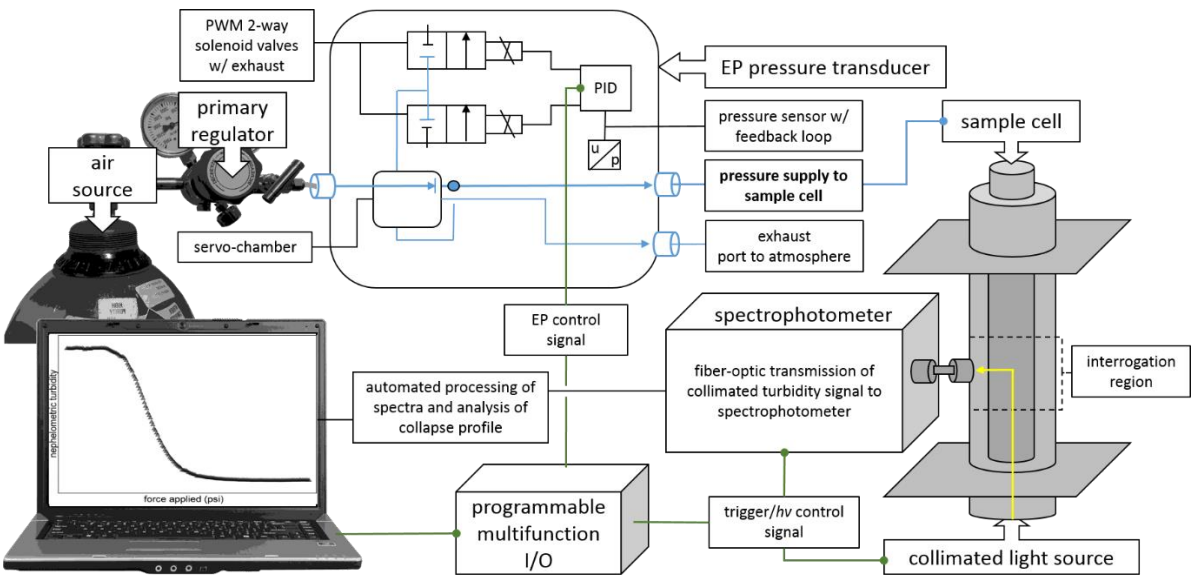

Figure 3.2: Schematic detailing the operation of the programmable pressure nephelometer. Control circuits, and pressure and light pathways are indicate in green, blue and yellow, respectively.

Hardware-level synchronization of systems is provided by a shared clock source with a 20 MHz frequency generator within the programmable 16-bit I/O module, allowing for nanosecond timing resolution (τ_r=10 ns) of triggering events. Triggering of the spectrophotometer is enacted on the rising edge of a square wave voltage signal (0-5V) from the I/O module, with the length of the square wave controlling integration time of the turbidity measurement. Concurrent to the rising edge of the square wave signal, the rising edge of a pulse-width modulated (PWM) square wave pulse train triggers an integrated circuit that drives the LED, with the duty cycle of the pulse train controlling light intensity. The falling edge of the square wave signal used to trigger and control the acquisition of spectra is used to establish timing for pressure increases, such that pressure increases always occur after the preceding, and prior to the subsequent, integration period and acquisition of spectra to allow equilibration of dissolved gasses in the sample. Response times for the light source and spectrophotometer are

<10 μs, while the response time for the EP pressure transducer is <2.6 ms psi^{-1}, resulting in a minimum cycle time per pressure step of <3 ms. System design adheres to all instrument requirements for nephelometric turbidity measurements as indicated in ISO7027: Water Quality—Determination of turbidity by nephelometry.

3.4.2 Cyanobacteria cultures

Axenic cultures of the unicellular, freshwater cyanobacteria *Microcystis* sp. PCC7806 obtained from the Pasteur Culture Collection of Cyanobacteria (Paris, FR), and a general *Microcystis* sp. obtained from Carolina Biological Supply (Burlington, NC, USA), were used for pressure nephelometry measurements. Cultures were grown in BG11 Medium at 15°C under a photosynthetic photon flux density of 30 μmol s^{-1} m^{-2} on a shaker table oscillating at ~75 rpm (Allen & Stanier, 1968). In line with previous reports, it was found that low photon irradiance promotes the production of cells with a high GV content, and agitation helps prevent colony formation and cell adhesion to surfaces (Oliver & Walsby, 1984).

3.4.3 Pressure nephelometry

Utilizing the change in nephelometric turbidity that occurs upon the collapse of GVs and the resultant decrease in suspended cells, CCP and CPD of GVs in *Microcystis* sp. were calculated, with minor alterations to prior methods (Walsby, 1980; Holland & Walsby, 2009). Automated pressure nephelometry measurements were made in triplicate for each data point, using 4 mL aliquots of culture. For culture experiments and the determination of mean effective CCP, CPD, and PST-inferred specific growth rate, as well as cell turgor pressure, pressure increments of 0.75 psi at 3000 ms intervals, and integration times of 1000 ms were utilized. For all measurements, the IR-LED was driven by a 100 Hz pulse train at a 30% duty cycle. Collapse

curves were generated by trapezoidal integration of nephelometric turbidity counts as a function of wavelength with respect to wavelength over the nephelometric wavelengths (860±30 nm); all data processing is automated via a suite of LabView^{TM} virtual instruments.

3.4.4 Critical collapse pressure and distribution

Multiple regression analyses of the raw collapse profiles using the Levenberg-Marquardt algorithm were performed for all measurements, based on fits to 4-parameter sigmoid functions of the form:

$$y = y° + a/\left[1 + e^{(-\frac{(p-Pe)}{b})}\right]$$

where $y°$ is minimum turbidity, a is the turbidity range, p is the force applied at some relative turbidity value y, Pe is the mean effective CCP indicated by the force applied at the inflection point of the curve, and b defines the gradient of the curve. The critical collapse pressure distribution was calculated as the relative change in pressure, centered about Pe that accounted for ≥95% of the change in turbidity due to pressure. As the automated measurement is both pressure and time resolved, and the size of plano-convex collimating lens of the interrogation region is known (5 mm), the CPD value can also be used to estimate sinking velocity (νs).

3.4.5 Pressure sensitive turbidity

Quantitative estimates of gas vacuolate organism abundance were made based on changes in PST. Utilizing the 4-parameter sigmoid fit of the critical collapse pressure distribution in culture measurements, PST was calculated as the integrand of turbidity as a function of pressure with respect to pressure.

3.4.6 Permanent slide preparation

Uncollapsed cultures were preserved using 10 % (v/v) Glutaraldehyde in BG11 at a final concentration of 1.0% and stored at 4°C overnight. Following preservation, 2-Hydroxypropyl methacrylate (HPMA) permanent slides were prepared, as in Crumpton (1987), for microscope analysis and counts. This method offers a number of benefits over the traditional inverted microscope method of Utermöhl, as GVs are known to maintain their structure and function (i.e. buoyancy) subsequent to preservation with Lugol's iodine and glutaraldehyde (Sundararajan & Ju, 2000; Nollet & De Gelder, 2013).

3.4.7 Photopigment fluorescence

In addition to pressure nephelometry measurements, in vivo measurements of chlorophyll-a and phycocyanin (PC) were collected using a benchtop laboratory fluorometer (Trilogy; Turner Designs, San Jose, CA, USA) for determination of specific growth rate (μ), determined from regression fitting to an exponential growth formula ($N=N_o e^{\mu t}$), where N_o is the initial growth metric (i.e. # cells/RFU/PST) and t is time in days.

3.4.8 Microscopy and cell counts

Micrographs were acquired on an AxioVert 200m microscope equipped with an Apotome imaging system (Carl Zeiss Microscopy; Thornwood, NY, USA). Replicate (n=6) phase contrast and confocal laser scanning micrographs (CLSMs) were collected at 400x total magnification for permanent slides corresponding to 0 and 72 hr time points (Figures 3.6/3.7). For CLSMs, a reflector module with a 546/12 nm excitation filter, FT 560 nm beam splitter, and 576-640 nm band pass filter were used, allowing for detection of phycobiliprotein and chlorophyll autofluorescence. For micrograph analysis the open-source software ImageJ was used. Briefly, for cell counts using the CSLMs based on fields of view (FOV), artifacts smaller than 2 pixels

were removed as noise, and object surface area maps were generated using the 3D Object Counter plugin (Cordelires & Jackson, 2005) and a uniform threshold level. The object area maps were then used to derive cell counts per FOV, utilizing the mean cell diameter (n=25) and the calculated 2D area of the cells—approximated as spheres. Cell counts are reported as the mean number of cells per FOV, with the error reported as the standard error about the mean.

3.4.9 Statistical analysis and graphics

The results of replicate measurements are expressed as the mean ± the standard deviation (SD) about the mean for metrics derived from regression fittings. For regression analysis and fitting of data, the coefficient of determination (R^2), the standard error about the mean (S) are reported. Data processing of nephelometric spectra for the pressure nephelometry measurements was performed using a suite of LabView virtual instruments. The generation of graphics and subsequent formatting were performed in SigmaPlot 13.0 and Gnu Image Manipulation Platform (GIMP 2.8.14), respectively.

3.5 Results and Discussion

3.5.1 Pressure nephelometer

A number of confounding factors associated with accurately and precisely determining the effective CCP of gas vesicles in turgid cells have previously been reported (Walsby, 1980). One aspect contributing to inaccuracy is the use of white light sources, which create convective cycling and were found to alter the turbidimetric scattering by as much as 18% of baseline values (Walsby, 1973). Moreover, white light sources emit the total complement of UV-Vis wavelengths known to drive photosynthesis and elicit metabolic regulatory effects in cyanobacteria, and therefore lead to physiological changes during the measurement period

(Castenholz & Garcia-Pichel, 2012). The stability of the IR LED, and GV-associated turbidity signal prior to collapse were determined from an overlay of replicate nephelometric spectra (n=10; $\Delta p = 0.75$ psi) recorded at the start of a collapse measurement utilizing a *Microcystis* PCC7806 culture (Figure 3.3). Baseline turbidity values vary less than 0.5% (data not shown). The use of an LED with emission centered over the nephelometric wavelengths minimizes several sources of error including: light attenuation, increases in thermal kinetic energy within the sample, changes in buoyancy due to photosynthetic carbon fixation, and the requisite integration time per acquisition. The optical elastic scattering properties of the nephelometric wavelengths also results in a much larger linear turbidity range than is achievable with white light sources.

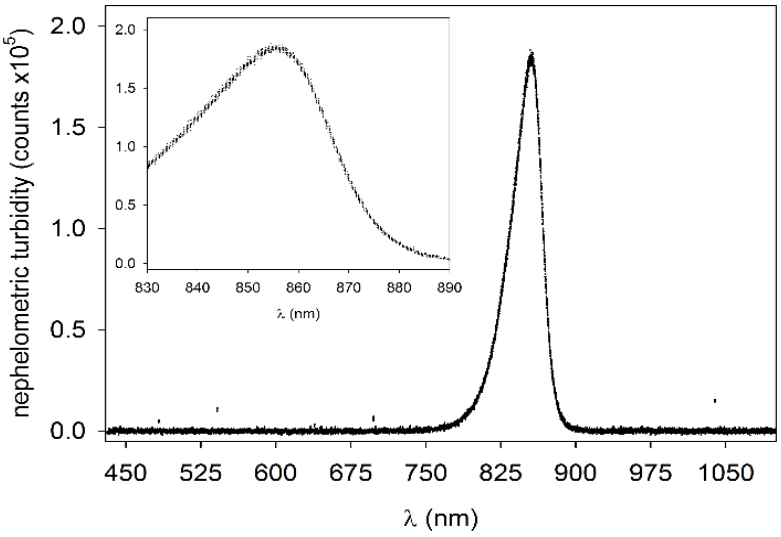

Figure 3.3: overlay of raw nephelometric spectra at the start of a collapse measurement (10 spectra; $\Delta p = 0.75$ psi); (insert) The IR LED has a narrow emission profile centered over the nephelometric wavelengths (860±30 nm).

The improved scattering properties and lowered minimum integration time arising from the IR LED facilitates the use of the electronic pressure transducer characteristics, including

millisecond response times between pressure steps (>3 ms psi^{-1}) and enhanced pressure resolution (>0.1 psi $step^{-1}$). Previous manual pressure nephelometer designs were constricted to pressure steps of approximately 0.05 MPa (7.25 psi), and relied on human accuracy and timing in enacting pressure steps at consistent and precise intervals, with both factors effecting the interpretation of GV collapse measurements and the accuracy of calculations (Table 3.1). The EP transducer dynamically senses and regulates pressure at each fixed pressure increment and therefore corrects for small pressure changes caused by air-water gas equilibration, which negates the need to minimize head space and maximize sample volumes as was necessary previously. Without these gas diffusion issues a sample volume resulting in a meniscus just above the interrogation region can be used. This further increases the sensitivity of the pressure nephelometry measurement by capturing changes in nephelometric scattering due to both the collapse of GVs and the resultant loss of cells with collapsed GVs as they settle out of the interrogation region (Figure 3.1).

Table 3.1: Comparison table for pressure nephelometry performance metrics

organism	**Pe (psi) intraday**	**Pe (psi) steady state growth**	**Pt (psi)**	**Pc (Psi)**	**critical pressure distribution (psi)**	**reference**
Microcystis sp. (this study)	72.33±0.02	72.34±0.65	44.51±0.41	116.84±0.41	36.35±3.00	-
Microcystis BC8401 (manual pressure increments)	63.8±NA	NA	46.4±NA	111.7±10.2	~50±NA	[57]

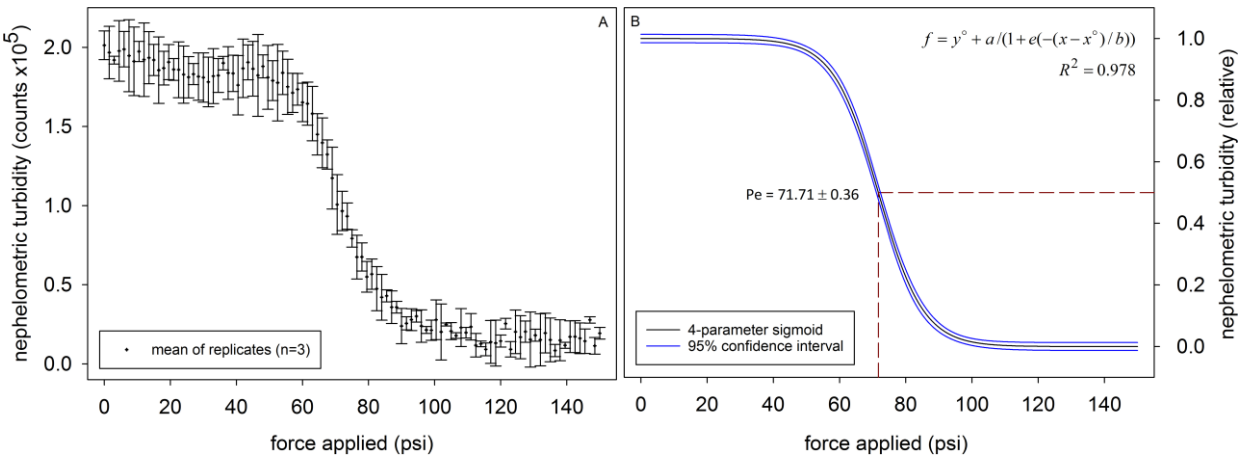

Figure 3.4: (left) GV collapse profile of replicate Microcystis aeruginoa PCC7806 cultures, data points indicate the mean of triplicate values generated by trapezoidal integration of raw nephelometric spectra collected at increasing pressure increments (ΔP = 1.5 psi), error bars indicate standard error of raw values from triplicate measurements; (right) 4-parameter sigmoid regression fitting of replicates, intercept of dashed line with x-axis indicates the mean effective critical collapse pressure (Pe=71.71 ± 0.36 psi).

The improved linearity and accuracy of pressure steps are important advancements that allow higher resolution in the CCP measurement. Previous studies have shown that large pressure steps cause changes in cell volume upon the rapid collapse of a large fraction of GVs, and if a subsequent pressure increment is applied prior to the cells regaining turgor, the effective CCP becomes artificially inflated (Reed & Walsby, 1985; Holland & Walsby, 2009). Moreover, the decreased magnitude and response time of pressure increments greatly improves the repeatability of the GV collapse measurement (Figure 3.4), and the uniformity of critical pressure distributions, in addition to eliminating uncertainties arising from the acquisition of spectra during dynamic increases in pressure. These advancements allow for direct comparisons between replicate cultures or treatments to be made, both intraday and over the course of

balanced growth, and demonstrate the stability of Pe during balanced growth as determined from replicate cultures, whereas previous studies were restricted to intraday, replicate collapse measurements of a singular culture (Table 3.1).

3.5.2 Critical collapse pressure and distribution

As in the example given in Figure 3.4b, the mean effective CCP of GVs in turgid *Microcystis* PCC7806 cells of 71.71±0.36 psi is in line with the reported value for the common laboratory strain, *Microcystis* BC 8401 of 67.88 psi, based on the quasi-continuous measurement method (Holland & Walsby, 2009). The observed CPD in *Microcystis* PCC7806, representing >95% change in nephelometric scattering as a function of pressure, calculated from triplicate collapse measurements, was found to be much more constrained (CPD=36.35±3.00 psi) than in previous reports utilizing *Microcystis* BC 8401 (CPD ≅ 50±NA psi). Based on literature reports for the positive sinking velocity (ν_s) of *Microcystis* sp, and utilizing the height of the plano-convex collimating lens (5 mm) and the time resolved CPD, the inferred sinking velocity of *Microcystis aeruginosa* PCC7806 (ν_s=34±3 μm s^{-1}), falls well within the range of reported rates 10-120 μm s^{-1} (Reynolds et al., 1987; Sullivan et al., 2011)

3.5.3 Critical collapse pressure and growth

Previous methods for measuring CCP were unable to generate reproducible results except when samples were taken from the same culture flask, owing to inherent differences in culture and organism conditions; for example, cultures of different ages with variable pigmentation that changed white light attenuation and scattering properties (Holland & Walsby, 2009). Thus, turbidity measurements were historically viewed as qualitative in nature, while more recently developed turbidity measurement methods can be used in quantitative capacities (Bin Omar &

Matjafri, 2009). In accord with ISO7027: Water Quality—Determination of turbidity: Quantitative methods—the use of fiber optics and a high power, narrow emission profile LED maximizes scattering intensity and minimizing interferences from: color, particle density, particle size, and stray light. This allows for comparisons of GV physical properties to be made between replicate cultures, both intraday and over the course of growth. From triplicate collapse measurements utilizing *Microcystis* sp. cultures recorded at 24 to 72 hour intervals over a complete growth cycle (i.e. lag, exponential, inflection, and stationary phases), we found the mean Pe of 72.34±0.65 psi to remain constant during steady state growth (Figure 3.5b), and to closely match that of *Microcystis* PCC7806 cultures (Pe=71.71±0.36 psi) maintained under the same conditions (Figure 3.4b). Slightly higher and lower CCP values were noted during lag and stationary phases, respectively, and CPD was found to remain constant throughout the course of measurement (data not shown).

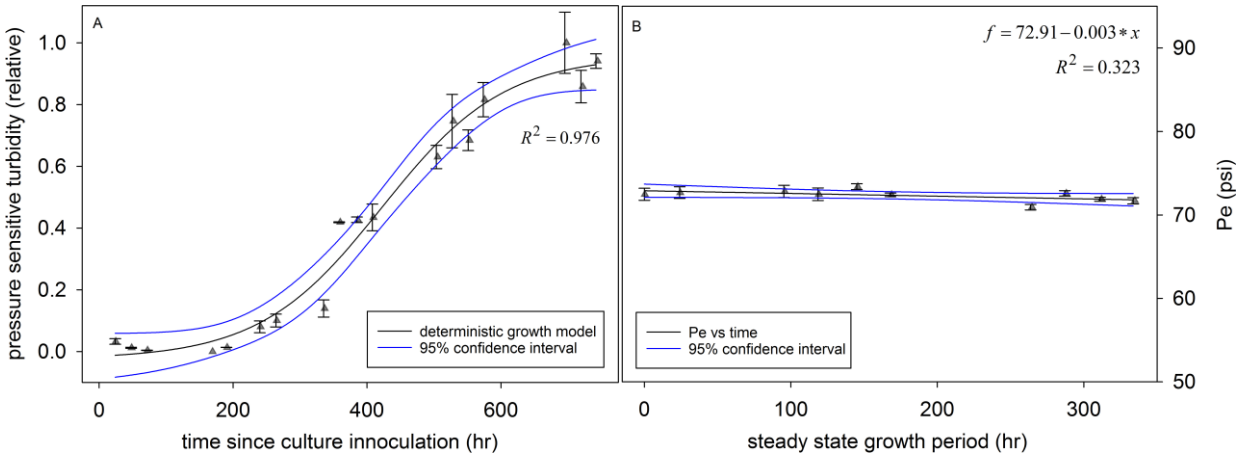

Figure 3.5: (A) pressure sensitive turbidity (PST) is a proxy for the abundance of GV-containing cyanobacteria, used here to track growth in a Microcystis sp., culture; (B) the change in mean effective critical collapse pressure (Pe = 72.34 ± 0.65 psi) is well constrained by the error of triplicate collapse measurements and remains constant during exponential growth.

3.5.4 Pressure sensitive turbidity and growth

Decreased light interferences and attenuation also allow for quantitative estimates of gas vacuolate organism abundance to be made based on changes in PST due to growth; here shown in axenic cultures of *Microcystis aeruginosa* PCC7806 (Figure 3.6/3.7). Specific growth rate (μ) based on PST was found to be strongly correlated with that of Chl-a and PC (R=0.995 and R=1.000, respectively; $p<0.001$). Further, based on cell counts at 0 and 72 h (90±45 and 159±46 cells FOV^{-1}, respectively; $\mu=0.190$), PST was the most accurate predictor of growth (Figure 3.6; $\mu=0.176$), thus indicating that PST is a valid proxy for the abundance of gas vacuolate organisms. Moreover, the change in inferred biomass during the course of measurement was accompanied by 220% increase in the integrated PST signal, as compared to the relative increases in fluorescence for Chl-a and PC of approx. 20% and 100%, respectively, observed during the same period (Figure 3.6). Thus, the PST measurement may be a more sensitive metric than photopigment fluorescence in assaying growth in buoyant cyanobacteria.

In addition, during strong illumination and periods of nutrient limitation, the degradation of highly-colored phycobilisome antenna pigments occurs in cyanobacteria, resulting in chlorosis, which decreases the utility of *in situ* fluorescence as a measure of cyanobacteria biomass (Hickman et al., 2013; Liu et al., 2013; Kopf et al., 2015). As such, photopigment fluorescence is a relatively poor marker for cyanobacterial abundance during bloom conditions, while gas vesicles remain necessary for continued growth and vertical migration. Thus, CCP and PST may be better proxies for metabolic activity and biomass, respectively, in cyanobacterial populations during HAB conditions (further assessed in Chapter 5).

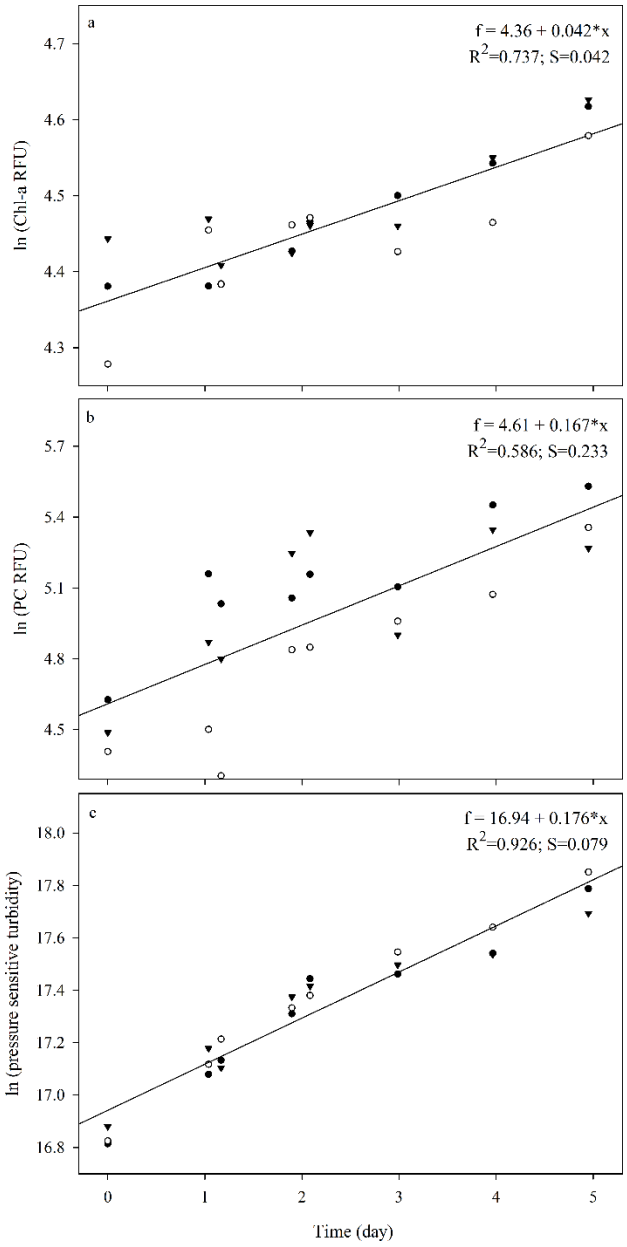

Figure 3.6: Regression analysis of specific growth rate (μ) using: (a) Chl-a (μ=0.042) and (b) PC (μ=0.167) RFU, and (c) PST (μ=0.176) in axenic Microcystis aeruginosa PCC7806 cultures. The observed specific growth rate based on PST is strongly correlated with both Chl-a and PC (R=0.939 and R=0.947, respectively; p<0.001). From cell counts at 0 and 72 hr (90±45 and 159±46 cells, respectively), PST-derived μ was found to most accurately approximate the growth rate based on physical counts (μ=0.190).

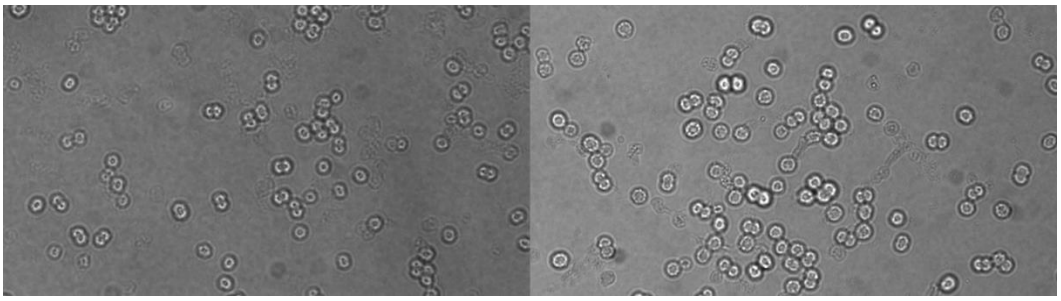

Figure 3.7: Phase contrast HPMA micrographs of axenic Microcystis aeruginosa PCC7806 cultures preserved at: (left) 0 and (right) 72 hr time point (Fig 5); gas vesicles clearly present as intracellular refractile bodies; panes 121x121 μm.

3.5.5 Determination of turgor and metabolism

The indicated instrument modifications allow for direct comparison of changes in the abundance of intact GVs in culture conditions, capturing both the shape and location of inflection points corresponding to collapse thresholds under different turgor conditions and applied pressures (Figure 3.8). Where changes in cell turgor—measured as the change in Pe in response to changes in external osmolarity—between treatments can be calculated from any relative turbidity value (0-to-1), thereby highlighting the usefulness of gas vesicle CCP as a quantitative benchmark for shifts in metabolism.

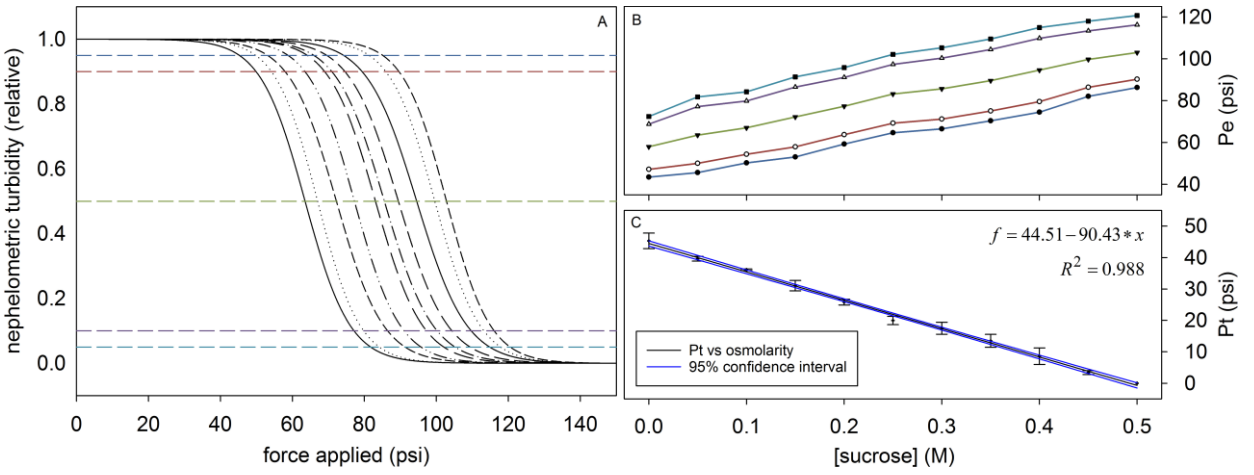

Figure 3.8: (A) Microcystis sp. collapse curves, from left to right, at sucrose concentrations of 0, 0.05, 0.10, 0.15, 0.20, 0.25, 0.30, 0.35, 0.40, 0.45, and 0.50 M, respectively. From top-to-bottom, thresholds corresponding to collapse of 5, 10, 50, 90, or 95-percent of the GV content; critical pressure values given by x-axis intercepts where dashed lines cross collapse curves; (B) linear increase in effective critical collapse pressure due to increasing external osmotic pressure (i.e. decreased Pt) determined at 5, 10, 50, 90, or 95-percent thresholds, demonstrating that GVs respond in a uniform and predictable way to changes in Pt; (C) linear decrease in Pt due to increasing osmotic pressure, calculated as mean relative change in Pe for all collapse thresholds, as shown in (B), demonstrating that Pe can be used to track changes in Pt (Pt = 44.51 ± 0.41 psi), and can therefore be used to directly assay changes in metabolic fluxes that influence turgor.

The effective CCP and turgor pressure were found to linearly increase and decrease (Figures 3.8b and 3.8c, respectively), with respect to external osmotic pressure, while the gradient of the sigmoid fits (*b*) and CPD were found to remain constant across the full range of sucrose concentrations examined. The stability of *b* and CPD indicate that the shift in Pe was due solely to removal of Pt. Thus, the change in Pe due to increased external osmolarity can be used to directly calculate cell turgor in the *Microcystis* sp. cultures we examined (Pt = 44.51±0.41 psi). Previous studies have demonstrated an inverse correlation between the strength and width of GVs in cyanobacteria owing to the protein primary structure of GVPs, resulting in species-specific Pe values (Hayes & Walsby, 1986; Mlouka et al., 2004; Dunton & Walsby, 2005; Dunton et al., 2006). Given that Pe varies linearly with respect to Pt, and as the external osmolarity experienced by cells in the environment can be assumed to be equivalent at any discrete point in time, it follows that pressure nephelometry can be used to track changes in the

bulk chemical properties of aquatic systems via a conserved shift in Pe across populations. Moreover, changes in Pe as a result of Pt may allow for quantitative analysis of the metabolic fluxes associated with photosynthesis in gas vacuolate organisms (Figure 3.9).

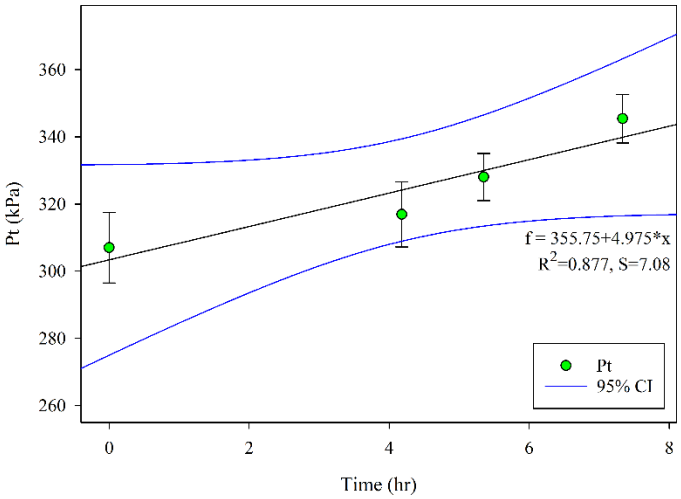

Figure 3.9: Intraday increase in Pt determined from the decrease in Pe in replicate (n=3) Microcystis aeruginosa PCC7806 cultures due to photosynthesis. The change in intracellular osmotic pressure (38.4±9.0 kPa) as determined by the change in Pt is a quantitative metric that can be used to assay metabolic fluxes in gas vacuolate organisms.

In addition to improving linearity over the course of collapse measurements, the precise application of minute pressure increments when examining environmental HAB samples indicates that the system is able to detect the presence and relative abundance of discrete cyanobacterial populations within whole-water environmental samples based on characteristic CCP and CPD values (described in Chapter 4). Following from which, changes in the metabolic status and selective advantage of a discrete subset of cells within mixed a population can be identified via a divergent change in CCP from the change observed in the rest of the gas-vacuolate population (demonstrated in Chapter 5). The simultaneous detection and

characterization of multiple bloom forming species via molecular techniques is a current area of focus in HAB management, however such molecular techniques still suffer from prolonged analysis times, elevated costs, and difficulties in detecting multiple species within a single multiplexed assay (Te et al., 2015; Otten et al., 2016). As gas vacuolate cyanobacteria are the dominant species within freshwater HABs, and critical collapse pressure is species specific, pressure nephelometry may provide a number of benefits over current molecular techniques; most notably the increased number of detectable targets, coupled with lower costs and analysis times.

4. The use of pressure nephelometry for rapid species identification and monitoring in mixed planktonic assemblages[3]

4.1 Abstract

Gas vesicles (GVs) are proteinaceous inclusion bodies that occur in a number of bacteria and archaea, including bloom forming cyanobacteria, pathogenic enterobacteria, antibiotic producing actinomycetes, and arsenic methylating halobacteria. To date, production of GVs has predominantly been linked to flotation, allowing for vertical taxis in aquatic niches by otherwise amotile organisms. Inter-organism differences in the primary structure of the main gas vesicle protein, GvpA, and the abundance and number of 33-residue repeats in the exterior scaffolding protein, GvpC, have been shown to alter the physicomechanical properties of GVs in the producing organisms. These properties can be analyzed in vivo via pressure nephelometry, where the application of pressure leads to the collapse of GVs and causes cells to sink vertically past a detection window equipped with a turbidity sensor. The critical collapse pressure (CCP) of GVs resulting from applied force alters turbidimetric scattering and generates a reproducible signal that is invariant during balanced growth and occurs over a narrow range of pressures. We show that pressure nephelometry can be used to separate and quantify discrete gas vacuolate populations within whole-water environmental samples on the basis of CCP, allowing for identification of different species in mixed microbial assemblages. As cyanotoxin biosynthesis occurs in a relatively limited set of cyanobacteria species, pressure nephelometry is a promising method for the rapid and cost-effective analysis of Harmful Algal Bloom (HAB) population dynamics, and the mitigation of HAB-associated human health risks.

[3]Dyer, S.W., L.P. Cook, T.D. Peterson, & J.A. Needoba. *Limnology & Oceanography Methods*: expected submission March, 2019.

4.2 Introduction

4.2.1 Cyanobacteria

Modern cyanobacteria are photosynthetic prokaryotes with evolutionary roots that extend back to the origins of photosynthesis (Schirrmeister et al., 2012; Nozaki et al., 2004). Cyanobacteria are known to rapidly adapt to environmental stressors through diverse processes including complementary chromatic adaptation, UV-radiation (UVR)-induced vertical migration, the formation of dissection-resistant microbial mats, and the synthesis of "sun-screening" and osmoprotectant compounds (Sinha et al., 2007; Moon et al., 2012; Wood, 2015; Walter et al., 2017; Rose et al., 2018). These stress responses and others relating to anti-herbivory or nutrient competition are responsible for the plethora of secondary metabolites—notably cyanobacterial toxins (cyanotoxins)—that together lend cyanobacteria a competitive advantage in many ecosystems (DeMott et al., 1991; Zimmer and Ferrer, 2007; Meissner et al., 2015; Frenken et al., 2018). The regular formation of cyanobacteria dominated Harmful Algal Blooms (cyanoHABs) is an emerging health concern effecting important freshwater reservoirs worldwide, and the upward trend in global average temperatures over the last century is likely to further promote cyanobacterial growth in these freshwater systems (Johnk et al., 2008; Michalak et al., 2012; Jiang et al., 2014; Pip et al., 2016; Tang et al., 2018; Santer et al., 2019)

4.2.2 Monitoring cyanobacteria species composition

The routine monitoring of aquatic resources for cyanobacterial abundance and cyanotoxin concentration has most often been carried out through microscopic counting coupled with chemical detection methods targeting a limited set of analytes (Ouellette and Wilhelm, 2003). This approach is hindered by a number of issues, including: (*i*) the morphological similarity of various form genera of cyanobacteria, making microscopic discrimination difficult, (*ii*) the fact

that some species are toxigenic, but only under certain circumstances, and (*iii*) the occurrence of benthic species as contributors to dissolved cyanotoxin concentrations (Casamayor et al., 2000; Kaplan et al., 2012; Bouma-Gregson et al., 2017). More recently, molecular techniques such as quantitative PCR and shotgun metagenomics have been utilized for the detection of a limited set of target organisms or analytes (Te et al., 2015; Otten et al., 2016). However, the genomes of cyanobacteria are highly malleable and multiple cyanotoxin gene clusters are flanked by insertion sequences, or miniature inverted-repeat transposable elements, resulting in the detection of non-toxin producing organisms by qPCR as a fraction of their toxin producing counterparts (Fewer et al., 2010; Meyer et al., 2017). Further, various species of cyanobacteria are known to harbor multiple complete chromosome copies (sometimes in the hundreds), that replicate asynchronously to cellular division, making associations between qPCR results and the effective environmental contribution of polyploidal cells to the total population difficult to determine (Jain et al., 2012; Watanabe et al., 2012). Additionally, the majority of the EPA drinking water Contaminant Candidate Listed (CCL) cyanotoxins are produced by non-ribosomal peptide synthetases and/or polyketide synthases (NRPS/PKS), which eschew ribosomal peptide synthesis and regulation, making it difficult to directly compare transcript levels to toxin production potential (Neilan et al., 2013; Weissman, 2015). Molecular techniques improve specificity as compared to microscopic identification and advance our understanding of factors influencing the production of cyanotoxins; however, they are still not rapid and do not lend themselves to routine monitoring applications. Thus, there is an urgent need for methods that are accurate, rapid, and can be scaled up to meet the demands of widespread monitoring efforts.

4.2.3 Gas vesicle structure

Gas vesicles are proteinaceous microcompartments devoid of lipids or carbohydrates that form regularly repeating amyloid fibril structures from the self-assembly of small amphiphilic GvpA monomers, resulting in a continuous cross β-sheet with strongly hydrophobic, and hydrophilic, interior and exterior faces, respectively (Strunk et al., 2011; Ezzeldin et al., 2012). A high degree of GvpA sequence similarity between diverse organisms has been noted (65.8% between *Anabaena flos-aquae* and *Halobacterium sp. NRC-1*), with the C-terminal segment of GvpA accounting for the majority of the observed variability (Walsby, 1994; Belenky et al., 2004). Molecular dynamic and mutation studies also indicate that the variable C-terminal portion of GvpA that contains α-helix-II is involved in the regulation of gas vesicle integrity (Mlouka et al., 2004; Strunk et al., 2011).

Despite small variations in protein primary structure, and the number or presence of multiple accessory proteins present in the operons of the producing organisms, the molecular framework of GVs is highly homologous between orthologs, as is the cylindrical-bicone shape of GVs (Walsby & Bleything, 1988; Knitsch et al., 2017). However, due to the sequence variability of GvpA, and the number of 33-residue repeats in GvpC—which interacts with α-helix-II of GvpA to stabilize GV quaternary structure—the length-to-width ratio of the GVs, and the mean critical collapse pressure (CCP) of GVs in various organisms has been shown to be distinct, in addition to remaining constant during periods of balanced growth (Walker & Walsby, 1984; Hayes & Walsby, 1986; Beard et al., 2002; Mlouka et al., 2004; Sievertsen et al., 2009/2010; S.W. Dyer & J.A. Needoba, in review). Previous morphological and molecular phylotyping studies have utilized the presence of GVs as a distinguishing feature between closely related

form-genera, with the molecular studies further proposing that the formation of GVs is of taxonomic importance at the species level (Eichler and Pfenning, 1988; Guyoneaud et al., 1998).

4.2.4 Pressure nephelometry

The premise of pressure nephelometry is to increase the hydrostatic pressure exerted on cellular suspensions within a sample cell by increasing the pressure in the head space, with concomitant monitoring of changes in cellular physicomechanical pro properties (i.e., GV structural integrity and cell buoyancy) being detected via changes in nephelometric scattering, as described previously (Walsby, 1971; S.W. Dyer & J.A. Needoba, in review). The change in nephelometric scattering due to the application of force has been termed Pressure Sensitive Turbidity (PST), and in axenic cultures occurs over a narrow Collapse Pressure Distribution (CPD), with the maximum rate of GV collapse and change in the rate of cell settling occurring at a characteristic CCP. Recently available technology has led to instrument advances relating to light sources, nephelometric detectors, and pressure regulators used in pressure nephelometer designs, allowing for quantitative estimates of particle density to be made, and nephelometric scattering to be measured within a narrow interrogation region located near the air-sample interface (Figure 4.1). These advances allow for the direct measurement of CCP and CPD of GVs based on the loss of cellular buoyancy, with detection occurring as cells pass through the interrogation region, as opposed being inferred based on changes in bulk light transmittance in concentrated samples subject to pervasive and variable light attenuation, as in prior designs. Programmatic instrument control and the detection of scattering within a narrow, fixed interrogation region also furnishes time resolved turbidity measurements, allowing for the estimation of settling velocity. The purpose of this research is to present evidence from pressure nephelometry experiments indicating that the presence of GV-containing organisms can be

determined through changes in PST, and that the distinct CCP/CPD associated with the PST changes can be used to rapidly delineate speciation in mixed microbial assemblages from environmental samples. Support for the interpretations of the pressure nephelometry results are given on the basis of microscopic examination of pressure fractionated samples.

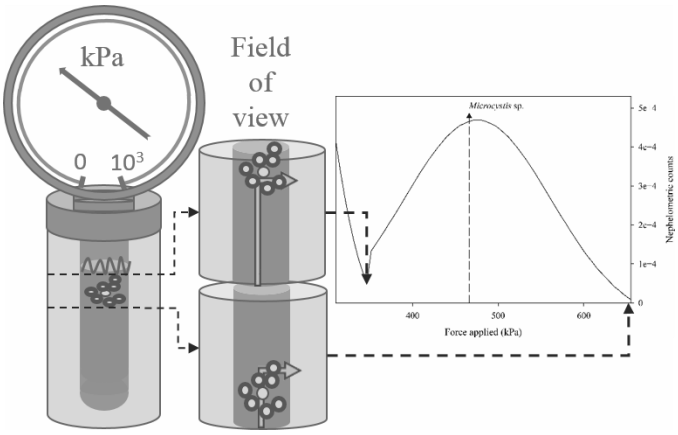

Figure 4.1: Pressure nephelometer schematic; scattering increases as GVs collapse and cells fall through the field of view.

4.3 Material and procedures

4.3.1 Automated pressure nephelometer

A detailed description of the high resolution pressure nephelometer is given elsewhere (Chapter 3; S.W. Dyer and J.A. Needoba, in review). Briefly, the instrument consists of an integrated: (i) pressure source and coarse pressure regulator, (ii) voltage-regulated EP pressure transducer for fine control of pressure steps, (iii) multifunction I/O module for system control and cross-talk, (iv) collimated IR LED light source with the emission profile centered over the nephelometric wavelengths (860±30 nm), and (v) CCD-based, Vis-IR spectrophotometer. The use of a high power IR LED and wavelength resolved spectrophotometer allow for quantitative

turbidity measurements to be made in accord with ISO7027: Water Quality—Determination of turbidity by nephelometry.

4.3.2 Cultures and environmental samples

Cultures of the aquatic freshwater cyanobacteria *Merismopedia* sp., *Anabaena* sp., and *Microcystis* sp., were obtained from Carolina Biological Supply (Burlington, NC, USA). Whole water environmental samples were collected from an off-channel site along the Lower Columbia River, USA, in 2016-18. For all culture and environmental sample maintenance and measurement, BG11 and BG11$^{1/2}$ mediums were used, respectively (Allen and Stanier, 1968). All samples were maintained at 15°C under a photosynthetic photon flux density of 30 μmol s^{-1} m^{-2} on a shaker table oscillating at ~75 rpm.

4.3.3 Pressure nephelometry

Pressure nephelometry measurements were performed, and collapse spectra—corresponding to the change in nephelometric turbidity as a function of applied pressure—were generated, with slight parameter modifications to previously described methods (S.W. Dyer & J.A. Needoba, in review). All transfers were performed utilizing sterile culture techniques. Dense cultures and environmental samples were diluted at ratios of 1:20 and 1:25, respectively, approximately 30 min prior to measurement, during which time they were maintained under low light conditions. For culture measurements and environmental measurements using samples from summer 2018, pressure increments of 5.17 kPa at 3 s intervals, and integration times of 1000 ms were utilized. For environmental measurements using samples from summer 2016, pressure increments of 2.59 kPa at 7 s intervals, and integration times of 1000 ms were utilized.

4.3.4 Processing of pressure nephelometry spectra

Nephelometric turbidity values associated with each pressure increment were determined from Vis-IR spectra by trapezoidal integration of nephelometric counts as a function of wavelength over the nephelometric wavelengths (860±30 nm). The resulting nephelometric turbidity data for each pressure increment was then concatenated into an array to give the total collapse measurement for processing using a suite of LabView™ virtual instruments (VIs). The array was passed into a recursive loop to yield an indexed array based on the pressure increments used in the collapse measurement, and then processed using a peak detection algorithm based on fitting sequential groups of data points to a quadratic polynomial. The indexed value of the detected peaks/valleys is used to control the loop iteration, resulting in a list of outputs containing values for the location of all peaks and valleys as well as the amplitudes and the 2nd derivatives associated with the detected inflection points. Use of indexed values as opposed to pressure steps allows the suite of VIs to automatically adapt to experimental conditions using different pressure step sizes or number of steps. The parameters associated with each discrete peak detected in the total collapse profile were then passed into a second iterative loop and used as the initial "guess" parameters to generate Gaussian curves of the form:

$$y[i] = a * e^{\left(-\frac{(x[i]-\mu)^2}{2\sigma^2}\right)}$$

based on multiple regression analysis using the Levenberg-Marquardt algorithm and the iterative general Linear Squares method, where α is the peak amplitude, μ is the peak center indicative of the CCP, σ is the standard deviation of the fitted model, and χ is the integrated nephelometric turbidity value at each pressure step, i. The Gaussian curves were then used to assign CPD values for each peak, where CPD=$\chi[i_{max}]$ - $\chi[i_{min}]$, as well as PST values, as determined by

numeric integration of turbidity as a function of pressure with respect to pressure (over the CPD ranges associated with each peak), according to the trapezoidal rule.

4.3.5 Assignment of pressure fractions

Replicate collapse measurements using environmental samples were collected on three separate days and CCP values were assigned as being distinct and included in analysis if: (i) they appeared in at least four of the six replicate measurements, and (ii) if the mean CPD was greater than three times the mean error about the CCP. Using these criteria, the total pressure range examined was divided into eleven pressure fractions such that the upper bound of each pressure fraction attempted to maximize the absolute pressure difference between the two peaks most immediately adjacent, as determined from the pressure nephelometry measurements.

4.3.6 Collection of pressure fractions

Utilizing the same environmental sample as in the pressure nephelometry measurements, 15 mL of sample was concentrated via gentle vacuum filtration (<30 kPa) onto a combusted GF/F filter, followed by multiple (3x, ~15 mL) resuspension and filtration steps using Milli-Q, in order to disrupt the extracellular polymeric substance (EPS) matrix and disperse consortia to the extent possible. The filtered cells were then resuspended, partitioned into twelve equivalent subsamples, diluted to a final volume of 10 mL per subsample, and allowed to equilibrate for <30 min. Following equilibration—with the exception of the first pressure fraction (0-93 kPa)—the top 7 mL of each subsample was first introduced into a 10x200 mm pressure-rated sample cell (8649-30; Ace Glass Inc, Vineland, NJ, USA), subjected to a pressure corresponding to the upper limit of the preceding pressure fraction, and held at that pressure for 10 min. Following the initial pressurization, the headspace was vented and the top 3 mL of sample was transferred via

pipette to a second collection pressure cell containing a syphon needle. The sealed syphon needle system consisted of a 0.5 mm ID glass capillary tube mated to ETFE HPLC tubing terminated in a normally-closed (NC) controllable valve allowing for sample collection; the tip of the syphon needle was located within 1 mm of the bottom of the pressure cell. The collection pressure cell was then ramped to the upper pressure limit associated with the fraction being analyzed and held at that pressure for 10 min. Following the second pressurization, pressure in the headspace was lowered to approximately 10^2 kPa, and the bottom 2 mL of sample was collected via the syphon needle system before fully venting the headspace. The syphon needle was then removed, the NC valve was opened to the atmosphere, and the samples were transferred into sterile Falcon tubes after rinsing the exterior of the syphon needle. Prior to collecting the subsequent sample, the syphon needle system was repeatedly back-flushed, using vacuum to minimize cellular contaminants in the collection system, starting with Milli-Q (~100 mL), followed by a soak in 70% ethanol (v/v) prior to a final Milli-Q rinse. For all fractions, prior to introduction of the sample and pressurization of the sample cell, the syphon needle was purged of air and back-filled with Milli-Q.

4.3.7 Permanent slide preparation

The pressure fractionated samples were preserved using 10 % (v/v) glutaraldehyde in BG11 at a final concentration of 1.0% and stored at 4°C overnight. Following preservation, 2-Hydroxypropyl methacrylate (HPMA) permanent slides for each pressure fraction and an unpressurized sample were prepared, as in Crumpton (1987), for microscope analysis. This method offers a number of benefits over traditional inverted microscope techniques based on the fact that gas-vacuolate organisms do not tend to undergo sedimentations—GVs are known to maintain their structure and function subsequent to preservation with Lugol's iodine and

glutaraldehyde—including the preservation of cell fine-structure and greatly decreased rates of photo-bleaching (Sundararajan & Ju, 2000; Nollet & De Gelder, 2013).

4.3.8 Microscopy and species identification

For all microscope counts and image acquisitions an AxioVert 200m microscope equipped with an Apotome imaging system was used (Carl Zeiss Microscopy; Thornwood, NY, USA). Counts were performed with minor alterations to the Utermöhl method as described by Lund et al., (1958), with the HPMA permanent slides replacing the settling column traditionally used. Phase contrast microscopy was used to identify uncollapsed GVs in cells of the unpressurized sample, which appear as refractile bodies. Briefly, HPMA slides corresponding to each pressure fraction were examined at both 400x and 1000x total magnification, and for each magnification a minimum of 400 gas vacuolate cells—corresponding to the morphotypes identified in the unpressurized sample—were counted, or 40 fields of view were examined, depending on which occurred first. Differential interference contrast (DIC) micrographs, allowing for analysis of cell structural characteristics, and confocal laser scanning micrographs (CLSMs), associated with phycobiliprotein and chlorophyll autofluorescence, were obtained for all pressure fractions. For CLSMs, a reflector module with a 546/12 nm excitation filter, FT 560 nm beam splitter, and 576-640 nm band pass filter were used.

4.4 Results & disscussion

4.4.1 Gas vacuolate species

Gas-vacuolate cyanobacteria within the unpressurized environmental sample were first identified under the light microscope using phase contrast illumination by the presence of refractile bodies indicative of gas vacuoles (Figure 4.2). Genus and/or species assignments for

the visibly distinct cyanobacteria were made based on morphological characteristics and similarity to reference strains given in Bergey's manual (2nd Ed, 2001), and/or molecular phylotyping studies (Tables 4.1 & 4.2). Micrographs of each species were recorded using the slide associated with the pressure fraction in which they appeared most abundantly based on counts (Table 4.1; Figure 4.3). Gas vacuoles were clearly present in the ten morphologically distinct cyanobacteria species for which counts were obtained, with the mean vacuole size across all species ranging from approx. 0.5-1.3 μm; the largest vacuoles occurred in *Microcystis* sp and *Nostochopsis* sp. The relative vacuolization within chains of the filamentous species, as well as within *Stanieria* sp. and *Xenococcus* sp., presumably due to localization within the baeocytes, was found to be highly variable, which may account for the broader pressure distribution observed in these species (Table 4.1).

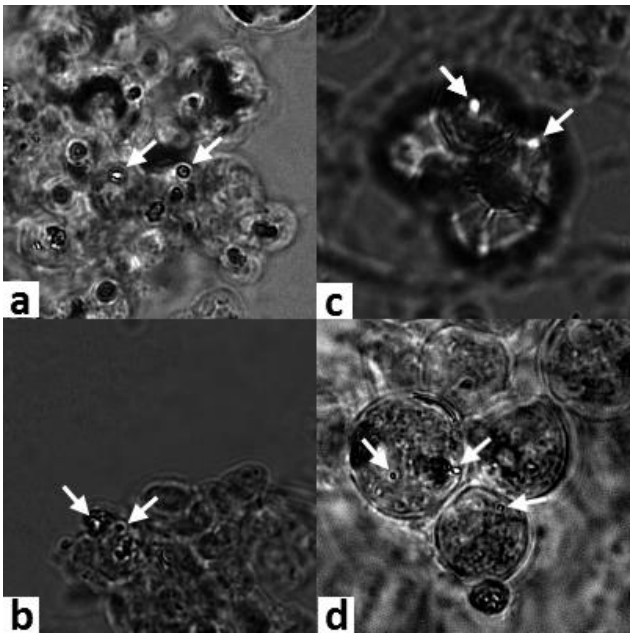

Figure 4.2: Phase contrast micrographs displaying intact GVs (arrows) in: (a) Microcystis aeruginosa; (b) Microcystis wesenbergii; (c) Aphanocapsa sp.; (d) Xenococcus sp. present in the uncollapsed environmental sample; all panes 32x32 μm.

Table 4.1: Percent relative abundance of morphotypically distinct, gas-vacuolate species associated with different pressure fractions. All species identified in fractions 1-3 had intact GVs and were present as colonial aggregates dominated by (presumably) non-gas vacuolate species. Highlighted cells indicate pressure range most likely characteristic of taxa indicated.

Taxon	**Pressure fraction (% abundance)**										
	F1	**F2**	**F3**	**F4**	**F5**	**F6**	**F7**	**F8**	**F9**	**F10**	**F11**
Stanieria sp.	36.9	19.0	0.6	16.1	0.2						
Aphanocapsa sp.						12.3	20.3	66.0	5.8	3.6	1.1
Xenococcus sp.	23.9	13.1			39.5	15.0					
M. Aeruginosa	35.1		74.2	8.3		60.3			4.2		
M. Wesenbergii									81.8	36.0	0.1
M. Viridis	4.1				20.6	12.4					
Dolichospermum sp.		67.9	25.2	67.9	39.7			3.9			
Pseudanabaena sp.							79.7	30.1	0.3	0.3	0.2
Nostoc sp.				7.6							
Nostochopsis sp.									7.9	60.1	98.6

Table 4.2: Dominant gas vacuolate morphotype associated with experimental pressure fractions identified by microscopic counts.

	Morphology	**Cell size (μm)**	**Range (kPa)**	**Species or genera**
F1	Round cells w/thick external wall (~1 um), multiple baeocytes per cell (1.5-3 um diameter), multiple fission	17.8±1.25 (diameter)	0-93	*Stanieria* sp
F2	Barrel shaped cells, non-branching chain w/non-terminal akinets and heterocycts, mucilage but no sheath, binary fission in one plane	2.6±0.19 (length) 1.5±0.20 (width)	93-155	*Anabaena (Dolichospermum)* sp.
F3	Round to oval cells in densely packed mucilaginous colony, elongation with binary fission	4.4±0.39 (length) 4.1±0.26 (width)	155-231	*Microcystis aeruginosa*

	Morphology	Cell size (μm)	Range (kPa)	Species or genera
F4/ F5	Barrel shaped cells in non-branching chain w/non-terminal akinets and heterocycts, mucilage but no sheath, binary fission in one plane	2.4±0.32 (length) 1.4±0.08 (width)	231-259/ 259-310	*Anabaena (Dolichospermum)* sp.
F6	Round to oval cells in densely packed mucilaginous colony, elongation with binary fission	4.4±0.40 (length) 4.2±0.34 (width)	310-455	*Microcystis aeruginosa*
F7	Isodiameteric cells in straight chains, no akinetes or heterocysts, terminal cells undifferentiated, growth from tip w/ short trichomes (<10 cells)	1.8±0.41 (length) 1.8±0.07 (width)	455-507	*Pesudanabaena* sp
F8	Diplococci/tetrads w/slime capsule linking cells within larger clusters, successive division in two planes at right angles	3.9±0.38 (length) 3.2±0.31 (width)	507-610	*Aphanocapsa* sp
F9	Round to oval cells in diffuse mucilaginous colonies, elongation with binary fission	4.2±0.41 (length) 3.1±0.34 (width)	610-683	*Microcystis wesenbergii*
F10/ F11	Irregular T-branching filaments, intercalary uniseriate/lateral-sessile heterocysts. Majority GV content intact in Fx10	3.6±0.61 (chain width)	683-817/ 817-1034	*Nostochopsis* sp

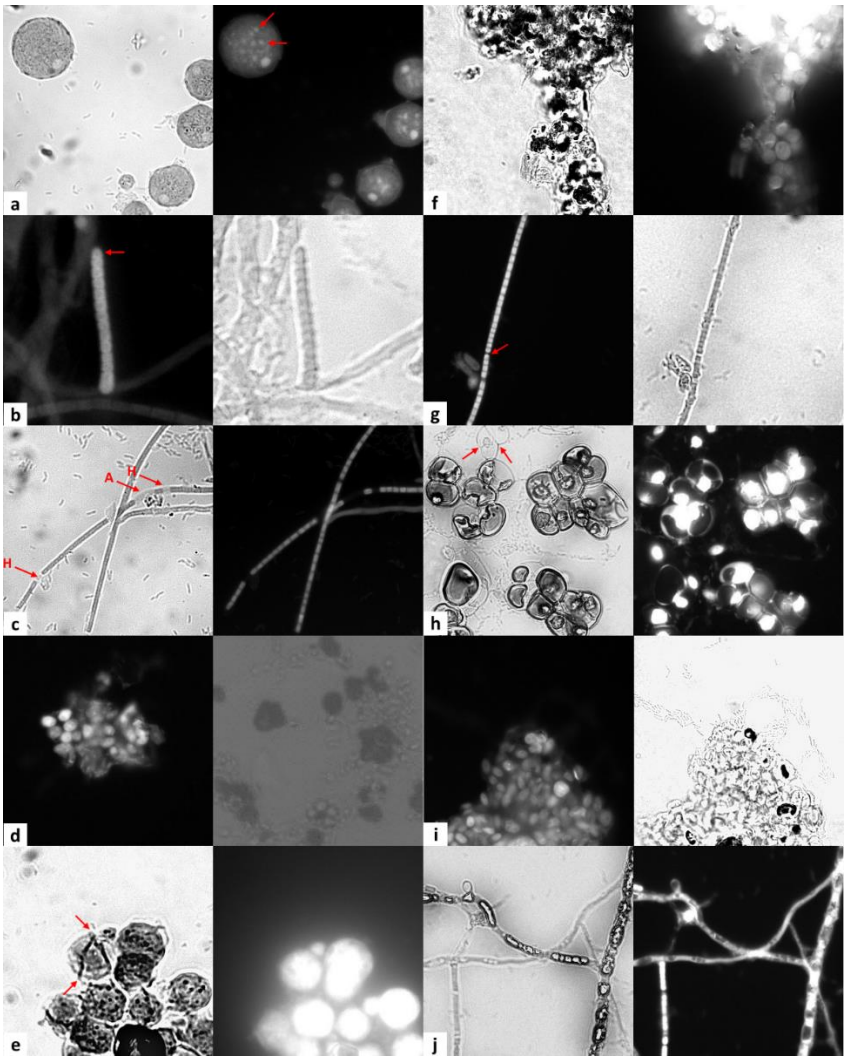

Figure 4.3: Representative morphotypically distinct species in pressure fractionated samples (Table 3): (a) Stanieria sp., (arrow) presence of multiple baeocytes; (b) Nostoc sp., (arrow) conical end cell typical of hormogonia; (c) Anabaena (Dolichospermum) sp., (H) intercalary heterocysts and (A) akinetes; (d) Microcystis viridis displaying diffuse mucilage; (e) Xenococcus sp., vegetative cells smaller than Stanieria sp., (arrow) visible cleavage stages 90° opposed; (f) Microcystis aeruginosa; (g) Pseudanabaena sp., (arrow) round, undifferentiated terminal cells; (h) Aphanocapsa sp. characterized by distinct slime capsule (arrow) and successive division in two planes at right angles; (i) Microcystis wesenbergii smaller and more ovoid, more diffuse within the mucilage than M. aeruginosa; (j) Nostochopsis sp. All panes 64 x 64 μm.

4.4.2 Pressure nephelometry of cultures

Collapse profiles from mixed cultured strains of *Merismopedia* sp, *Anabaena* (now *Dolichospermum*) sp, and *Microcystis* sp, resulted in CCPs for *Anabaena* sp. and *Microcystis* sp. of 248 and 476 kPa, respectively; closely approximating literature reports of the mean CCP as measured in axenic cultures of the reference strains *Anabaena flos-aquae* CCAP1403/13f and *Microcystis aeruginosa* BC84/1, of 180 ±100 kPa and 440±120 kPa, respectively (Figure 4.4; Table 4.3) (Walsby & Bleything, 1988; Dunton & Walsby, 2005). With the CPD range for the *Anabaena* sp and *Microcystis* sp we examined of 207-347 kPa and 352-662 kPa, respectively, falling well within the ranges reported for monocultures of *Anabaena flos-aquae* CCAP1403/13f and *Microcystis aeruginosa* BC84/1, of 0-370 kPa and 280-680 kPa, respectively (Hayes & Walsby, 1986). The more constrained CPD range for the *Microcystis* sp is well aligned with our previous examinations using axenic cultures of *Microcystis aeruginosa* PCC7806, where the CPD was found to be 252 ±21 kPa, occurring over the range 368-620 kPa and centered about the CCP of 494 ±3 kPa (S.W. Dyer, and J.A. Needoba, in review).

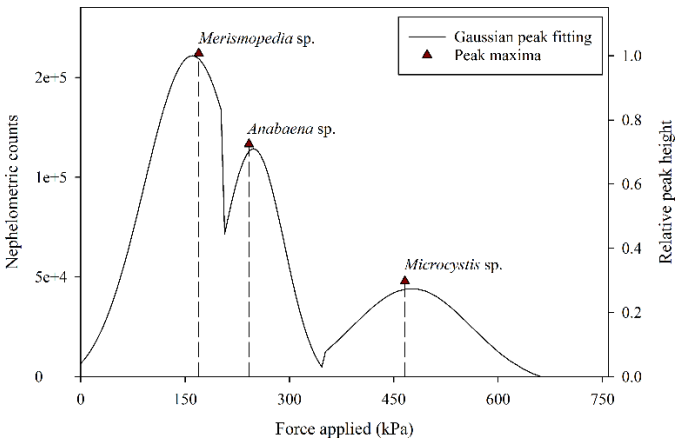

Figure 4.4: Gaussian peak fitting of collapse profile (solid line), and peak maxima from raw nephelometric signal (triangles) resulting from mixed cultured strains of Merismopedia sp., Anabaena (Dolichospermum) sp., and Microcystis sp.

Table 4.3: Characteristic CCP of GVs (Pc) in the absence of turgor pressure (Pt) in aquatic organisms; in vivo CCP given by the difference between Pc and Pt. Values obtained from manual pressure nephelometry measurements are noted to vary by $>10^2$ kPa; more recent measurements utilizing automated systems are much better constrained (Holland & Walsby, 2009; S.W Dyer & J.A. Needoba, in review).

Organism		Pc (kPa)	Pt (kPa)	Reference
Cyanobacteria	*Anabaena* CCAP 1403/13f	610±100	430	Walsby, 1980
	Aphanizomenon CCAP 1401/1	600±80	350	Walsby & Bleything, 1988
	Dactylococcopsis BC 79/1	330±110	80	Walsby & Bleything, 1988
	Microcystis aeruginosa BC 84/1	770±120	320	Walsby et al., 1983
	Microcystis aeruginosa PCC 7806	806±3	307±3	Dyer S.W. & J.A. Needoba, in review
	Nostoc muscorum PCC 6719	570±80	360	Walsby & Bleything, 1988
	Oscillatoria agardhii PCC 7801	990±130	380	Walsby & Bleything, 1988
	Prochlorothrix hollandica	890	460	Walsby, 1994
other bacteria	*Amoebobacter roseus*	340	150	Walsby, 1971
	Amoebobacter purpureus	240	100	Walsby, 1994
Halobacteria	*Halobacterium salinarium*	90	0	Walsby, 1971

4.4.3 Sinking velocity based on CPD

From the environmental sample pressure nephelometry collapse profiles, the upper bound for the mean CPD of all peaks corresponded to a time period of 161 ±49 s (Figures 4.5 & 4.6). As the nephelometric interrogation region arising from the plano-convex collimating lens is ≤5 mm, based on literature reports for the positive sinking velocity (v_s) of gas-vacuolate cyanobacteria similar to those we identified via microscopic enumeration, the inferred sinking

velocity based on the mean CPD of peaks in the environmental samples (v_s=31 ±7 μm s^{-1}), falls within the range of reported rates for taxa from temperate freshwater systems of 10-120 μm s^{-1} (Reynolds et al., 1987; Sullivan et al., 2011). The mean sinking velocity, based on CPD ranges obtained from pressure nephelometry measurements using mixed cultured strains (v_s=44 ±17 μm s^{-1}), was also similar to the mean rate from our environmental measurements.

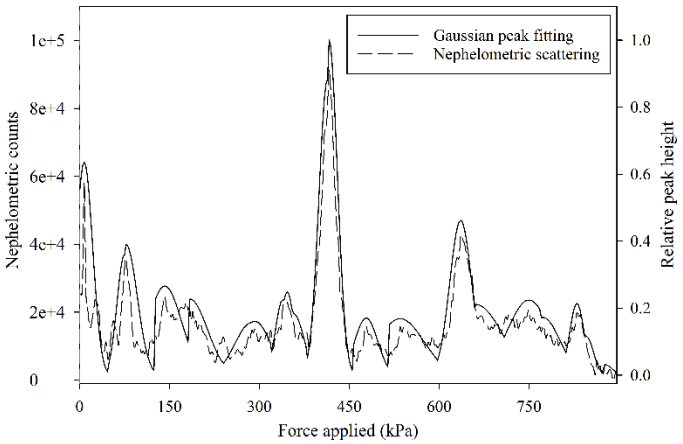

Figure 4.5: Pressure nephelometry spectrum and Gaussian peak fitting of distinct pressure sensitive fractions in environmental sample utilized for experiments.

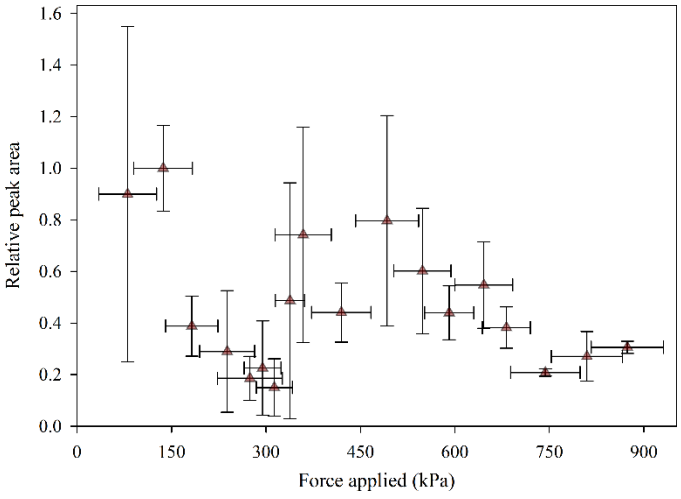

Figure 4.6: (Triangles) mean CCP from replicate (n=6) pressure nephelometry measurements using environmental samples; (dashed lines) pressure fraction cutoffs; (vertical error bars) relative error about the mean PST, which represents variation in signal magnitude and is correlated with relative abundance; (horizontal error bars) mean CPD.

4.4.4 Pressure fractionation of cyanobacteria in environmental samples

We assigned nephelometric peaks to the different cyanobacterial taxa based on a combination of direct visual examination and by comparison to literature values. Based on the combination of pressure nephelometry measurements and microscope counts utilizing the pressure fractionated samples, we found the CCP/CPD of species—occurring not as a consortia within the pressure fractionated samples—for which literary comparisons were available to be well aligned (Tables 4.1 & 4.3; Figure 4.3). *Anabaena* sp. dominated the assemblage over the pressure range 231-310 kPa, with the greatest abundance of *Anabaena* sp. identified within the 231-259 kPa pressure fractionated sample (67.9% relative abundance) (Table 4.1). For the 231-259 kPa fraction only one peak was detected (Figure 4.3), with a CCP of 238 ±7 kPa, which closely approximates reported values for axenic *Anabaena* sp cultures and measurements from our cultures (Tables 4.1 & 4.2; Figure 4.6). Within the 310-455 kPa pressure range *M. aeruginosa* was found to be the dominant species based on counts (60.3% relative abundance), while *M. viridis* was also detected in this fraction (12.4%); however, the latter was better represented within the 259-310 kPa pressure fraction (20.6%), leading to CCP assignments of 313 ±2 kPa and 420 ±8 kPa for *M. viridis* and *M. aeruginosa*, respectively.

Aphanocapsa sp, belonging to the subclass Oscillatoriophycideae, possesses a high degree of GV homology to *Oscillatoria* sp. (JSC-12), with a protein blast query of GvpA from an *Aphanocapsa* reference genome (BDHKU210001) to that of *Oscillatoria* sp (JSC-12) resulting in a blast hit identity value of 98.6% (71/72 residues) and 100% sequence identity. Literature reports using axenic cultures of *Oscillatoria agardhii* PCC 7801 report a CPD ranging from 320-980 kPa, with the mean CCP of 610 ±130 kPa closely matching the experimental pressure fraction (507-610 kPa) in which *Aphanocapsa* sp was found to be the most abundant (66.0%

relative abundance), resulting in a CCP assignment of 548 ±5 kPa based on the pressure nephelometry measurements. The nearest neighbor based on phylogenetic alignment of 29 concatenated PhyEco marker genes to *Stanieria* sp is *Xenococcus* (bootstrap=1), supporting the similarity in observed CCP; no literary CCP values could be found for either strain (Wilbanks et al., 2017). However, based on our experimental results *Stanieria* sp and *Xenococcus* sp occurred most frequently within and below, and within and above the 231-310 kPa range, respectively. From this, tentative CCP assignments of 275 ±6 kPa and 295 ±5 kPa for *Stanieria* sp. and *Xenococcus* sp., respectively, are proposed based on the pressure nephelometry measurements, and the associated overlap of CPD ranges with the results of the microscope counts (Table 4.1; Figure 4.6). CCP assignments of 492 ±14 kPa, and 646 ±7 kPa for *Pseudanabaena* sp, and *M. wesenbergii*, respectively, are likewise proposed, with each species dominating the pressure fraction associated with their assigned CCP (≅80% relative abundance). The peaks for which species assignments are not presented are likely the result of cellular consortia possessing GVs with disparate CCPs and/or a lack of GVs, excessive CPD overlap of multiple species resulting in inefficient pressure fractionation, and/or a need for further refinement of the peak detection and fitting algorithms. It is also possible that our microscopic identification failed to separate/delineate morphologically similar cells, or failed to detect additional gas vacuolate species present in the samples.

4.5 Summary

The combined results of the pressure nephelometry experiments and microscopic examination of pressure fractionated samples support the interpretation that the Gaussian-distributed peaks observed in the pressure nephelometry spectra are a result of GV collapse in a predictable fashion in successive fractions of buoyant cells, where the loss of buoyancy and

associated CCP generate a stable signal that can be used for species delineation. Comparison of the collapse profiles of environmental samples collected from the same site in the summers of 2016 and 2018 further supports this interpretation (Figures 4.5 & 4.7), where the CCP of peaks appearing across years are very strongly correlated ($r=0.999$, $p<10^{-9}$, $n=8$), and coincide with the dominant species from the pressure fractionation experiments.

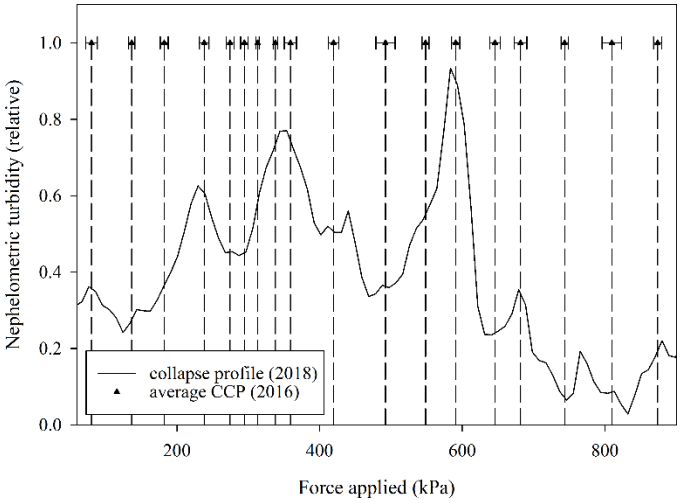

Figure 4.7: Pressure nephelometry comparison of samples collected in May, 2018 to the mean CCP of peaks from the samples collected in June, 2016; error bars represent the standard deviation about the mean CCP (n=6).

Despite the improved specificity afforded by molecular techniques, as compared to microscopic identification, due to the elevated costs and protracted times required for sample analysis and interpretation, they do not lend themselves to routine monitoring applications (Te et al., 2015; Otten et al., 2016). The setup time per pressure nephelometry collapse measurement is generally less than a minute, and the measurement itself—as presented for the culture and environmental assays described—ranges from 10-45 min, with immediately available results. The complete pressure nephelometry system we developed uses commercially available parts,

and costs less than a basic benchtop fluorometer—with gas from a pressurized source being the only consumable.

As GVs are crucial for the dominance of bloom forming cyanobacteria within HABs, where the relative GV content increases in tandem with ecophysiological factors linked to cyanotoxin production potential, and as PST can be used as a more robust surrogate for cyanobacterial abundance than chlorophyll fluorescence, pressure nephelometry is a promising tool for monitoring efforts in aquatic ecosystems and the mitigation of cyanobacteria-associated human health threats.

The accurate detection of different cyanobacteria species is important for predicting toxicity within cyanoHABs. For example, *M. aeruginosa* and *M. viridis* have been shown to be the dominant microcystin (*Mcy*) producing *Microcystis* species, while *M. wesenbergii* is not believed to produce *Mcy*, with our results indicating that separation of these species is possible based on their divergent CCP and the minimal CPD overlap we observed in the pressure fractionated samples (Kaneko et al., 2007; Meyer et al., 2017). In addition, as CCP is the effective critical collapse pressure of GVs in turgid cells, temporal shifts in cellular metabolism associated with stress responses manifest in the pressure nephelometry measurement as alterations to the characteristic CCPs, allowing for rapid estimates of toxin production potential in routine monitoring applications (Chapter 5). Moreover, as pathogenic enterobacteria, antibiotic producing actinomycetes, and arsenic methylating halobacteria are known to produce GVs, pressure nephelometry may also be applicable for the routine monitoring of drinking water supplies and/or effluent from wastewater treatment plants. There is an urgent need for methods that are accurate, rapid, and scalable for widespread monitoring efforts surrounding our aquatic resources, and pressure nephelometry is a promising prospect.

4.6 Comments and recommendations

Further molecular and genomic assays are needed to clarify the species assignments, as morphological similarities make microscopic species delineation difficult. Molecular and genomic characterization of the gas vacuolate populations within the pressure fractions would also advance the feasibility of using pressure nephelometry for routine monitoring purposes in a variety of applications, especially as it relates to toxin production potential and human health impacts from GV-containing organisms.

Refinements to the peak fitting algorithm could provide accurate quantitative estimates of cellular subsets within mixed assemblages, as variable nephelometric scattering results from cells of various size and morphology (i.e. chain vs round). The settling velocity of cells also varies with particle size and the concentration of dense cellular constituents, such that closely associated peaks with narrow CPD ranges and a large degree of CPD overlap may be attributable to a single species, as the settling velocities inferred from these narrow CPD ranges boarder on the upper limit of expected values for freshwater cyanobacteria. Therefore, the pressure fractionation and the accuracy of measured CCP/CPD values would benefit from increases in the time between pressure steps and/or decreases in the size of pressure steps. Owing to the programmatic nature of the pressure nephelometer and the accuracy of the pressure transducer, these changes would be easy to adopt. Additionally, a horizontal slit prior to the plano-convex collimating lens associated with the nephelometric detector could be used, which would presumably result in finer resolution between populations by limiting the overlap of peak tails, and if settling is pressure-induced and PST follows a Gaussian distribution, should not affect the interpretation of collapse measurements, the assignment of CCPs, or the estimation of settling velocities.

5. The cyanobacterial neurotoxin β-*N*-methylamino-L-alanine (BMAA) attenuates gas vesicle critical collapse pressure and enhances colony formation to control buoyancy and bloom succession in stratified water column conditions[4]

5.1 Abstract

Under dense cyanobacterial Harmful Algal Bloom (cyanoHAB) states, proteinaceous gas vesicles (GVs) allow cyanobacteria to colonize air-water interfaces, which increases access to carbon species and photosynthetically active radiation. However, the warm periods that accompany the formation of cyanoHABs often result in decreased nutrient access due to thermal stratification of the water column, leading to enhanced oxidative stress and UV-radiation (UVR) exposure in the buoyant population. Here, we present evidence from laboratory culture studies using *Microcystis aeruginosa* PCC7806, and environmental time series measurements from a seasonally recurrent freshwater cyanoHAB dominated by *Microcystis* sp. that the cyanobacterial neurotoxin β-*N*-methylamino-L-alanine (BMAA) is involved in the regulation of bloom dynamics. We demonstrate decreased GV critical collapse pressure (CCP) in cyanobacteria and increased colony formation due to BMAA in both settings, and correlate these adaptations with enhanced nutrient scavenging efficiency and the mitigation of oxidative stressors resulting from diel vertical migration (DVM) cycles. Further, we propose that the decrease in CCP due to BMAA culminates in bloom collapse when the hydrostatic pressure experienced during DVMs exceeds the CCP of the buoyant population. As BMAA is a potential etiological agent of human neurodegenerative disease and continued global warming will enhance thermal stratification in freshwater systems, here proposed to result in increased BMAA production, this is of great concern. This work presents an ecophysiological function for BMAA, proposes a mechanism for

[4] Dyer, S.W., T.D. Peterson, & J.A. Needoba. Journal TBD; expected submission, 2019.

CCP modulation in buoyant freshwater cyanobacteria, and identifies a need for further investigation of the regulatory systems responsive to BMAA in gas vacuolate organisms, including human enterobacteria.

5.2 Introduction

Freshwater systems subjected to anthropogenic eutrophication and warmer temperatures are at increased risk for the formation of Harmful Algal Blooms (HABs), where the species richness and diversity decrease throughout the warm summer months, often resulting in a cyanobacteria HAB (cyanoHAB) state (Gomez-Casati et al., 2003; Woodger et al., 2005; Van de Waal et al., 2011). During cyanoHAB events, the high rates of photosynthesis and concurrent uptake of dissolved inorganic carbon create daily pH fluctuations in the surrounding water; a condition that has been demonstrated to stimulate the synthesis of intracellular gas vesicles (GVs) in cyanobacteria (Gao et al., 2016), thus creating hyper-buoyant cells that float near the air-water interface (Paerl & Ustach, 1982; Dervaux et al., 2015). The upward trend in global average temperatures over the last century is likely to continue, and benefits buoyant cyanobacteria in a number of ways, as decreased water density and dissolved gas concentration both occur with increases in aquatic temperature (Johnk et al., 2008; Paerl & Huisman, 2008). Hydrodynamic drag decreases with decreased water density, and the buoyant force provided by GVs increases with decreased dissolved gas concentration—generating conditions such that the rate of GV-associated taxis outstrips migration in motile microbes by multiple orders of magnitude (Walsby, 1994). Optimal growth rates in cyanobacteria also occur at elevated temperatures as compared to other aquatic phototrophs (Elliott et al., 2006; Tang et al., 2018).

Localized bloom formation at air-water interfaces by gas vacuolate cyanobacteria may be a key aspect of species succession within cyanoHABs, as it reduces grazing pressure on the

buoyant cyanobacteria population, while the resultant shading of the water column and drawdown of dissolved gas species stifles growth in non-buoyant phytoplankton and aquatic plants (Sterner, 1989; Dervaux et al., 2015). However, prolonged residence times near surface boundary layers create deficits in the nutrients required for balanced growth and expose cells to high levels of UVR—factors strongly associated with the induction of stress response mechanisms in cyanobacteria (Kaebernick et al., 2000; Downing et al., 2011; Zilliges et al., 2011).

Previous reports have demonstrated that pressure nephelometry can be used for the in vivo analysis of GV physiomechanical properties and cellular metabolic status (Walsby, 1980; S.W Dyer & J.A. Needoba, in review). As the critical collapse pressure (CCP) of GVs is linked to cell turgor, and is therefore a function of the chemical, osmotic, and water stress components of the cell, pressure nephelometry allows for inferences to be made regarding the metabolic status and nutrient history of gas vacuolate organisms via determination of CCP—a metric that is stable and species specific under balanced growth (Walsby, 1980; S.W. Dyer & J.A. Needoba, in review; S.W. Dyer, L.P Cook, T.D. Peterson, & J.A. Needoba, in review). The results of the pressure nephelometry measurement in mixed gas vacuolate assemblages can therefore be used to gauge changes in population dynamics and identify shifts in the metabolism of distinct subsets of cells.

The atypical amino acid β-*N*-methylamino-L-alanine (BMAA) diverges from other cyanotoxins in that it lacks acute toxicity, and as such, has received comparatively less attention from scientists and regulatory agencies (Holland & Kinnear, 2013). However, BMAA has been putatively identified as an etiological agent of at least one human neurodegenerative disease with defining characteristics that resemble a combination of traits specific to Alzheimer's Disease

(AD), and Amyotrophic Lateral Sclerosis/Parkinsonism Dementia Complex (ALS/PDC), which are not typically observed in tandem (Cox et al 2003; Murch et al, 2004; Spencer et al., 2005; Xiao et al., 2006; Liu et al., 2009; Koenig et al., 2015; Cox et al., 2016; Metcalf et al., 2017; Scott & Downing, 2018). Moreover, BMAA is the only cyanotoxin known to occur in all five cyanobacteria "Orders," indicating the compound may play a fundamental role within the canonical cyanobacterial metabolon (Cox et al., 2005). Isotopic labeling studies have demonstrated the de novo production and the rapid uptake (within 10 min) of exogenous BMAA, and proposed that the compound is associated with nutrient stress responses; conclusive evidence of a distinct biochemical or ecophysiological role for the compound has not been presented (Downing et al., 2011; Downing et al., 2012).

This work seeks to address knowledge gaps associated with the ecophysiological role of BMAA in cyanobacteria, with a focus on GV regulation. First, using both culture and field measurements of *Microcystis* sp., we demonstrate that BMAA decreases the CCP of GVs and enhances colony formation. The BMAA-associated decrease in CCP is here proposed to: (i) enhance nutrient scavenging efficiency by accelerating the transition between positive-and-negative buoyancy during DVMs in stratified water column conditions, and (ii) to occur in response to the photooxidative and nutrient stressors associated with surface scum formation. Further, using the environmental time series measurements, we present evidence that decreased CCP among the buoyant cyanobacterial population is correlated with increased BMAA concentration and may attribute to bloom senescence. Finally, a proposed mechanism for the GV-associated changes induced by BMAA is presented.

5.3 Materials and methods

5.3.1 Automated pressure nephelometer

A detailed description of the high resolution pressure nephelometer and the use of pressure nephelometry for species identification in natural settings are given elsewhere (S.W. Dyer & J.A. Needoba, in review; S.W. Dyer, L.P Cook, T.D. Peterson, & J.A. Needoba, in review). Briefly, the use of a high power IR LED, an automated pressure regulator, and individual wavelength-resolved spectrophotometry allow for quantitative turbidity measurements that describe discrete species-specific gas vesicle CCPs that can inform both the abundance and relative buoyancy capacity of species during HAB events.

5.3.2 BMAA culture addition experiments

Cultures of the aquatic freshwater cyanobacteria *Microcystis aeruginosa* PCC7806 were obtained from the Pasteur Culture Collection of Cyanobacteria (Paris, FR). For all culture maintenance and measurement BG11 medium was used, and sterile culture techniques were observed for all manipulations (Allen and Stanier, 1968). Cultures were maintained on a 14/10 hr light/dark cycle at 15°C under a photosynthetic photon flux density of 30 μmol s^{-1} m^{-2} on a shaker table oscillating at 40 rpm. As the ratio of red/teal light is known to effect colony formation and induce complementary chromatic adaptation, all cultures were maintained under pulse-width modulated LED lighting (Cree CXB2540, Durham, NC, USA), which more closely approximates the natural visible spectrum than fluorescent lighting (Enomoto et al., 2015). On the day prior to culture spike, dense replicate cultures (n=6) in mid-exponential growth were diluted at a ratio of approximately 1:18 to a uniform optical density and a final volume of 0.75 L. For culture spikes, a solution of L-BMAA hydrochloride, (BMAA; CAS #:16012-55-8), purity ≥97% (NMR) purchased from Millipore-Sigma (St. Louis, MO, USA), was prepared at a concentration of 25 mM in MilliQ and spiked into replicate cultures resulting in a final concentration of 10 μM.

In addition to pressure nephelometry measurements, in vivo measurements of chlorophyll-a, phycocyanin, phycoerythrin, and turbidity were conducted using a benchtop laboratory fluorometer (Trilogy; Turner Designs, San Jose, CA, USA). All in vivo photopigment measurements are reported as relative values normalized to the maximum RFU/NTU of the control cultures.

5.3.3 Environmental samples

Ross Island lagoon, located near Portland, Oregon, USA in the Willamette River, Oregon, USA, was formed in 1926-27 when an earthen dike was constructed between Hardtack and Ross Islands. The lagoon is approximately 200 acers, with access to the lagoon occurring via a 500-foot-wide mouth that is connected to the Willamette River through a slow moving slough on the east side of the island. For more than eighty years, the lagoon was used as a mining and processing site for sand and gravel, resulting in a maximal depth of approximately 30 m; the main channel of the Willamette River adjacent to the lagoon in approximately 14 m deep. Due to the regional geology, characterized by unconsolidated river alluvium (maximum depth of approximately 200 m) overlaying partially-cemented sandstone formations, the lagoon receives groundwater flux from a North-northwest-oriented hydraulic gradient with an average magnitude of 0.0002 (ODEQ, 2011).

Whole water environmental samples (Figure 5.1), for each sampling date were collected at approximately noon at a sampling site within the lagoon. Whole water samples were collected in triplicate, 1 L opaque polycarbonate bottles that had been cleaned using 10% HCl, and triple rinsed with deionized water. All samples were collected at midday, along with high resolution depth profiles of water temperature and conductivity using a handheld CTD equipped with a 6-electrode conductivity cell and fast response thermistor (SonTek, San Diego, CA, USA).

Samples were immediately stored on ice, and transported to the laboratory for same day analysis in accord with EPA recommendations (EPA, 1984a).

Chlorophyll a was collected by gently vacuum filtration (100-300 mL) onto Whatman GF/F filters, which were transferred to cryovials, and stored at -80°C until analysis. The filter concentrated samples were extracted into acetone, and chlorophyll-α concentrations were determined via EPA method 445.0: *in vitro* determination by fluorescence—utilizing a benchtop laboratory fluorometer (Trilogy; Turner Designs, San Jose, CA, USA).

For pressure nephelometry measurements, following gentle inversion, triplicate 10 mL aliquots were removed via sterile serological pipette and transferred to sterile falcon tubes. The aliquots were then gently agitated via serological pipette and left open to the atmosphere under low light (15-30 μmol s^{-1} m^{-2}) for approx. 30 min, at which point the upper 4 mL of each aliquot was collected via pipette and transferred to the pressure nephelometer sample cell for measurement.

For toxin quantification, replicate whole water samples (n=9) were collected in sterile 15 mL falcon tubes, and strored in a -20°C freezer prior to lyophilization (Freezone4; Labconco Co., Kansas City, MO, USA), at which point the lyophilized material was transferred to siliconized centrifuge tubes, and the tubes were parafilmed and stored at -20°C until sample workup for BMAA. The HPLC-MS/MS detection of the dansyl derivative of BMAA (DNS-BMAA) was performed as previously described, with quantification based on the area ratio of multiple transitions specific to DNS-BMAA referenced to a ^{15}N-labeled BMAA stable isotope-labeled internal standard (S.W. Dyer, J.A. Needoba, & T.D. Peterson, in review).

Nutrient analysis was performed as previously described (Gilbert et al., 2013), using an Astoria Analyzer (Astoria-Pacific, Clackamas, OR, USA) for nitrate+nitrite (reported as nitrate),

silicic acid, orthophosphate (reported as phosphate), and fluorescent ammonium (EPA 1984b/c, Aminot et al., 2001).

Figure 5.1: (left) Ross Island Lagoon HAB in early August dominated by small, evenly dispersed colonies approx. 0.2 mm in diameter; (right) Ross Island Lagoon HAB in late August dominated by large colonies with a maximum diameter of approx. 20 mm.

5.3.4 Pressure nephelometry

Pressure nephelometry measurements were performed, and collapse spectra were generated as previously described (S.W. Dyer & J.A. Needoba, in review; S.W. Dyer, L.P Cook, T.D. Peterson, & J.A. Needoba, in review). All transfers were performed utilizing sterile culture techniques. For culture and environmental measurements, pressure increments of 5.17 kPa at 3 sec and 5 sec intervals, respectively, and integration times of 1000 ms were utilized.

5.3.5 Permanent slide preparation of cultures

On each sampling day, 10 mL aliquots of culture were preserved using 10 % (v/v) Glutaraldehyde in BG11 at a final concentration of 1.0% and stored at 4°C overnight. Following preservation, 2-Hydroxypropyl methacrylate (HPMA) permanent slides were prepared using 1 mL of the preserved sample, as in Crumpton (1987), for microscope analysis.

5.3.6 Microscopy and colony analysis

Micrographs were acquired on an AxioVert 200m microscope equipped with an Apotome imaging system (Carl Zeiss Microscopy; Thornwood, NY, USA). Differential interference contrast (DIC) micrographs, allowing for analysis of cell structural characteristics and cell diameter, and confocal laser scanning micrographs (CLSMs), associated with phycobiliprotein and chlorophyll autofluorescence—used for colony analysis and estimation of cytoplasmic volume, were obtained at 400x total magnification. For CLSMs, a reflector module with a 546/12 nm excitation filter, FT 560 nm beam splitter, and 576-640 nm band pass filter were used. For micrograph analysis the open-source software ImageJ was used. Briefly, for both DIC and CLSM, a background subtraction using a 50-pixel rolling ball was performed, and artifacts smaller than 2 pixels were removed as noise. Maps of object surfaces in pairs of DIC/CLSM micrographs were generated using the 3D Object Counter plugin (Cordelires & Jackson, 2005), which were then used as inputs for the Colocalization Finder plugin (Laummonerie, 2006), the results of which were used to generate and analyze skeleton plots of the colocalized pixels (i.e. colonies).

5.3.7 Statistical analysis & graphics

The results of replicate measurements are expressed as the mean ± the standard deviation (SD) about the mean for metrics derived from regression fittings, and as the mean ± the standard error (SE) in all other cases. For Student's *t*-tests and Pearson correlation coefficients, $p<0.05$ was used to gauge significance. For regression analysis and fitting of data, the coefficient of determination (R^2), and the standard error about the mean (S) are reported. Data processing of nephelometric spectra for the pressure nephelometry measurements was performed using a suite

of LabView virtual instruments, as previously described (S.W. Dyer & J.A. Needoba, in review; S.W. Dyer, L.P Cook, T.D. Peterson, & J.A. Needoba, in review). All other data analysis was performed in SigmaPlot 13.0. All graphics were compiled using Gnu Image Manipulation Platform (GIMP 2.8.14).

5.3.8 GvpA protein alignment and modeling

Protein primary sequences for GvpA from twenty-two freshwater cyanobacteria reference strains were obtained from the CyanoBase database (Fujisawa et al., 2017). Multiple sequence alignment of the GvpA orthologs were generated using the ClustalX2 and Jalview platforms (Larkin et al., (2007), and Waterhouse et al., (2009), respectively) based on the BLOSUM62 substitution matrix. Protein secondary structure predictions based on the consensus sequence of the multiple alignment, as well as the GvpA sequences for *Microcystis aeruginosa* PCC7806 and *Anabaena* sp. 90, were generated in I-TASSER and PSIPRED (Yang & Zhang (2015), and Jones (1999), respectively). The best-fit model of the GvpA consensus sequence was used for figure generation in PyMOL.

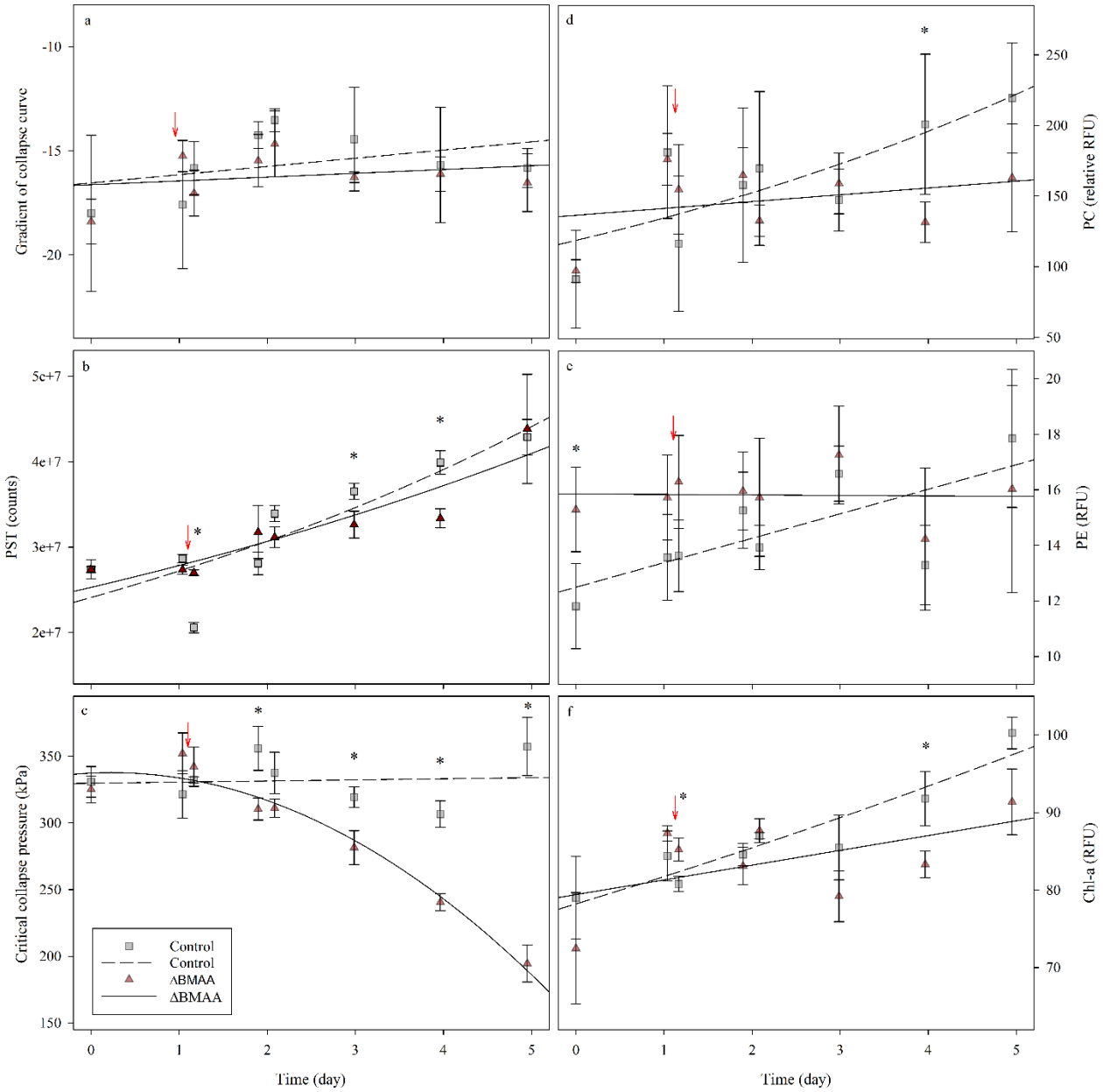

Figure 5.2: Effects of exogenous BMAA spike (arrow) on GV and photopigment fluorescence in M. aeruginosa PCC 7806; (a) gradient of sigmoid pressure collapse curves; (b) integrated pressure sensitive turbidity; (c) critical collapse pressure calculated from sigmoid collapse curves; (d) phycocyanin (PC) fluorescence; (e) phycoerythrin (PE) fluorescence; and (f) chlorophyll-a (Chl-a) fluorescence; (*) time points for which the difference between control and BMAA treated samples are statistically significant (t-test, $p<0.05$).

5.4 Results & discussion

5.4.1 Laboratory culture results

5.4.1a Gas vesicle response to BMAA treatment

Pressure nephelometry measurements of control and BMAA-spiked cultures demonstrated a variety of responses, as illustrated in Figure 5.2. Figure 5.2a depicts the rate of GV collapse, indicated by the turbidity-pressure change, which was not significantly different between the control and BMAA treated samples. Based on Student's *t*-tests, no statistically significant difference was observed for any of the sampling points.

Figure 5.2b shows that the temporal change in the integrated pressure sensitive turbidity (PST) signal—a proxy for total GV volume—was also similar ($R=0.954$, $p<0.001$). Statistically significant differences were not observed about the mean PST of the two groups ($t=0.130$, $p=0.90$), where as PST in the BMAA treated samples was found to be statistically lower than controls on days three and four ($t=2.987$ and $t=5.215$, respectively; $p<0.05$). However, the mean relative gas vesicle volume (based on comparison of the PST and Chl-α derived growth rates), for the BMAA treated samples ($\mu=0.096$ and $\mu=0.022$, respectively), was greater than that of the control ($\mu=0.121$ and $\mu=0.045$, respectively) (Figures 5.2b/5.2f).

Figure 5.2c demonstrates that the mean CCP in the control and the initial CCP in BMAA treated cultures of 337 ±15 kPa and 335 ±10 kPa, respectively, are well aligned with the previously published values for *M. aeruginosa* PCC7806 of 330 ±90 kPa (Dunton & Walsby, 2005). However, 24 h following BMAA treatment the CCP significantly decreased, with continued weakening of GVs noted over the course of measurement (ΔCCP=131 ±15 kPa; 96 h). At the end of the experiment the weakest GVs collapsed at pressures below 100 kPa (Figures

5.2c and 5.3, respectively). The decreased CCP following BMAA treatment was found to be statistically significant for four of the five replicate measurements collected during days two through five (Figure 5.2c), with the degree of difference between the BMAA treated and control samples continuing to increase during this period ($t=3.615$ to $t=8.914$; $p<0.05$).

5.4.1b Photopigment response to BMAA treatment

During the experiment, phycocyanin (PC) and phycoerythrin (PE) decreased in the BMAA treated cultures, with the greater change occurring in PE (Figures 5.2d & 5.2e, respectively). Based on the results of Student's *t*-test comparing PC, PE, and Chl-a in replicate BMAA-treated and control samples, few of the time points showed statistically significant differences as compared to controls (Figures 5d-5e). However, regression analysis of specific growth rate (μ) based on Chl-a, PC, and PE for the control (μ=0.045, μ=0.149, and μ=0.059, respectively) and BMAA-treated (μ=0.022, μ=0.031, and $\mu=1x10^{-11}$, respectively) groups indicated decreased photopigment production in response to BMAA treatment over the course of measurement.

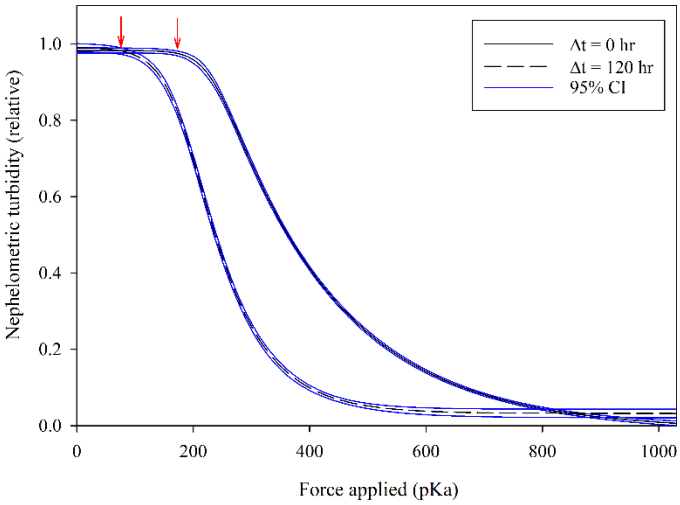

Figure 5.3: 4-parameter sigmoid fittings and 95% confidence intervals (CIs) of pressure nephelometry GV collapse profiles pre- and post-BMAA treatment in cultures of Microcystis aeruginosa PCC7806.

5.4.1c Colony formation

Figure 5.4 illustrates the changes in the degree of colony formation of the BMAA treatment compared to controls. Based on image analysis, 72 h post-spike 63.3% of the population in the BMAA treated cultures had aggregated into colonies with more than twenty cells per colony, as compared to 28.9% in controls; no aggregates with greater than twenty cells per colony were found in the pre-spike control (Table 5.1). The total relative abundance of the population due to colonial aggregates in the BMAA treated samples was found to be 30.5% greater than that of control samples.

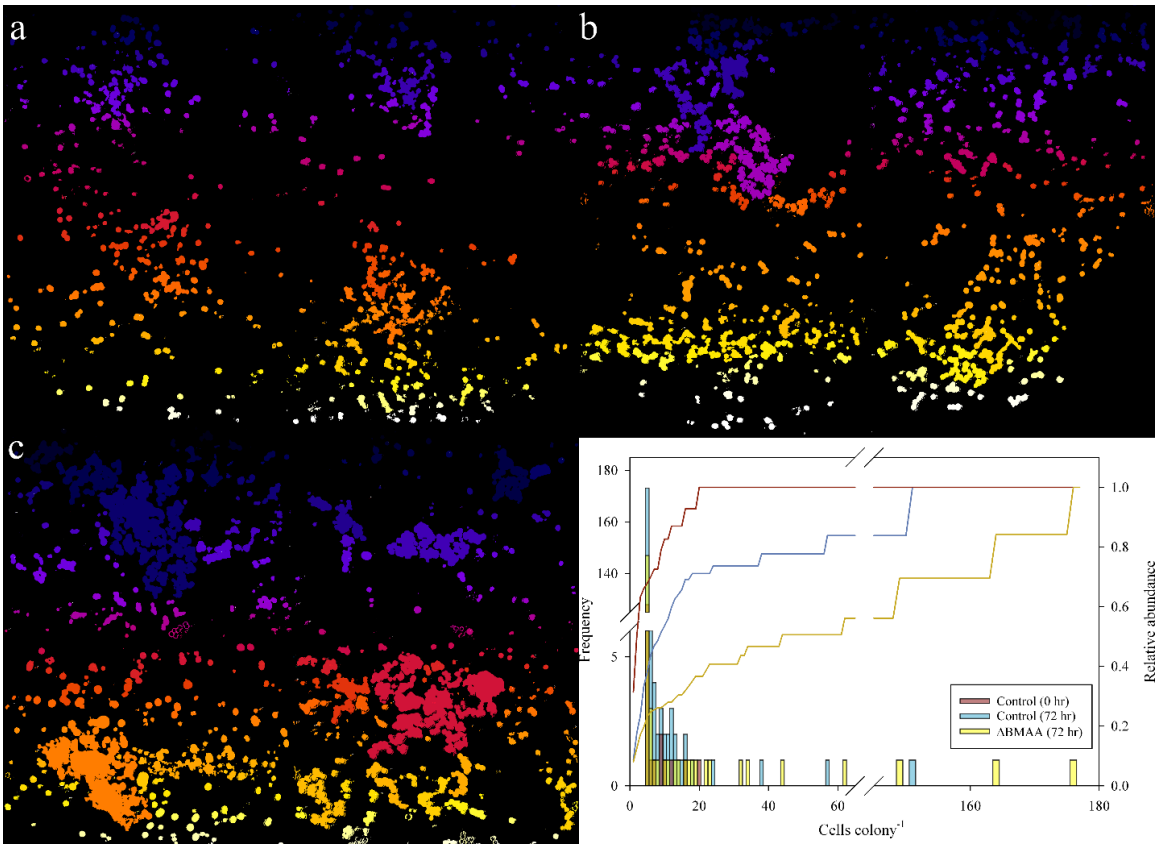

Figure 5.4: Self-organizing object maps of colonial aggregates generated from HPMA permanent slides showing BMAA driven colony formation in Microcystis aeruginosa PCC7806: (a) control, pre-spike; (b) control, 72 h post-spike; (c) ΔBMAA, 72 h post-spike; (insert) Pareto histogram of colony size frequency distribution for control (0 & 72 hrs, red and blue, respectively) and BMAA treated (yellow) cultures.

5.4.1d Cell morphology and growth

Image analysis of the BMAA treated and control samples was performed for glutaraldehyde preserved samples collected immediately prior to, and 72 h post, BMAA treatment. For both control and BMAA treated cultures, photopigment autofluorescence was preserved over the course of measurement, as was the presence of intact GVs (Figure 5.5). No

change in cell size or cytoplasmic volume was noted in BMAA treated cells, as compared to controls, and no statistically significant difference in cellular abundance was observed (Table 5.1).

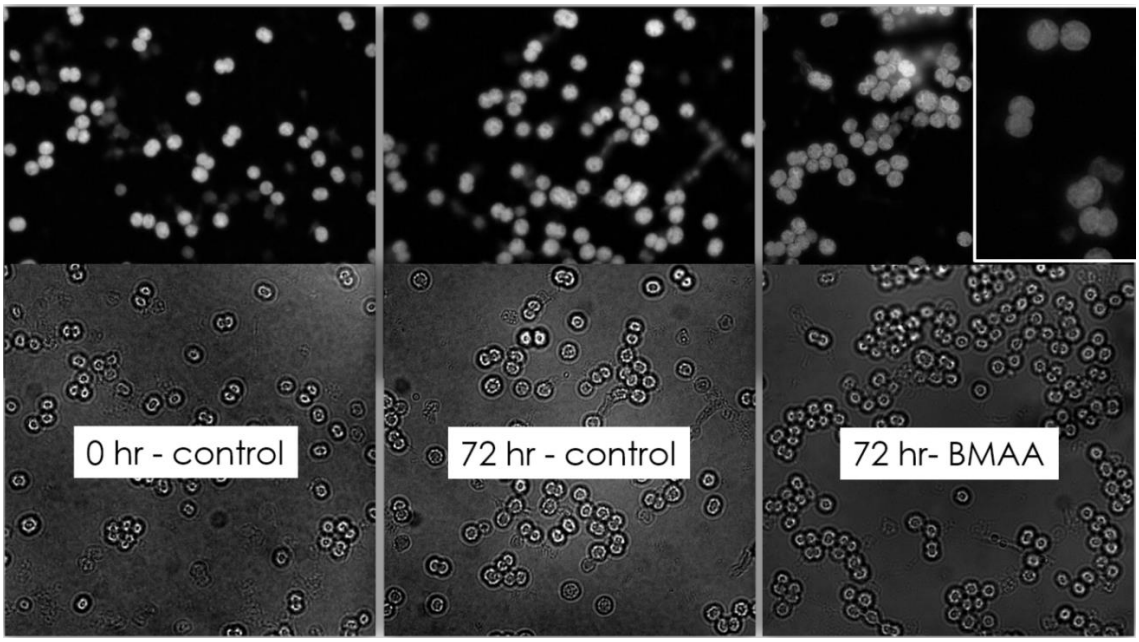

Figure 5.5: (top) CLSMs and (bottom) phase contrast micrographs of Microcystis aeruginosa PCC7806 cultures. For both control and BMAA treated cultures, GVs are present as refractile bodies in the phase contrast images, and cell viability is demonstrated via photopigment autofluorescence in the CLSMs.

Table 5.1: Mean cell size (n=25) and colony size in cultures of *Microcystis aeruginosa* PCC7806 in response to BMAA treatment.

Sample	time (hr)	cell diameter (μm)	cytoplasmic volume (μm^3)	Mean colony size (cells colony^{-1})‡	Cell abundance (cells FOV^{-1})
Control	0	4.0±0.2	23.6±6.2	2.25 (1-20)	90±45
	96	4.1±0.4	23.9±6.2	8.45 (1-151)	159±46
ΔBMAA	96	4.2±0.4	24.8±6.2	44.2 (1-176)	149±39

‡Range of values given in parenthesis

5.4.2 Laboratory culture discussion

The observed increase in PST in both the control and BMAA treated cultures may reflect different processes. In the control, the increase is most likely tied to increased cell growth, which is reflected in the relatively higher growth rate. The BMAA treated cells had a small decrease in growth rate, and thus the increase in PST is more likely due to a relative increase in GV formation. Based on the growth rates derived from PC and PE in the control and BMAA treated cultures, the observed change in phycobilin concentrations may indicate that protein reserves were being mobilized for enhanced GV synthesis in response to BMAA. Thus, BMAA might be acting to balance cellular responses due to nutrient and photooxidative stress; with enhanced buoyancy allowing for faster upward movement, and decreased CCP attenuating the surface residence-time needed to become negatively buoyant, leading to enhanced vertical migration capability. Despite the observed chlorotic response, no difference in cell size or cytoplasmic volume was noted between BMAA treated and control samples (Table 5.1), suggesting that cells were not nutrient limited, despite the observed chlorotic response typical of nutrient stress in cyanobacteria (Görl, et al., 1998; Chien et al., 2012). The maintenance of chlorophyll autofluorescence and continued cellular fission also indicate that cells remained viable and continued to grow (Figure 5.5).

The similar rate of GV collapse (Figure 5.2a), compared to the decrease in CCP (Figure 5.2c), in the BMAA treatment is evidence of alteration in the effective CCP of the total population of BMAA-treated cells, as changes to a subset of the population would result in a broadening of the collapse profile and a decrease in the value of the gradient (i.e. more negative). Further, the decreases in CCP due to BMAA did not occur immediately, but instead showed a 24 h delay and then continued to increase over the measurement period (ΔCCP=131 $\pm$15 kPa; 96 h).

The delayed response may reflect the incorporation of BMAA into GV proteins, or as is here proposed, alterations in interprotein interactions leading to a weakened state. The growth of GVs occurs via elongation of the cylindrical mid-section by insertion of GvpA monomers, with elongation to a mature length taking >12 h (Buchholz et al., 1993). It is here proposed that BMAA may be effecting the CCP of GVs via association with GvpA monomers within the growing GV segments (see section 5.5), as opposed to eliciting immediate changes in metabolism that increase cell turgor, and hence, decrease the CCP of turgid cells.

Gas vesicles respond to increased turgor pressure by reducing volume; previous culture studies using *Anabaena flos-aquae* CCAP1403/13*f* found that exposure to high light intensity for prolonged periods (135 μmol m^{-2} s^{-1} for 16-23 hr) generated increased turgor pressure of up to 240 ±100 kPa, and was accompanied by large decrease in GV volume (Kinsman et al., 1991). Studies in *Microcyctis aeruginosa* MASH01 have also demonstrated decreased GV volume in response to high light treatments due to turgor upshift, where the increased turgor is due in equal parts to the rapid production of soluble carbohydrates and light-induced uptake of ions (Allison & Walsby, 1981; Walsby, 1994; Brookes & Ganf, 2001). As our cultures were maintained under low light conditions (30 μE m^{-2} s^{-1}) on a 14/10 light/dark cycle, increased turgor is unlikely to account for our observed decrease in CCP in response to BMAA treatment.

Prior culture experiments using continuous lighting conditions in *Nostoc* sp. PCC 7120 exposed to 20 μM BMAA noted elevated glycogen concentrations as compared to controls, indicating that BMAA promotes the generation of energy stores (Berntzon et al., 2013). However, the energetically costly process of glycogenesis is undertaken specifically because glycogen effectively removes the osmotic load cells would otherwise experience from the photosynthetic accumulation of soluble carbohydrates, and is thus unlikely to account for the

decrease in CCP we observed in response to BMAA treatment (Oakley & Young, 1936). Moreover, the increase in relative PST in the BMAA treated cultures indicates increased GV volume—a finding opposite of that which would occur if increased turgor were causing the decrease in CCP, as turgor induced CCP decreases coincide with decreased GV volume. This interpretation is also supported by our previous findings using cultures of *Microcystis aeruginosa* PCC7806 maintained under the same 14/10 h light cycle and at the same light fluence rate. Under these conditions, the turgor associated change in CCP in controls (ΔCCP=38.4 ±9.0 kPa) measured over the course of an eight hour light period (Figure 3.9), was far less than the magnitude of the decrease in CCP we observed in BMAA treated cultures (ΔCCP=131 ±15 kPa; 96 h), and returned to a baseline value following the respiration-associated dark cycle (see Chapter 3, Section 3.5.5).

In addition to a substantial decrease in CCP in response to BMAA treatment, an increase in the degree of colony formation was measured. Based on image analysis, 72 h post-spike 63.3% of the population in the BMAA treated cultures had aggregated into colonies with more than twenty cells per colony, as compared to 28.9% in controls; no aggregates with greater than twenty cells per colony were found in the pre-spike control. In thermally stratified systems, increased colony size enhances vertical migration, where hydrodynamic drag and the surface area-to-volume ratio of colonies decrease in tandem (Sterner, 1989; Walsby, 1994).

5.4.3 Laboratory culture summary

The observed cellular responses to BMAA treatment indicate that the compound elicits changes in metabolic state and morphology that synergistically act to increase the relative gas vacuolization of cyanobacteria while simultaneously making less robust GVs; likely as a stress avoidance mechanism. Truncation of the phycobilisome antennae complex—apparent from

decreases in PC and PE—decreases the likelihood of photoinhibition, as occurs in nutrient limited and/or excessively illuminated cells (Schwarz & Grossman, 1998). Increased colony formation increases the maximum rate of vertical migration that planktonic cells can achieve, in addition to enhancing tolerance to high-light conditions (Walsby, 1994; Holland & Kinnear, 2013; Meissner et al., 2015). Continued production of GVs allows for the maintenance of DVMs, and more rapid returns to surface layers following nutrient scavenging from depth, while the production of GVs with decreased CCPs hastens the transition from positive-to-negative buoyancy due to photosynthesis-associated turgor increases, and hence, limits surface residence times (Oliver & Walsby, 1984; Gao et al., 2016). These combined adaptations are therefore likely to result in both decreased photooxidative and nutrient stresses in thermally stratified systems, by maintaining a tight link between physically separated energy and nutrient pools. It is therefore proposed that thermal stratification resulting in combined nutrient and photooxidative stresses leads to the production of BMAA by gas-vacuolate cyanobacteria, and that the compound elicits metabolic adaptations that allow for more efficient vertical migrations.

5.4.4 Ross Island Lagoon environmental time series results

5.4.4a Physical site description

Ross Island Lagoon (Figures 5.1 & 5.6), located near Portland, Oregon, USA in the Willamette River, Oregon, USA, is an approximately 200 acre artificial impoundment that is accessed via a 500-foot-wide opening with the Willamette River. For more than eighty years, the lagoon was used as a mining and processing site for sand and gravel, resulting in a maximal depth of approximately 30 m, while the main channel of the Willamette River adjacent to the lagoon is approximately 14 m deep. Due to the improper disposal of contaminated fill and cement wastes within the lagoon, multiple areas of elevated pH and zinc-ion concentrations have

been noted, with a maximum pH of 11.39 measured in 2007 at the sediment-water interface (ODEQ, 2011).

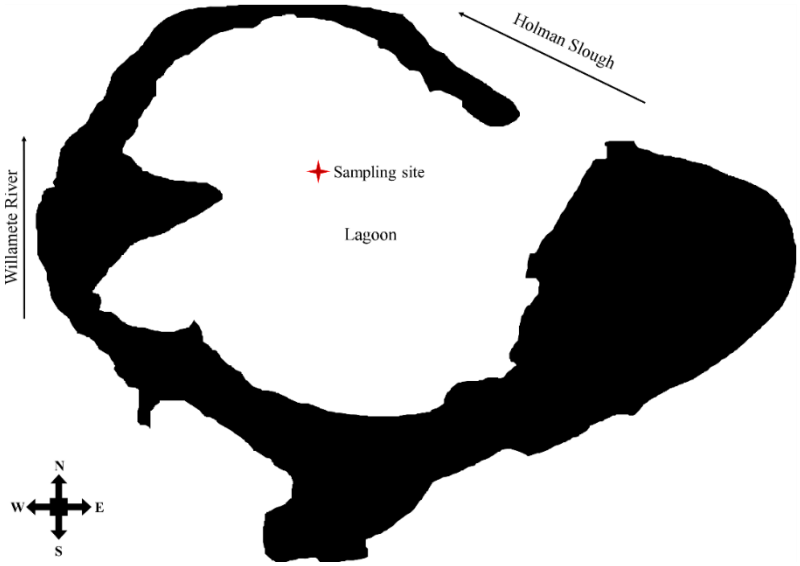

Figure 5.6: Ross Island Lagoon site map.

5.4.4b Density stratification

Water column depth profiles of temperature collected during the course of the time series illustrated temporal changes in the depth and stability of the seasonal thermocline within Ross Island Lagoon (Figure 5.7), with the stability and homogeneity of the surface mixed layer increasing from late July to early September, 2017. During this period, water temperatures at the air-water interface decreased by approximately 4°C, and the boundary layer between the seasonal thermocline and the nutrient rich deep layer increased from approximately 10 m to 15m in depth (Figure 5.7). The greatest rate of change in the depth of the seasonal thermocline was observed to occur between the 08/22/17 and 08/30/17, past which point temperature variability within the surface mixed-layer was less than 3°C. Apart from minor rainfall on 08/14/17, no precipitation was observed during the course of monitoring. In the weeks following 08/25/17,

average temperatures remained constant, while both average and sustained wind speeds fell to the lowest values observed during the time series, further stabilizing the surface mixed-layer (Figure 5.8).

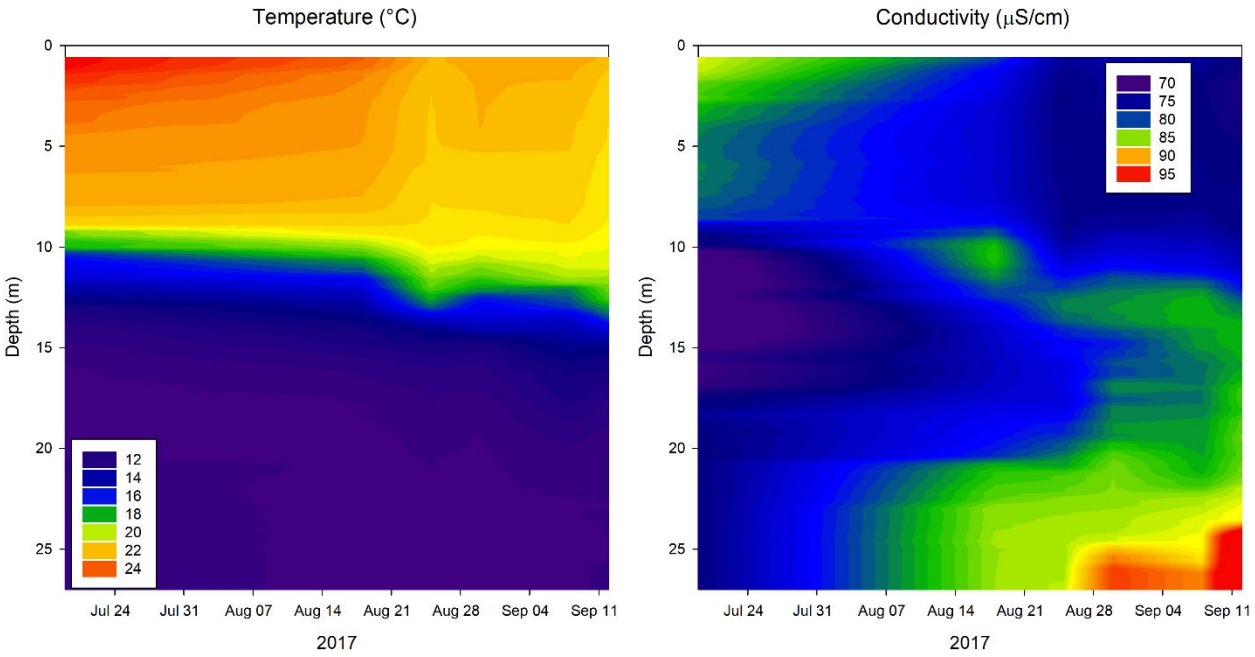

Figure 5.7: Contour map of changes in thermocline and conductivity characteristics within Ross Island Lagoon over the course of bloom development and collapse; 07/19/17 to 09/12/17.

5.4.4c Conductivity shifts within the lagoon

The conductivity profile was found to vary in a similar fashion to the temperature profile; at the start of the time series—prior to stabilization of temperature gradients—the conductivity maxima occurred within the top 5 m of the lagoon, and proceeded to shift towards greater depths in tandem with the thermocline. However, subsequent to the 08/25/17 sampling point the conductivity maxima were observed to fall below the seasonal thermocline, despite the temperature within the hypolimnion remaining invariant over the course of the time series

(Figure 5.9). The greatest conductivity values were observed at the end of the time series, and occurred within 5 m of the sediment-water interface (Figure 5.7).

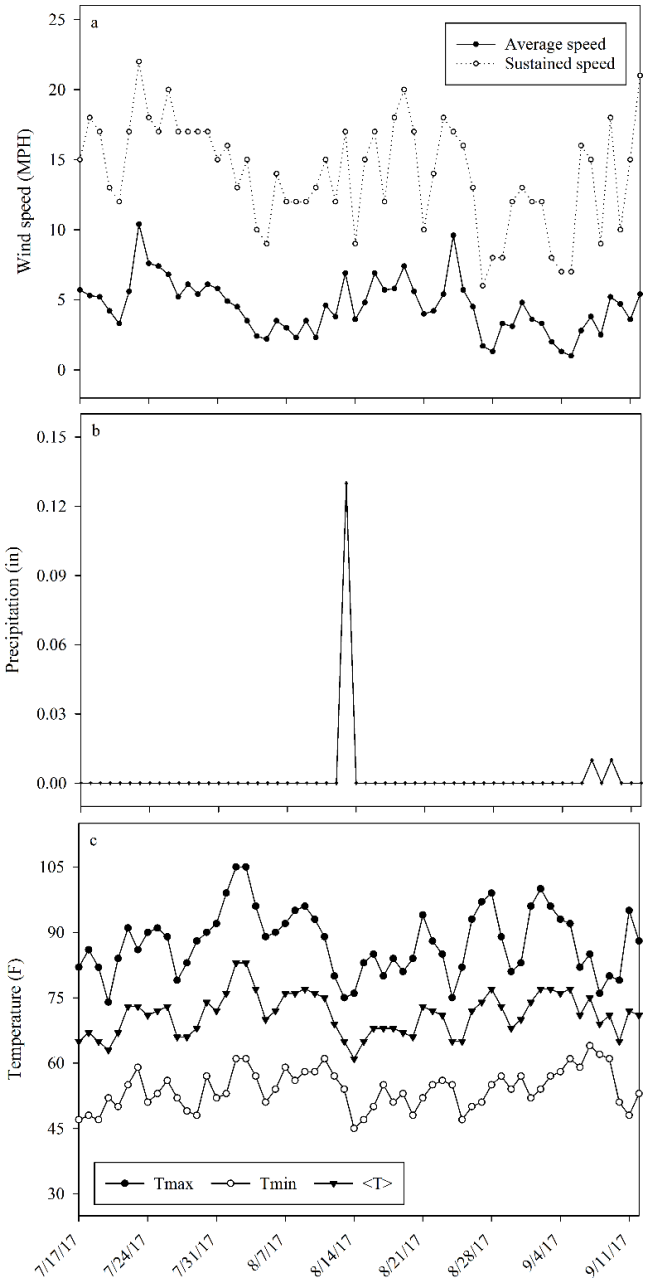

Figure 5.8: Local climatological data for the Portland, Oregon during the course of the Ross Island Lagoon environmental time series.[5]

[5] NOAA (2019).

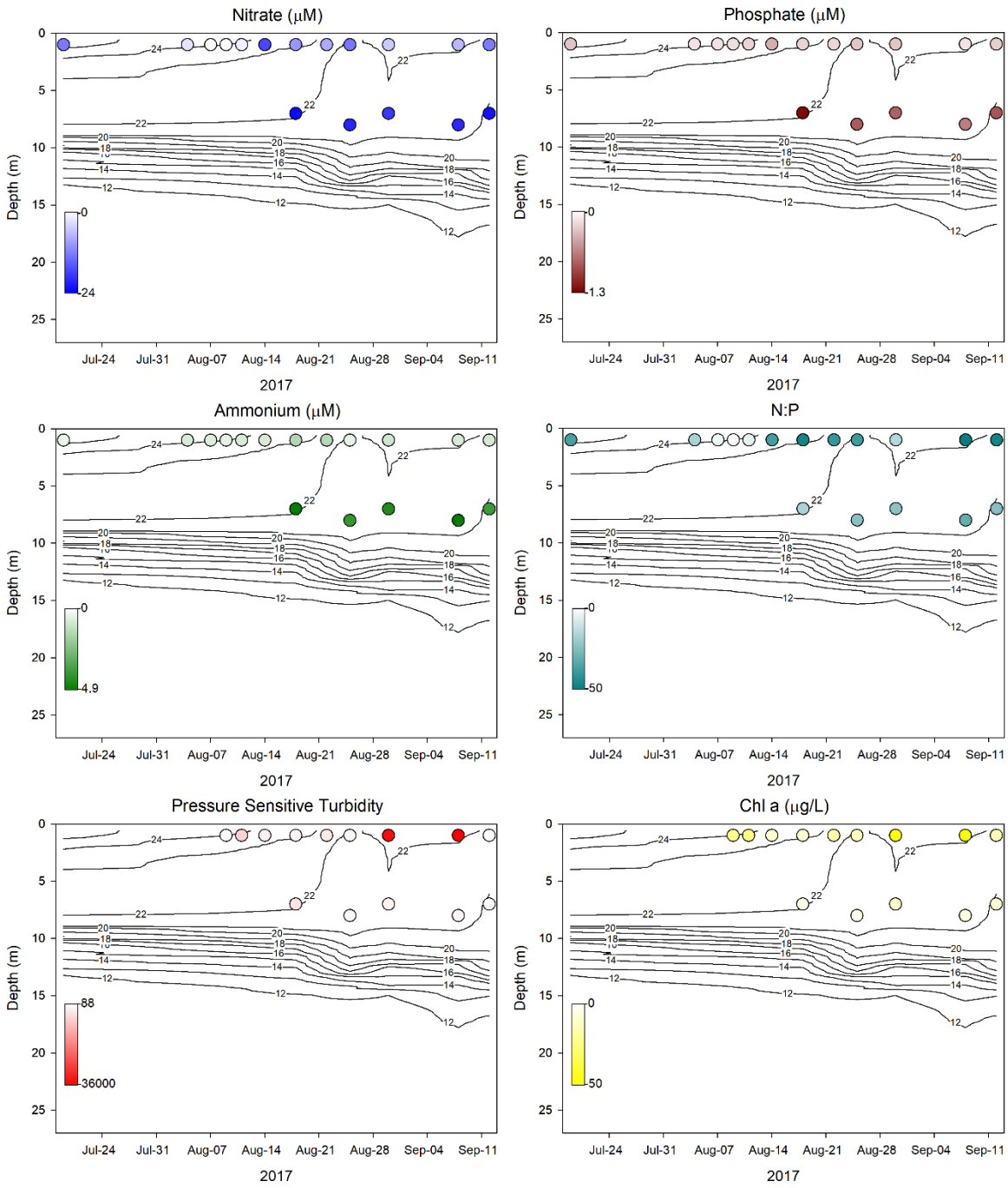

Figure 5.9: Nutrient and biomass fluxes over the development and collapse of a Microcystis sp dominated harmful algal bloom within Ross Island Lagoon. Temperature isopleths (°C) based on CTD casts provided for comparison to parameter changes with respect to thermocline characteristics.

5.4.4d Nutrient & biomass changes

Examining the nutrient fluxes within our study site, we found that dissolved concentrations of both phosphate and nitrate/nitrite within the epilimnion fell below the half-saturation constants (*Kp*=0.2 and *Kn*=5.6 μM, respectively) required for balanced growth in phytoplankton populations at multiple points in time (Klausmeier et al., 2004). Dissolved concentrations of nitrate/nitrite and ammonium ranged from 17.3-1.25 μM and 1.46-0.67 μM, respectively, and concentrations of phosphate and silica ranged from 0.41-0.13 μM and 267-209 μM, respectively (Figures 5.10; Table 5.2). Variability in the concentration of dissolved nutrients was inversely correlated with chl-α concentration, which ranged from 79.3-18.8 μg L^{-1}, indicating nutrient uptake due to the growth of phytoplankton populations (Figure 5.9). Wind-induced mixing events on 08/14/17 and 08/25/17 are proposed to have temporarily alleviated nutrient stress within the surface mixed-layer, leading to rapid increases in cellular abundance (Figures 5.8 & 5.9). Nutrient limitation leading to increased oxidative stress—subsequent to stabilization of the surface mixed layer—was also indicated by the concurrent increase in pheophytin concentrations during time points for which phosphate and nitrate/nitrite uptake resulted in concentrations below their half-saturation constants (Figure 5.9; Table 5.2). During the latter half of the time series, samples were collected from depth (7-8 M) via Niskin bottle, for which the nutrient concentrations were found to greatly exceed those of the surface grab samples (Table 5.2). No samples from depth were collected for which the combined nitrogen or phosphate concentrations were found to be limiting (Figure 5.9; Table 5.2).

Table 5.2: Water quality measurements for Ross Island Lagoon time series.

Date & depth		**PO_4**	**Silicic acid**	**NO_2**	**NO_3**	**NH_4 (fluor)**	**N:P**	**Chl**	**Pheo**	**PST**	**BMAA**
	(m)			(μM)				(mg L^{-1})	(RFU)	(counts)	(ng g^{-1})
7/19/17	0	0.30	249.75	0.78	12.40	0.43	43.47	-	-	-	-
8/7/17	0	0.14	259.75	0.04	0.40	0.62	7.29	-	-	-	-
8/9/17	0	0.16	260.85	0.03	0.20	0.49	4.28	40	0.449	8.8E+04	28.0
8/11/17	0	0.21	265.40	0.12	1.25	0.75	9.50	42.1	0.471	6.8E+06	33.4
8/14/17	0	0.41	267.15	1.16	17.30	0.72	44.48	19.6	0.243	2.1E+06	38.7
8/18/17	0	0.21	230.80	0.51	9.75	1.46	54.68	18.8	0.274	1.3E+06	37.3
8/18/17	7	1.26	257.10	0.62	23.05	4.77	22.16	12.3	0.176	3.6E+06	-
8/22/17	0	0.20	248.00	0.40	7.85	1.41	47.46	29.7	0.381	3.0E+06	43.4
8/25/17	0	0.29	250.40	0.24	12.80	0.46	45.72	22.8	0.284	1.4E+06	39.7
8/25/17	8	0.84	233.90	0.19	20.55	3.89	29.27	10.2	0.172	1.3E+06	-
8/30/17	0	0.29	212.30	0.31	4.90	0.92	20.05	76.3	0.847	3.5E+07	58.1
8/30/17	7	0.80	245.50	0.19	18.70	4.25	28.87	19.6	0.270	1.4E+06	-
9/8/17	0	0.13	208.85	0.58	6.50	0.75	57.96	79.3	0.946	3.7E+07	36.7
9/8/17	8	0.66	197.35	0.61	20.05	4.78	37.62	13.9	0.219	1.3E+06	-
9/12/17	0	0.24	216.85	0.52	12.25	0.77	55.40	27.5	0.314	3.4E+05	16.6
9/12/17	7	0.87	211.25	0.63	22.25	3.71	30.01	16.9	0.224	5.9E+05	-
Standard Deviation of Replicate Measurements											
7/19/17	0	0.115	6.15	0.055	2.4	0.015	n/a	-	-	-	-
8/7/17	0	0.01	2.25	0	0	0.1	n/a	-	-	-	-
8/9/17	0	0.01	0.75	0	0.1	0.055	n/a	1.4	0.022	1.4E+06	15.1
8/11/17	0	0.03	3.2	0	0.05	0.005	n/a	0.9	0.012	1.2E+06	23.1
8/14/17	0	0.075	0.45	0.02	0.1	0.165	n/a	0.6	0.274	6.7E+04	9.0
8/18/17	0	0.035	2.6	0	0.05	0.1	n/a	0.4	0.176	5.6E+05	21.9
8/18/17	8	0.015	8.5	0.01	0.05	0.085	n/a	2.5	0.022	8.2E+05	-
8/22/17	0	0.035	1.4	0	0.15	0.055	n/a	0.3	0.004	1.8E+05	10.3
8/25/17	0	0.02	3.15	0.2	0.2	0.21	n/a	0.3	0.004	1.8E+05	5.8
8/25/17	7	0.005	21.3	0	0.05	0.01	n/a	1.6	0.020	4.2E+05	-
8/30/17	0	0.03	0.4	0.04	1.3	0.045	n/a	11.6	0.121	5.8E+06	2.6
8/30/17	7	0.035	9.9	0.03	0.9	0.15	n/a	5.0	0.038	1.5E+05	-
9/8/17	0	0.025	0.35	0.13	0.2	0.045	n/a	5.2	0.038	7.5E+06	10.2
9/8/17	8	0.06	8.65	0.005	0.15	0.08	n/a	1.7	0.021	2.6E+05	-
9/12/17	0	0.045	6.95	0	0.35	0.01	n/a	0.7	0.009	6.6E+04	4.6
9/12/17	7	0.035	27.05	0.005	0.25	0.075	n/a	0.9	0.008	2.2E+05	-

5.4.4e Pressure sensitive turbidity & BMAA

Pressure sensitive turbidity (a proxy for GV abundance), was found to be strongly correlated with extracted Chl-α concentration ($R=0.978$, $p<0.0001$). The PST signal increased by seven orders-of-magnitude over the development of the bloom (Figure 5.10), with peak values occurring concurrent to Chl-α, pheophytin, and BMAA maxima, and dissolved nutrient minima (Table 5.2). BMAA concentrations were found to range from below the lower limit of quantification (LLOQ=23 ng g^{-1} lyophilized material) up to 58.1±2.7 ng g^{-1} lyophilized material (Figure 5.10; Table 5.2), and showed a strong negative correlation ($R=-0.846$, $p<0.02$) with the N:P ratio. Principle component analysis indicated strong associations between BMAA concentration, pheophytin concentration, the size of the gas vacuolate population as indicated by PST, and the depth of the thermocline (Figure 5.11). Subsequent to the peak BMAA concentration, a decrease in CCP across peaks was observed, and it was noted that low-CCP colonial aggregates became dominant during the latter stages of bloom progression (Figures 5.10, 5.12 & 5.13).

The results of the quantification method for BMAA, AEG, and DAB are based on, and referenced to, the amount (in mg) of lyophilized starting material used for each sample (as in Chapter 2). As this quantification scheme does not account for the size of the planktonic population, a one-fold per-cell increase in BMAA concentration is assumed to have occurred over the time series (Figure 5.10; Table 5.2). However, if the BMAA concentrations are normalized to the fold-change in Chl-α concentration or PST—used as biomass proxies—from the corresponding sampling dates, a much different picture emerges; the absolute BMAA concentration underwent a 10-fold increase, with peak concentrations occurring immediately prior to bloom collapse.

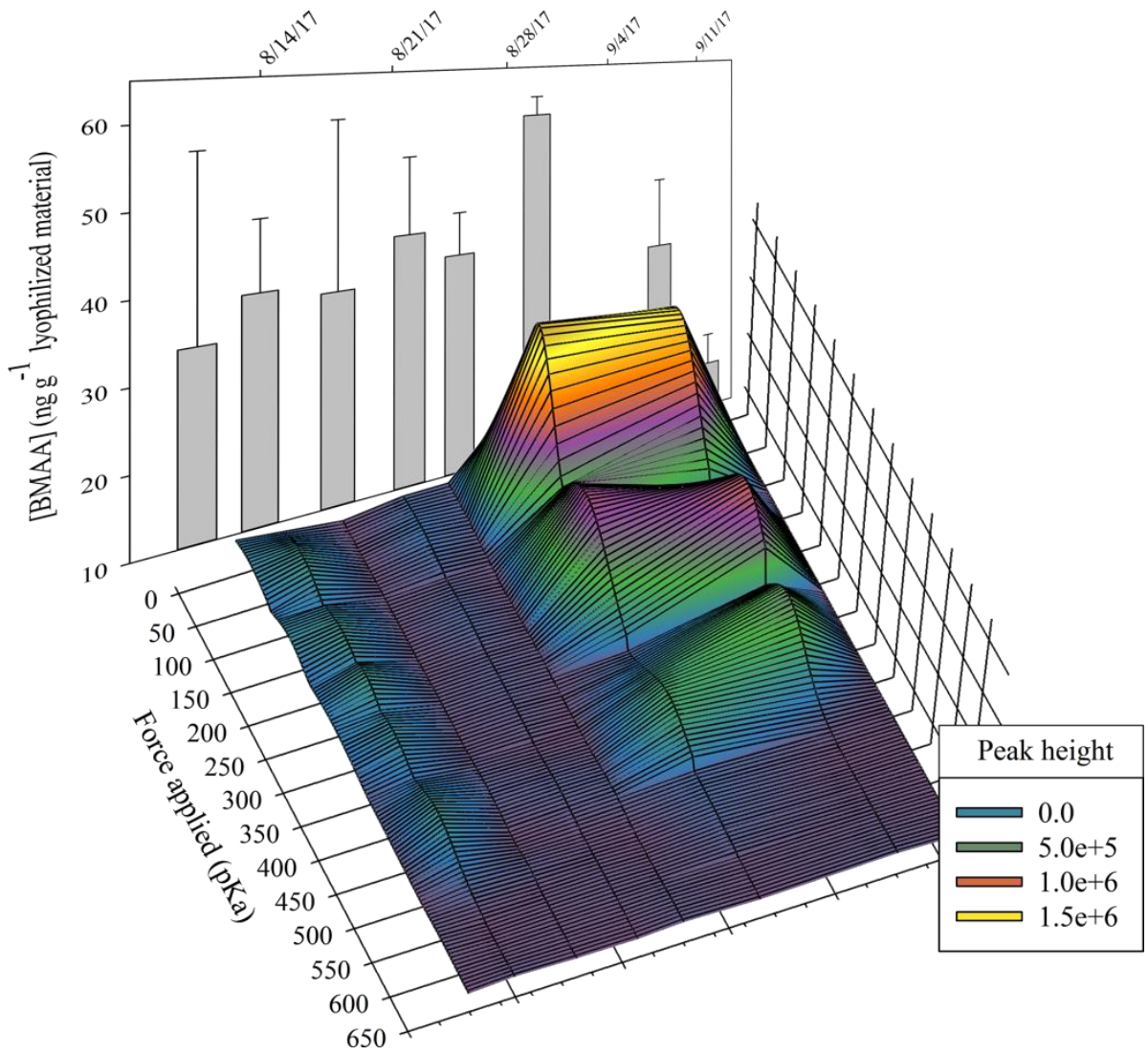

Figure 5.10: (top) Change in BMAA concentration over the development and collapse of a Microcystis sp dominated harmful algal bloom (bottom) change in PST of specific gas vacuolate populations during the course of measurement; maximum BMAA concentration (58.1 ±2.6 ng g^{-1} lyophilized material) and PST signal occur on 08/30/17, followed by disappearance of the gas-vacuolate population and BMAA presence (<LLOQ).

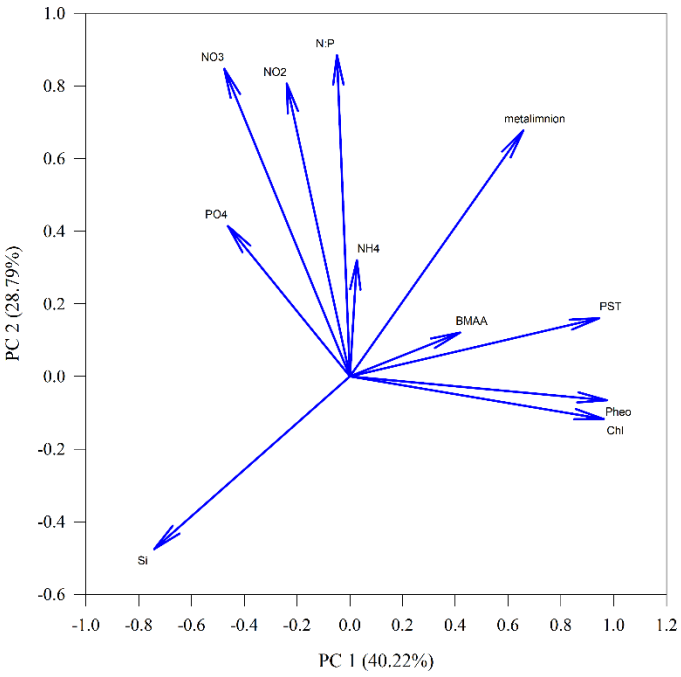

Figure 5.11: Principal component correlation loadings for water quality parameters associated with BMAA production over the course of measurement within Ross Island Lagoon.

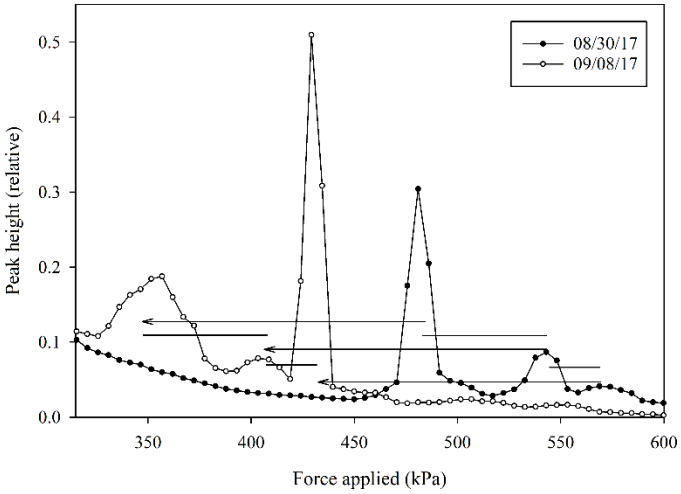

Figure 5.12: Change in CCP of conserved peaks from 08/30/17 to 09/08/17 subsequent to peak BMAA concentrations; intraday spacing of peaks is maintained between sampling points, and the decrease in CCP between dates is constant for all peaks (ΔCCP≅137 kPa) and comparable to the shift observed in culture experiments in response to BMAA treatment (ΔCCP=131±15 kPa).

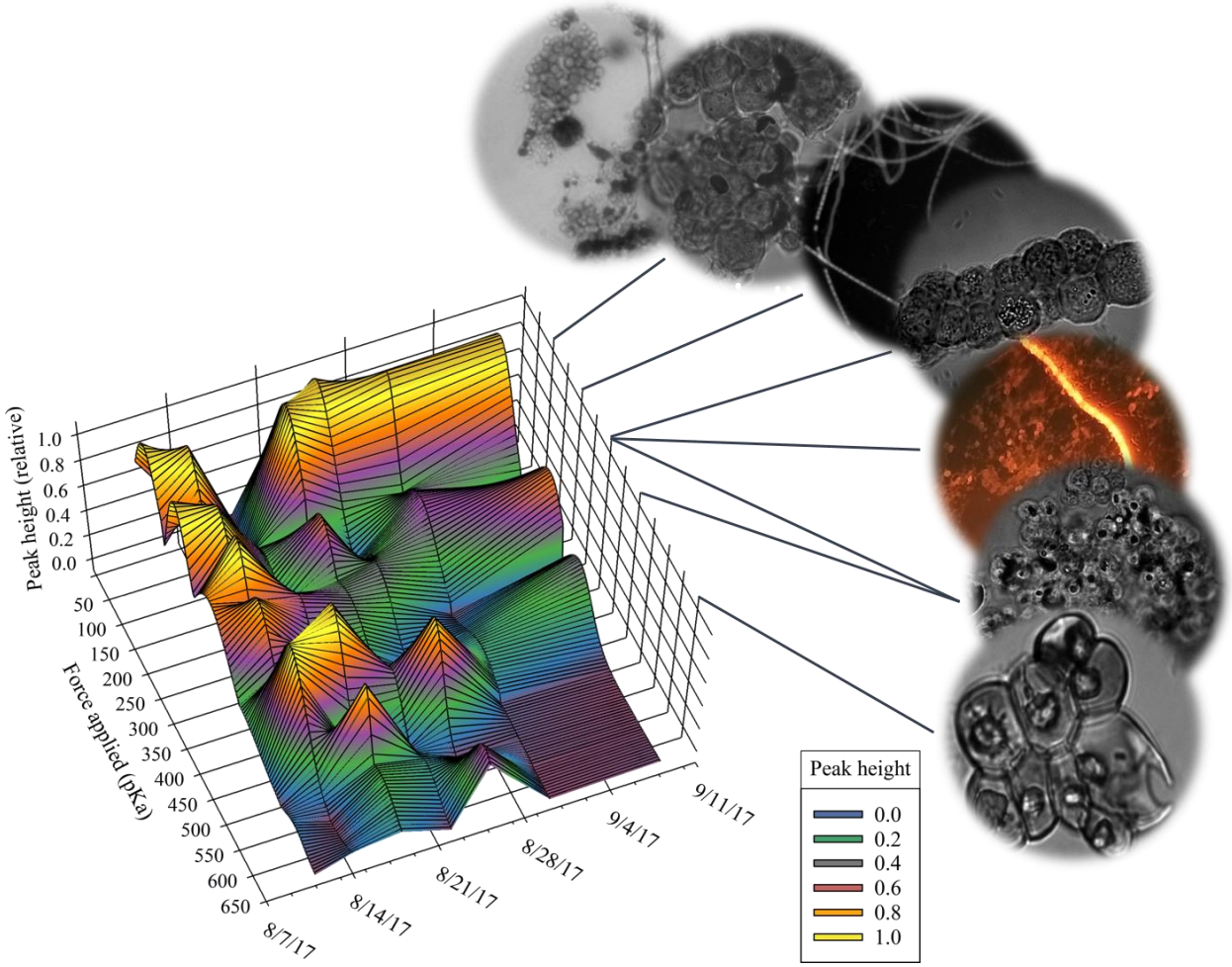

Figure 5.13: Change in relative (intraday normalization) PST distribution of specific gas-vacuolate populations during the course of measurement. Population shifts towards low-CCP, colonial aggregates during the latter stages of bloom progression, in tandem with increased BMAA concentration, noted to occur.

5.4.5 Ross Island Lagoon environmental time series discussion

Examining the nutrient shifts within our study site, we found that the surface concentration of both phosphate and nitrate/nitrite became limiting to GV synthesis at multiple time points (Figure 5.9, Table 5.2). Culture studies using *Microcystis aeruginosa* MASH01

reported large reductions in relative gas vacuolization when cultures were inoculated in medium with nitrate and phosphate concentrations below 10 μM and 0.5 μM, respectively, as compared to nutrient replete cultures (Brooks & Ganf, 2001). However, comparing nutrient variability from our environmental time series to the change in PST, we see that the largest increase in PST coincided with growth limiting nitrate and phosphate concentrations—based on surface-grab samples—suggesting that cells were successfully migrating to depth for nutrient resupply and sustained GV synthesis (Figure 5.10; Table 5.2). Coinciding with the period of greatest nutrient limitation within the surface mixed-layer, we also observed maximal pheophytin concentrations (Table 5.2), as would be expected in phytoplankton populations experiencing resource competition in concert with photooxidative stress (Rehman et al., 2013). The increased pheophytin concentration is presumably a result of photoinhibitory conditions and increased rates of cell death. Further enhancing nutrient competition within the epilimnion and concurrent to the period of greatest nutrient limitation, increases in the depth of the seasonal thermocline boundary layer were observed (Figures 5.7 & 5.9). Nutrient competition within thermally stratified systems favors more rapid transitions from positive-to-negative buoyancy in order to access nutrients from depth during DVMs, while also selecting for enhanced buoyancy in the competition for carbon species and PAR from surface boundary layers following nutrient resupply (Ibelings et al., 1994; Walsby, 1994). This juxtaposition provides an ecophysiological motivation for enhanced GV content with decreased CCP and increased colony formation, as these adaptations are here proposed to hasten the transition between positive and negative buoyancy, and vice versa, due to photosynthate accumulation and respiration, respectively, resulting in increases in DVM efficiency and the maximum achievable depth of migration. Evidence for increased DVM depth by the buoyant population is provided by concurrent shifts in

the conductivity maxima within the thermocline boundary layer, the depth of the seasonal thermocline, and nutrient depletion within the surface mixed layer (Figures 5.7 & 5.9). The increased conductivity at depth is proposed to be due to the presence of colonial cyanobacteria aggregates linked via exopolymeric substances (EPS) matrices, and the solubilization of EPS-localized calcium carbonate—generated during photosynthesis—as the aggregates descend into the water column (Morse et al., 2007; Kamennaya et al., 2012).

Correlated with increased nutrient stress, metalimnion depth, and BMAA concentration, the CCP distribution of the buoyant populations—as determined from pressure nephelometry measurements—underwent large shifts, resulting in decreased CCP across all populations and coinciding with the peak measured BMAA concentration of 58.1±2.7 ng g^{-1} lyophilized material (Figures 5.10 & 5.12). We have previously shown that CCP as determined via pressure nephelometry is species-specific and constant during periods of balanced growth (Chapter 4). The large shift in the CCP of the population may be indicative of pervasive nutrient limitation and photooxidative stress, and is here proposed to have driven the observed increase in BMAA concentration as a means of increasing access to nutrients from depth. Further, the decrease in CCP across all populations indicates that the mechanism of CCP decrease due to BMAA is likely conserved within gas vacuolate cyanobacteria (discussed below).

Subsequent to the peak in BMAA concentration and coinciding with bloom collapse, disappearance of the dominant pressure sensitive populations (CCP<150 kPa) was noted to occur (Figure 5.10). Based on the change in hydrostatic pressure due to depth (approximately 10 kPa m^{-1}), and the depth of the seasonal thermocline layer during this period (Figure 5.7), the CCP of these populations is proposed to have fallen below the hydrostatic pressure they were subjected to during DVMs, leading to GV collapse at depth and removal of these cells from the buoyant

population. Further, following the decrease in CCP across populations and concurrent to disappearance of the buoyant population based on PST (Figure 5.10; Table 5.2), BMAA concentrations fell to levels below the lower limit of quantification (LLOQ=23 ng g^{-1} lyophilized material). Bloom collapse and sedimentation of the buoyant population within the lagoon, and a correlation between BMAA and the buoyant cyanobacteria population, is further supported by time series measurements of PC fluorescence collected immediately downriver from Ross Island (Figure 5.14), where no increase in PC was detected subsequent to disappearance of the buoyant population within the lagoon (USGS, 2017).

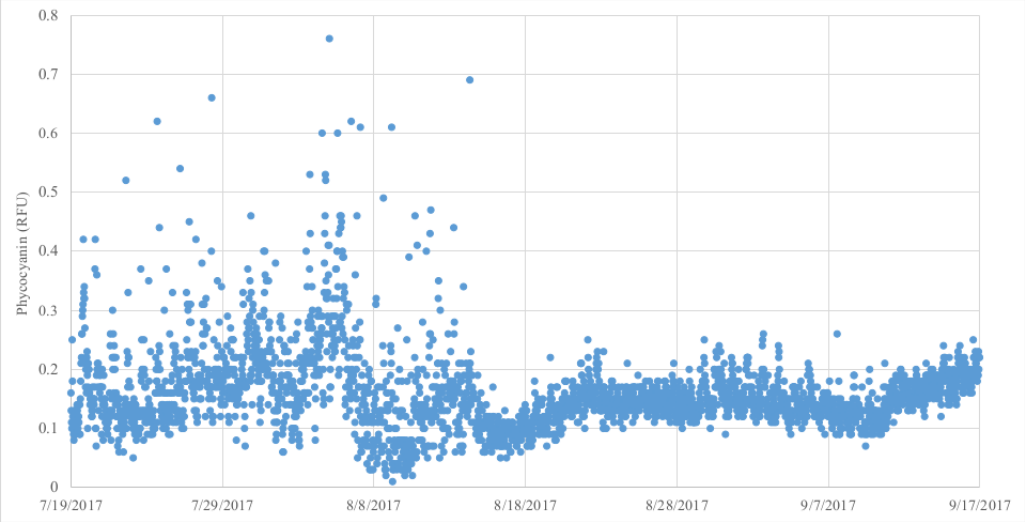

Figure 5.14: Phycocyanin fluorescence detected downriver from Ross Island within the mainstem of the Willamette River during the course of the lagoon time series (USGS, 2017).

Principal component analysis of the water quality parameters recorded during the time series indicates that changes in BMAA concentration were most strongly correlated with pheophytin concentration, the depth of the thermocline boundary layer, and the size of the PST signal—attributed to gas vacuolate cyanobacteria—indicating a role in stress responses as has previously been reported and here attributed to buoyancy modulation in response to

photooxidative stress (Downing et al., 2011; Downing et al., 2012; Pip et al., 216). The chemical synthesis studies of Pfammatter & Seebach (1991) demonstrated direct synthesis of BMAA via hydrolysis of an imidazolidine precursor analogous to 5-hydroxy-5-methylhydantoin—the predominant photochemical DNA lesion generated during strong UVR exposure under oxic conditions (Breimer & Lindahl, 1985). Based on the effects on CCP due to BMAA we have presented, and the nutrient limitation within the surface mixed-layer that occurred immediately prior to bloom collapse, we propose that BMAA is generated from UVR-associated DNA lesions in cyanobacteria experiencing photooxidative and nutrient stress.

5.5 Proposed mechanisms of BMAA action on GVs

5.5.1 Altered electrostatic interactions with GvpA

BMAA treatment of replicate cultures of *M. aeruginosa* PCC7806 (MICAE_210002; Figure 5.15) resulted in a decrease in the CCP of GVs, with the first statistically significant decrease in CCP, as compared to controls, occurring approximately 24 hours after the BMAA spike (Figure 5.2c; $[BMAA]_{final}$=10μM). No decrease in GV volume/abundance, as compared to controls—determined via PST measurements and cell counts—occurred as a result of BMAA application. This indicates that the decrease in the CCP of GVs due to BMAA treatment is not turgor associated, and is therefore likely a result of modifications to the sequence and/or structure of the gas vesicle proteins (GVPs) that comprise the GVs—specifically GvpA (Oliver & Walsby, 1984; Brookes & Ganf, 2001). Analysis of the mechanism underlying the BMAA-associated change in CCP, and the variability in the innate CCP among cyanobacteria species, is hindered by the lack of a well refined atomic structure for both GvpA and the larger GV assembly. However, speculation of how BMAA might affect the CCP of GVs can be made based on a combination of results from prior studies, including: (i) fiber-based (solution) x-ray

crystallography of GVs (Blaurock & Walsby, 1976); (ii) MALDI-TOF mass spectrometry analysis of GV and GvpA proteolysis products (Belenky et al., 2004; Dunton et al., 2006), (iii) 2D NMR characterizations of GvpA secondary structure and solvent accessibility (Sivertsen et al., 2009/10), (iv) FTIR spectroscopy-assisted structural modeling of GvpA secondary structure (Strunk et al., 2011), and (v) TEM analysis of the effects of point mutations in GvpA, and deletions from the C-terminus of GvpA, on GV structural integrity and GV shape (Strunk et al., 2011).

Rapid responses to metabolic and environmental changes, specifically associated with light exposure and nutritional status in this context, are often enacted through the post-translational modification (PTM) of proteins. These PTMs include the phosphorylation, methylation, acetylation, nitrosylation, glutathionylation, and N-glycosylation of target residues flanked by specific recognition sequences and/or at sites occurring within distinct conformational motifs (Kemp & Pearson, 1990; Nothaft & Szymanski, 2013; Chardonnet et al., 2015; Grabsztunowicz et al., 2017). Based on the sequence of GvpA, and the structure of intact GVs, it is unlikely that the decrease we observed in the CCP of GVs in *M. aeruginosa* PCC7806 (MICAE_210002; Figure 5.15) in response to BMAA treatment is a result of the covalent PTM of GvpA monomers. Environmentally stimulated proteolytic modification to structurally important segments of GvpA, leading to vesicle weakening, is also unlikely. It is here proposed that the modulation of GV integrity due to BMAA in planktonic cyanobacteria is a result of direct electrostatic interactions between BMAA and GvpA at the cytoplasmic face of GvpA monomers, and leads to decreased CCP via alterations in the ability of GvpC to associate with GvpA monomers that have recently been added to the growing segments of GVs (discussed below).

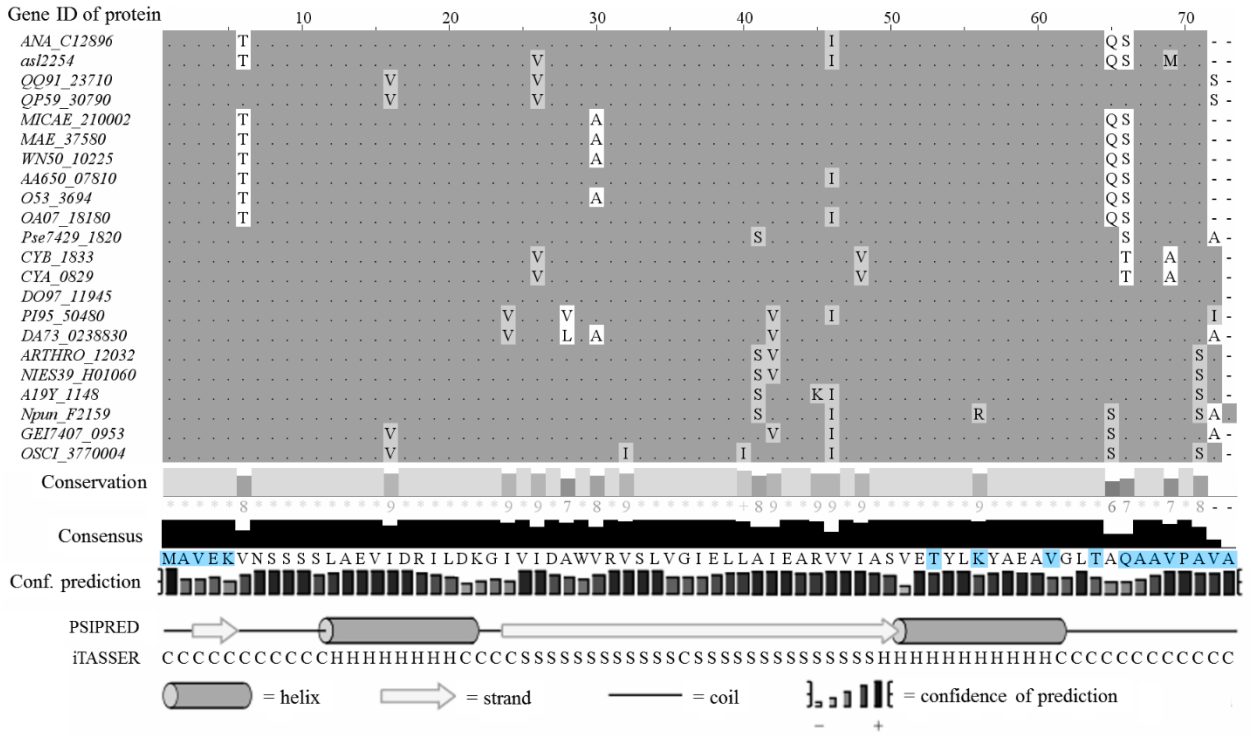

Figure 5.15: Sequence alignment (Clustal), and predicted secondary structure elements (PSIPRED & iTASSER) of the consensus sequence (solvent accessible residues indicated in blue), for gas vesicle protein A (GvpA) derived from freshwater cyanobacterial reference strains (KDRI database). The core 51-residue segment (S9-A60) containing α-helix I and both β-sheet regions, is highly conserved among cyanobacteria, halobacteria, and enterobacteria. The C-terminus containing α-helix II is variable among cyanobacterial orthologs, and a high degree of variability in both sequence identity and length occur in GvpA homologs from other organisms.

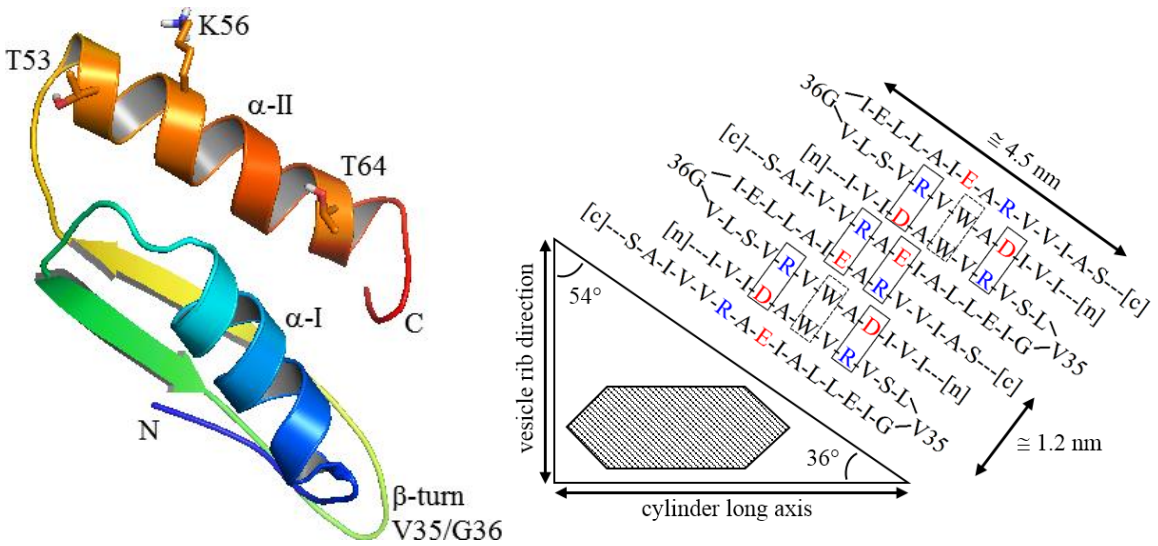

Figure 5.16: (left) Cartoon rendering of GvpA secondary structure (iTASSER) corresponding to the best prediction based on the GvpA consensus sequence given in Figure 1, α-II is positioned on the solvent-exposed exterior face of GVs and interacts with the GV stabilization protein, GvpC; (right) Predicted topology of gas vesicle ribs formed by the β-sheet portion of GvpA based on the consensus sequence. All charged and aromatic residues are oriented on one face of the β-sheet, and engage with adjacent GvpA monomers via salt bridge formation and pi-stacking, respectively.

The overall topology of GvpA monomers as determined from the 2D NMR analysis of Sivertsen et al., (2010), which conforms to structural predictions from the fiber x-ray crystallography studies of Blaurock & Walsby, 1976, is highly conserved between orthologs (Figure 5.16). The secondary structure of GvpA monomers and quaternary structure of the GV shell precludes the possibility of modifications to and/or cleavage at a majority of reactive residues within the GvpA subunits. Within the highly conserved 51-aa core segment of GvpA monomers (Figure 5.15; S9-A60 of the consensus sequence), all of the D-X, E-X, K-X, and R-X bonds have been shown to be inaccessible to proteases in aqueous suspensions of intact GVs (Belenky et al., 2004; Dunton et al., 2006). This inaccessibility presumably results from the

orientation of these residues on the hydrophobic interior of the GV shell and/or their participation in non-covalent interactions with adjacent GvpA monomers, as in Figure 5.16 (Sivertsen et al., 2010; Ezzeldin et al., 2012). Further, the accessible portions of GvpA in cyanobacteria lack any homology to known recognition sequence motifs for Ser/Thr- and Tyr-based kinases (Figure 5.15), making phosphorylation of structurally important residues within GvpA unlikely (Kemp & Pearson, 1990; Zhang et al., 2007). Moreover, and while it does not cover all possible scenarios for the various cyanobacteria—especially within the context of environmental populations—the MALDI-TOF mass spectrometry studies of Belenky et al., (2004) failed to detect any PTM of GvpA monomers. Despite these results, regulation of GV integrity via PTMs resulting in altered GvpA and/or GvpA:GvpC structural characteristics cannot be ruled out, as there are multiple conserved and solvent accessible residues within the C-terminus of GvpA that would typically act as the nucleophilic sites of PTM via methylation and/or acetylation (Sivertsen et al., 2010). However, decreased GV content was not observed in our BMAA treated cultures, and no glutamate residues exist near solvent exposed lysine residues for any of the species examined (Figure 5.15), thus precluding the possibility of acetylation based on our current understanding of the mechanism in bacteria (Carabetta & Cristea, 2017). Likewise, no cysteine residues are present in any of the GvpA sequences examined, and no asparagine residues exist within the accessible portions of GVs associated with GvpA, indicating that nitrosylation and glutathionylation, and N-glycosylation, respectively, are not involved in the regulation of GV integrity (Nothaft & Szymanski, 2013; Chardonnet et al., 2015; Grabsztunowicz et al., 2017). Altered GvpA characteristics due to methylation cannot entirely be ruled out.

Specific residues within the C-terminal region of GvpA are of great importance in the regulation of GV integrity. Based on the results of trypsin cleavage and carboxypeptidase-Y (CPY) digestion experiments on GVs isolated from cultures of *A. flos*-aquae CCAP1403/13*f*, the N- and C-terminal penta- and octamers, respectively, are solvent accessible (Belenky et al., 2004). However, tryptic cleavage at K5-V6 of GvpA (Figure 1; ANA_C12896) did not affect GV integrity or conformation, nor did CPY digestion of the accessible octamer of the C-terminus. The variable C-terminal region of GvpA acts as the docking site for the scaffolding protein GvpC, which binds to GvpA in a non-covalent manner and stabilizes GV quaternary structure. In cells of *Anabaena flos-aquae* CCAP 1403/13*f* the innate CCP (i.e. no turgor influence) was found to decrease from 630±2 kPa to 210±1 kPa when intact GVs were stripped of GvpC (Dunton et al., 2006). The importance of electrostatic interactions between the conserved and solvent accessible lysine and threonine residues within the variable C-terminus of GvpA on GV integrity—due to associations with GvcC (Dunton et al., 2005)—are highlighted by the mutation and deletion studies of Strunk et al., (2011), where a KΔL mutation within α-helix II (Figure 5.15; K56L of the consensus sequence) abolished GV integrity. Deletion of an 11-aa segment of the C-terminus containing the solvent exposed, conserved threonine residue was also shown to be detrimental to GV integrity and formation (Strunk et al., 2011). However, a deletion mutant lacking a 7-residue C-terminal segment, distal to the conserved threonine, resulted in cells with GV characteristics analogous to the WT strain, akin to the results obtained from CPY digestion of the C-terminal octamer (Belenky et al., 2004; Strunk et al., 2011).

To date, no mutation studies of the additional solvent exposed residues (Figure 5.15: T53 and V61 of the consensus sequence) of GvpA have been performed. However, it is likely that these residues are involved in the regulation of GV structure and stability as they are fully

conserved across all species analyzed, lay within the structurally important C-terminus of GvpA, are solvent accessible, and are capable of participating in electrostatic interactions.

Minor variations in amino acid sequence within the C-terminus of GvpA between cyanobacterial orthologs—in addition to variable baseline turgor pressures—may also partially account for the variability in effective CCP that occurs between. Comparing the GvpA sequences for *M. aeruginosa* PCC7806 and *Pseudanabaena* sp. PCC7429 (Figure 5.15; MICAE_210002 and Pse7429_1820, respectively) the only variation in the C-terminus exists at residue 65; Q65 vs A65, respectively (Figure 5.15). Solvent accessibility for this residue, based on iTASSER structure and function predictions, is greater in MICAE_210002, and non-covalent glutamine interactions have been identified as important contributors to the intermolecular association of proteins (Rhys et al., 2012). Comparing the results of our pressure fraction experiments and the detection of species via characteristic CCP (Chapter 4; Table 4.1), we also see that *Microcystis* sp. possessed a greater CCP than the *Pseudanabaena* sp. analyzed (310-455 kPa vs 231-259 kPa, respectively), which may be due to more favorable GvpA-GvpC interactions.

The growth of GVs occurs via insertion of GvpA monomers into the center of the cylindrical GV segment, with elongation to a mature size taking > 12 h, where the addition of GvpC to the surface of GVs occurs as the vesicle grows (Buchholz et al., 1993). Recent studies indicate that strong electrostatic interactions occur between BMAA and charged/polar functional groups, resulting in altered protein folding even is the absence of de novo protein synthesis (Downing & Downing, 2016; van Onselen & Downing, 2018). Based on our observed decrease in CCP due to BMAA treatment and the timeframe of the response—indicative of changes in CCP associated with growth of the GVs—it is likely that electrostatic interactions are occurring between BMAA and GvpA at structurally important and solvent exposed residues of GvpA

monomers as they are incorporated into the larger GV structure, thus preventing GvpC from associating with the growing segments. This interaction is here proposed to occur at the conserved, and solvent exposed residues of the C-terminus of GvpA (Figure 5.15).

Over time, the association of BMAA with GvpA in the proposed manner would result in larger and larger GV segments, and a greater intracellular percentage of GVs, unable to interact with GvpC. This type of BMAA/GvpA interaction is in line with the attenuation in the CCP of GVs that we observed in BMAA treated cyanobacteria cultures (Figure 5.2c), where CCP continued to decrease over the 96 h period following BMAA treatment. In addition, if BMAA production occurs in response to environmental stressors and if these stressors were to cease, the proposed mechanism would allow cells to return to a baseline buoyant state, as continued cellular growth would dilute the effects of BMAA on the total complement of GVs within a cell. Further, the residues within GvpA that are here proposed to interact with BMAA are fully conserved between the cyanobacterial orthologs examined, thus providing a conserved ecophysiological response to BMAA within buoyant cyanobacteria populations, consistent with the evolutionary history of planktonic cyanobacteria.

In addition to the I-TASSER secondary structure predictions for GvpA, structure-function, protein homology, and ligand binding models were compiled using the COFACTOR and COACH prediction platforms; no ligand binding sites were identified and no proteins with an appreciable degree of structural similarity were found. However, the structural alignments for GvpC from *Microcystis aeruginosa* PCC7806 (MICAE_210002), identified a high degree of homology (TM-score: 0.544; Figure 5.17), with the α-chain of the cytoskeletal protein tropomyosin—in addition to other cytoskeletal proteins, including α-Actinin and the neck region of Myosin V (Phillips, 1986; Yang & Zhang, 2015). Previous electron paramagnetic-resonance

(EPR) studies utilizing the protein- and lipid bilayer-specific spin labels 2,2,6,6-tetranethyl-4-maleimidopiperidine-1-oxyl (MAL6) and 5-doxylstearic acid, respectively, found a concentration-dependent response to BMAA treatment in the protein spectrin, resulting in altered protein-protein interactions (Butterfield et al., 1993). Spectrin is the dominant cytoskeletal protein associated with regulating the strength, shape, and flexibility of erythrocyte membranes (Butterfield et al., 1993). Further, while the EPR spectra for the MAL6 labels was clearly altered in response to BMAA treatment, no change associated with the 5-doxylstearic acid label was detected (i.e. no change in the physical state of the lipid bilayer occurred), leading to the conclusion that the altered spectrin-associated, protein-protein interactions were as a direct result of non-covalent interactions between BMAA and spectrin (Butterfield, 1992). Within the erythrocyte membrane skeleton, spectrin-tropomyosin associations—in addition to multiple other interprotein interactions—act to support the larger cytoskeletal scaffold (Bennett & Lambert, 1987; Machnicka et al., 2014). Thus, the observed change in spectrin structural characteristics in response to BMAA treatment (in the absence of de novo protein synthesis), further supports a role for BMAA in modulating interprotein interactions via altered electrostatic interactions—as we have here proposed for GVs.

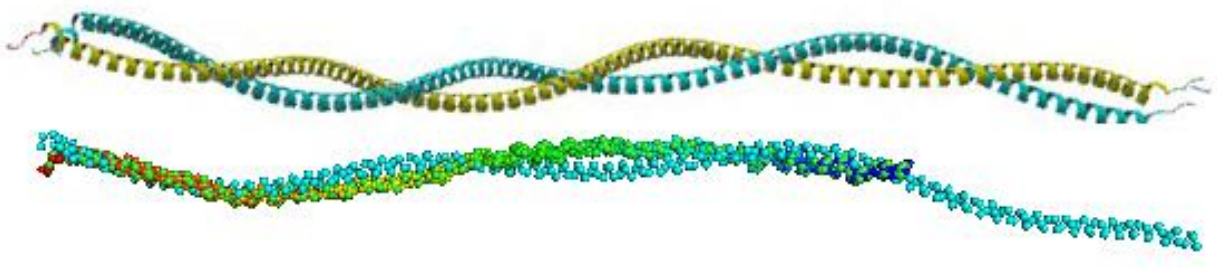

Figure 5.17: (top) structure of alpha- (yellow) and beta-chains (teal) of the cytoskeletal protein tropomyosin; (bottom) structural homology of GvpC from *Microcystis aeruginosa* NIES843 to the alpha chain of tropomyosin.

5.5.2 Direct incorporation of BMAA into GvpA

Mechanisms other than the electrostatic disruption of GvpA:GvpC associations leading to GV weakening, in response to BMAA treatment, are also plausible. Principally, BMAA may be incorporated into the protein primary structure of GvpA and modulate the CCP of GVs via a cycle of isopeptide formation and reversal, driven by nucleophilic attack of the BMAA β-amine on the *N*-carbonyl of the peptide backbone (Figure 5.18). Direct incorporation of BMAA into protein primary structure, and the ability to modulate protein secondary structure elements, are supported by prior studies, including: (i) structural characterization of the peptide antibiotic Galantine-I isolated from *Bacillus pulvifaciens*, which contains BMAA (Figure 5.19; Sakai & Ohfune, 1992), (ii) determination of isopeptide speciation within Polymyxin-M resulting from transpeptidation by the BMAA isomer DAB (Silaev et al., 1966), and (iii) examination of the effects of isopeptide formation on protein secondary structure using synthetic ogliopeptides containing BMAA in the central position of small α-helices (Blodgett & Loudon, 1989; Seebach et al., 1994).

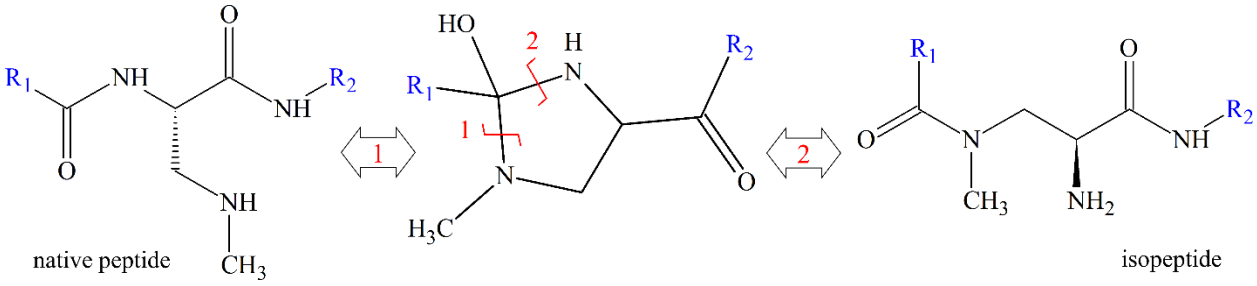

Figure 5.18: Isopeptide formation in BMAA containing peptides. The native peptide is here proposed to be the preferred conformation at neutral to acidic pH ranges and low carbonate concentrations. Cycilization (1), is proposed to occur spontaneously upon activation of the BMAA β-amine as a nucleophile, with subsequent formation of a stable isopeptide (2), being favoured under elevated carbonate and oxygen concentrations.

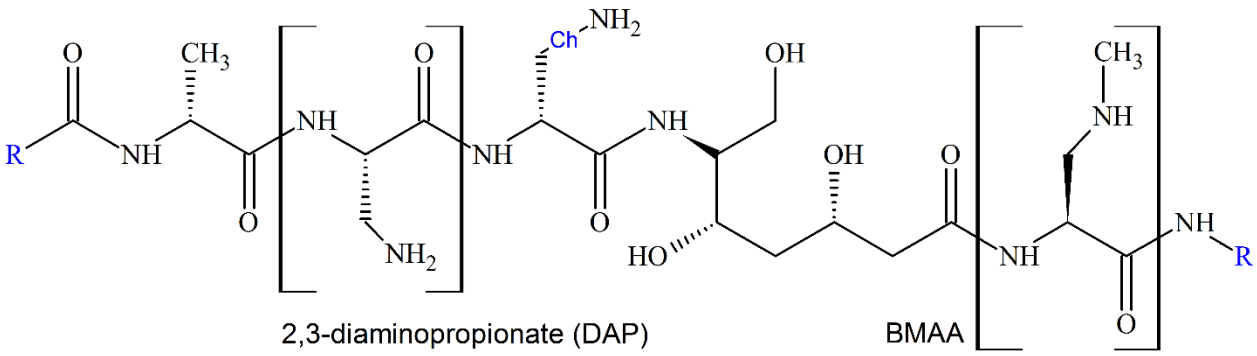

Figure 5.19: Core structure of the peptide antibiotic galantin I isolated from *Bacillus pulvifaciens* (Sakai & Ohfune, 1992).

On the basis of NMR comparisons of synthetic Galantin-I to that isolated from *Bacillus pulvifaciens*, Sakai and Ohfune (1992), determined that both BMAA and DAP exist as naturally occurring residues within the peptide backbone of Galantin-I (Figure 5.19). However, Galantin-I contains multiple atypical amino acids (e.g. D-ornithine, D-lysine, L-DAP, L-BMAA, and galantinic acid), leading to the proposal that its biosynthesis occurs via non-ribosomal peptide-synthetase (NRPS) and/or polyketide synthase (PKS) modules (Nunn & Codd, 2017). To date, no biosynthetic route for Galantin-I has been confirmed, and while NRPS/PKS modules are often involved in the biosynthesis of cyanotoxins, none are known to contain BMAA (Meriluoto et al., 2017). Despite the lack of a biosynthetic mechanism for Galantin-I, the demonstrated incorporation of BMAA into a peptide backbone may lend support to the results of Dunlop et al., (2013), which argued for misincorporation of BMAA during de novo protein synthesis. Incorporation of BMAA into the peptide backbone was proposed to arise from competition between BMAA and serine for seryl-tRNA, and upon protein incorporation, to result in misfolding (Dunlop et al., 2013). The prior proposal remains contentious, however, oxidative stress has been shown to result in elevated instances of misacylation by aminoacyl-tRNA

synthetases (aaRS), and to impair the editing ability of mischarged aaRS, resulting in elevated instances of mistranslation (Ling & Söll, 2010).

The direct incorporation of BMAA into GvpA may offer additional benefits over the electrostatic associations described above, based on the fact that GVs are functional β-amyloid proteins (Walsby, 1994; Sivertsen et al., 2010). Within gas vacuolate cyanobacteria, GVs can account for up to 10% of the total protein complement, which is a startling concentration of functional β-amyloid protein, as gas vacuolate cells must possess a means of recycling GvpA monomers and preventing the irreversible aggregation of amyloid plaques (Walsby, 1994; Broome & Hecht, 2000). The cyclic rearrangement of BMAA via an isoaspartate-like intermediate has been proposed and is known to occur in similar biogenic peptides containing α,β-diamino acids (Silaev et al., 1965; Blodgett & Loudon, 1989; Downing & Downing, 2016). Within the α,β-diamino acid-containing peptides analyzed, the spontaneous formation of isopeptide species was shown to be strongly catalyzed by bicarbonate, in a pH dependent fashion, and to be favored under conditions of elevated P_{O_2}; transpeptidation was shown to result in the loss of helical conformation present in the native peptides (Blodgett & Loudon, 1989; Karle et al., 1991; Seebach et al., 1994).

Due to the colocalization of the photosynthetic/respiratory ETC and the NDH-$I_{3/4}$ CO_2-hydrating systems within the thylakoid membrane of cyanobacteria—associated with O_2 and bicarbonate production, respectively—the conditions that occur within dense HAB states, and which favor CCM induction, also favor the formation of isopeptide species by α,β-diamino acid-containing peptides—specifically those near the cytoplasmic face of the thylakoid membranes (Blodgett & Loudon, 1989; Woodger et al., 2005). Spontaneous reversal of isopeptide species has also been demonstrated, where the isopeptide is stable for prolonged periods but reverts to a

native state under more acidic conditions, as would occur within cells undergoing DVMs and distinct photosynthetic/respiratory cycles (Seebach et al., 1994; Badger et al., 2008).

Reversal of α,β-diamino-containing amino acids to a native state via a cyclic intermediate has also been shown to act as a "β-breaker" element, allowing for the disruption of insoluble β-sheet aggregates; in this case proposed to allow collapsed GVs to be recycled via dispersal of the aggregated β-sheets likely to form upon GV collapse (Sivertsen et al., 2010; Nadimpally et al., 2014). This type of cycle receives further support from isotope labeling studies in *Anabaena flos-aquae* CCAP 1304/13*f*, which did not provide a mechanism but indicated that collapsed GVs are dispersed and that the constituent GvpA monomers are reassembled into growing GVs, as opposed to being degraded (Hayes & Walsby, 1984). If BMAA is being produced as a breakdown product, with elevated concentrations generated in response to environmental stressors associated with nutrient limitation concurrent to strong UVR exposure, this would also act as a temporal control on buoyancy regulation while maintaining elevated GV content. Where if the stressors were removed, and full induction of the CCMs was not necessitated, isopeptide formation might be prevented and the native GvpA conformation might be maintained, while continued production and incorporation of BMAA, and high light exposure, would continue to amplify the attenuation of CCP and result in faster buoyancy reversal, thus limiting UVR exposure and nutrient stress. However, our BMAA-treated *Microcystis* sp. cultures were maintained under low photon flux, and CCP continued to decrease over the course of measurement, indicating that direct incorporation of BMAA into GvpA, with weakening of the GV driven by isopeptide formation, is less likely than altered GvpA:GvpC associations arising from electrostatic interaction of BMAA with GvpA.

5.5.3 Summary

Despite uncertainty in the mode of action, electrostatic disruption of interprotein interactions between GvpA and GvpC, resulting in a decrease in the CCP of GVs, appears to be the most plausible explanation for our observed response to BMAA treatment. Further, BMAA is here proposed to attenuate the CCP of GVs, and enhance colony formation, in order to limit nutrient and photooxidative stress before those stressors result in the photoinhibitory cell death of buoyant cyanobacteria. The ecophysiological conditions that most favor the establishment of cyanoHABs (i.e. warm temperatures leading to thermal stratification—coupled with large populations arising from initial nutrient inputs, and ultimately resulting in resource competition), are a double-edged sword. Colonization of air/water interfaces provides an immense selective advantage within dense HAB states. However, prolonged surface residence times may generate conditions of profound photooxidative stress during periods of nutrient limitation, and if photoinhibition occurs under these conditions, the cell loses any chance of survival as migration into the water column becomes impossible. As the conditions encountered by HAB organisms one day are likely to exist the subsequent day, attenuation in the CCP of GVs due to BMAA may act as a trigger controlling buoyancy-driven DVMs, and may ultimately lead to bloom senescence once the size of DVMs becomes impossible to maintain and the magnitude of surface stressors becomes impossible to tolerate.

6. Conclusions and future directions

6.1 Significant findings

6.1.1 Overview

Validation of an improved HPLC-MS/MS method for BMAA quantification using environmental samples is demonstrated. Advancements in the pressure nephelometer design and pressure nephelometry measurement—including those that allow for species delineation of buoyant cyanobacteria in mixed microbial assemblages—are expounded on. And a proposed ecophysiological role for the cyanotoxin BMAA in the regulation of cyanobacterial buoyancy, and the effects of decreased GV integrity due to BMAA on HAB dynamics are presented.

6.1.2 HPLC-MS/MS quantification method

We developed an improved HPLC-MS/MS quantification method for the total fraction of the dansyl chloride (DNS) derivatives of BMAA, 2,4-Diaminobutyric acid (DAB), and *N*-(2-Aminoethyl)glycine (AEG). The use of ^{15}N-labelled BMAA as a stable isotope-labeled (SIL) internal standard (^{15}N-BMAA) provides a direct comparison for quantification of total BMAA, and generates a more robust (>20:1 peak area) and stable (25.8% vs 68.2% mean deviation of peak area) MS quantification transition as compared to the deuterated analogue, $^{2}H_3$-BMAA, used in prior studies. Partial method validation using ^{15}N-BMAA as a stable isotope labeled SIL demonstrated high accuracy and precision (R^2>0.999; S=0.004) over a wide range of L-BMAA concentrations (0–100 μg g^{-1} lyophilized material). The enhanced stability and decreased variability of the SIL standard resulted in improved lower limits of quantification (LLOQ) and detection (LOD) of 23 and 2.4 ng g^{-1} lyophilized material, respectively, as compared to the previously published values of 150 and 16 ng g^{-1} lyophilized material, respectively.

Method application using environmental samples was demonstrated, and BMAA was detected at several sites in the Lower Columbia River (USA), and at concentrations ranging from 23.5±4.5 to 63.3±18.1 ng g^{-1} lyophilized-material. Water residence time and cyanobacterial abundance were identified as the primary factors associated with the elevated BMAA concentrations observed at the Franz Lake and Campbell slough sites—supporting previously proposed associations between BMAA prevalence, cyanobacteria abundance, and oxidative stress conditions. Use of dansyl chloride derivatization was shown to provide a less expensive alternative to 6-aminoquinolyl-*N*-hydroxysccinimidyl carbamate (AQC)-based methods, with no performance loss. We note that the use of deuterated SIL standard variants and the derivatization buffer pH used in prior studies may have led to over estimates of total BMAA concentration and therefore contributed to the historic disagreement regarding the prevalence and abundance of BMAA.

6.1.3 Automated pressure nephelometer

Areas for improvement over previous pressure nephelometer designs were identified, including: (i) the light source, (ii) pressure regulator, (iii) and scattered light detector orientation, and using recently available technology, an automated pressure nephelometer was designed and developed. System automation and the improved scattering properties and lowered minimum integration times arising from the use of a collimated IR LED and an electronic pressure transducer, respectively, allow for millisecond sample acquisition times and enhanced pressure resolution (>1.0 kPa). Previous manual pressure nephelometer designs were constricted to pressure steps of approximately 50 kPa, and relied on human accuracy and timing in enacting pressure steps at consistent and precise intervals, with both factors effecting the interpretation of GV collapse measurements and the accuracy of calculations. While orienting the plano-convex

collimating lens of the detector just below the air-water interface of the sample cell resulted in further increases in the sensitivity of the pressure nephelometry measurement. This orientation captures changes in nephelometric scattering due to both the collapse of GVs and the resultant loss of cells with collapsed GVs as they settle out of the interrogation region. As the automated system is both pressure and time resolved, this loss of cells from the interrogation region can be used to estimate sinking velocities—a heretofore undemonstrated feature of the pressure nephelometry measurement.

Previous methods for measuring GV critical collapse pressure (CCP) were unable to generate reproducible results except when samples were taken from the same culture flask, owing to inherent differences in cultures and organisms; for example, variable pigmentation that changed white light attenuation and scattering properties. In accord with ISO7027: Water Quality—Determination of turbidity: Quantitative methods—the use of fiber optics and a high power, narrow emission profile IR LED maximizes scattering intensity while minimizing interferences from color, particle density, particle size, and stray light. This allows for comparisons of GV physical properties to be made between replicate cultures, both intraday and over the course of growth, where the CCP of *Microcystis* sp. cultures (499±4.5 kPa) recorded at 24 to 72 hour intervals over a complete growth cycle (i.e. lag, exponential, inflection, and stationary phases), was found to remain constant during balanced growth. Moreover, it was found that quantitative estimates of gas vacuolate organism abundance could be made based on changes in pressure sensitive turbidity (PST) due to growth. The specific growth rate (μ) in *Microcystis aeruginosa* PCC7806, based on PST, was found to be strongly correlated with that derived from Chl-a and/or phycocyanin (PC) ($R=0.939$ and $R=0.947$, respectively; $p<0.001$). While based on cell counts, the PST-derived rate most accurately modeled growth, thus

indicating that PST is a valid proxy for the abundance of gas vacuolate organisms. Further, the change in inferred biomass during the course of measurement was accompanied by a multiple order-of-magnitude increase in the integrated PST signal, as compared to the relative increases in fluorescence for Chl-a and PC of approx. 20% and 100%, respectively, observed during the same period. Thus, the PST measurement may be a more sensitive metric than photopigment fluorescence in assaying growth in buoyant cyanobacteria.

The indicated instrument modifications allow for direct comparison of changes in the abundance of intact GVs in culture conditions, capturing both the shape and location of inflection points corresponding to collapse thresholds under different turgor conditions and applied pressures. The effective CCP and turgor pressure of *Microcystis* sp, were found to linearly increase and decrease, respectively, with respect to external osmotic pressure, while the gradient of the collapse profiles and collapse pressure distributions (CPDs) were found to remain constant. Given that CCP varies linearly with respect to external osmolarity, and as the external osmolarity experienced by cells in the environment can be assumed to be equivalent at any discrete spatiotemporal point, changes in the metabolic status and selective advantage of a discrete subset of cells within mixed a population can be identified via a divergent change in CCP from the change observed in the rest of the gas-vacuolate population.

6.1.4 Pressure-based cyanobacteria identification

The combined results of the pressure nephelometry experiments and microscopic examination of pressure fractionated environmental samples support the interpretation that the Gaussian-distributed peaks observed in the pressure nephelometry spectra are a result of GV collapse in a predictable fashion in successive fractions of buoyant cells, where the loss of buoyancy and associated CCP generate a stable signal that can be used for species delineation.

Comparison of the collapse profiles of environmental samples collected from the same off-channel site within the Lower Columba River (USA), in the summers of 2016 and 2018 further supports this interpretation, where the CCP of peaks appearing across years are very strongly correlated ($r=0.999$, $p<10^{-9}$, $n=8$), and coincide with the dominant species from the pressure fractionation experiments.

While molecular techniques improve specificity as compared to microscopic identification, due to the elevated costs and protracted times required for sample analysis and interpretation, they do not lend themselves to routine monitoring applications. The setup time per pressure nephelometry collapse measurement is generally less than a minute, while the measurement itself—as presented for the culture and environmental assays described—ranges from 10-45 min, with immediately available results. The complete pressure nephelometry system we developed uses commercially available parts, and costs less than a basic benchtop fluorometer—with gas from a pressurized source being the only consumable.

As GVs are crucial for the dominance of bloom forming cyanobacteria within HABs, where the relative GV content increases in tandem with ecophysiological factors linked to cyanotoxin production potential, and as PST can be used as a more robust surrogate for cyanobacterial abundance than photopigment fluorescence, pressure nephelometry is a promising tool for monitoring efforts in aquatic ecosystems and the mitigation of cyanobacteria-associated human health threats. For example, *M. aeruginosa* and *M. viridis* have been shown to be the dominant microcystin (*Mcy*) producing *Microcystis* species, while *M. wesenbergii* is not believed to produce *Mcy*, with our results indicating that separation of these species is possible based on their divergent CCP and the minimal CPD overlap we observed in the pressure fractionated samples. In addition, as CCP is the effective critical collapse pressure of GVs in turgid cells,

temporal shifts in cellular metabolism associated with stress responses manifest in the pressure nephelometry measurement as alterations to the characteristic CCPs, allowing for rapid estimates of toxin production potential in routine monitoring applications (Chapter 5). Moreover, as pathogenic enterobacteria, antibiotic producing actinomycetes, and arsenic methylating halobacteria are known to produce GVs, pressure nephelometry may also be applicable for the routine monitoring of drinking water supplies and/or effluent from wastewater treatment plants. There is an urgent need for methods that are accurate, rapid, and scalable for widespread monitoring efforts surrounding our aquatic resources, and pressure nephelometry is a promising prospect.

6.1.5 Ecophysiology of BMAA

From the pressure nephelometry experiments using cultures of *Microcystis aeruginosa* PCC7806, the change in the PST signal—a proxy for total GV volume—for BMAA treated and control samples was found to be strongly correlated ($R=0.954$, $P<0.001$), while the increase in the mean GV volume (based specific growth rates for PST and Chl-a), for the BMAA treated samples was greater than that of the control. The observed increase in relative PST with decreased PC and PE may indicate that protein reserves were being mobilized for enhanced GV synthesis in response to BMAA. Further, despite the observed chlorotic response—generally an indicator of nutrient stress, no reduction in cell size or cytoplasmic volume was noted in the BMAA treated cultures, as occurs in nutrient limited bacteria.

The results of the pressure nephelometry measurements show that the mean CCP in the control and the initial CCP in BMAA treated cultures of 337 ±15 kPa and 335 ±10 kPa, respectively, are well aligned with the previously published values for M. aeruginosa PCC 7806 of 330 ±90 kPa. However, the CCP in the BMAA treated cultures drastically decreased over the

course of measurement (ΔCCP=131 ±15 kPa), with the resultant decrease causing the weakest GVs to collapse at pressures below 100 kPa. The gradient of the collapse profile remaining constant in both control and BMAA treated cultures, while the CCP decreased in BMAA treated cultures argues for alteration in the effective CCP of the total population of cells in the BMAA treated samples. Further, the decreases in CCP due to BMAA did not occur immediately and continued to magnify over the measurement period, indicating that BMAA may be effecting CCP via association with the growing segments of the GVs. Moreover, the increase in PST we observed over the course of measurement indicates increased GV volume—a finding opposite of that which would occur if increased turgor were causing the decrease in CCP, as turgor induced CCP decreases coincide with decreased GV volume.

In addition to a substantial decrease in CCP in response to BMAA treatment, an increase in the degree of colony formation was noted as compared to controls. Increased aggregation of buoyant cyanobacteria over the course of our environmental time series, and prior to its senescence, was also noted. In HAB states, increased colony size provides a number of benefits, as it allows for more rapid vertical migration during diel vertical migration (DVM) cycles.

When we compare nutrient shifts from our environmental time series to the change in PST, we see that the largest increase in PST coincided with growth limiting nitrate and phosphate concentrations—based on surface-grab samples—suggesting that cells were successfully migrating to thermocline boundary layers for nutrient resupply and sustained GV synthesis, and/or reallocating internal protein reserves (i.e. phycobilins) for continued GV synthesis. Coinciding with the period of greatest nutrient limitation, we also observed maximal pheophytin concentrations, as would be expected in phytoplankton populations experiencing resource competition in concert with photooxidative stress. Further enhancing nutrient

competition within the surface mixed layer and concurrent to the period of greatest nutrient limitation, increases in the depth of the seasonal thermocline boundary layer were observed.

Correlated with increased nutrient stress, thermocline depth, and BMAA concentration, the CCP distribution of the buoyant populations—as determined from pressure nephelometry measurements—underwent large shifts, resulting in decreased CCP across all populations and coinciding with the peak measured BMAA concentration of 58.1 ±2.7 ng g^{-1} lyophilized material. As CCP, as determined via pressure nephelometry, is species-specific and constant during periods of balanced growth, the decrease in CCP across all populations indicates that the mechanism of CCP decrease due to BMAA is likely conserved within the gas vacuolate cyanobacterial population. Subsequent to the peak in BMAA concentration, there was an almost complete loss of the PST signal at pressure below 155 kPa, which had been the dominant pressure-sensitive population. The hydrostatic pressure due to depth at the upper bounds of the thermocline boundary layer during the BMAA maxima was approx. 120 kPa at 12 m. Combined with the laboratory culture findings, the decrease in CCP due to BMAA is proposed to have resulted in cells with GVs unable to withstand the hydrostatic pressure they were subjected to during DVMs, leading to collapse of their GVs at depth, and resulting in their removal from the buoyant population. Further, following the decrease in CCP across populations, BMAA concentrations decreased to levels below the method detection limit (LLOQ=23 ng g^{-1} lyophilized material), and based on the population-wide PST signal, the BMAA decrease coincided with collapse of the bloom state. Principal component analysis of the physicochemical parameters recorded during the time series indicates that changes in BMAA concentration were most strongly correlated with pheophytin concentration, the depth of the thermocline boundary layer, and the size of the PST signal—indicating a role in stress responses, as has previously

been reported, and here attributed to buoyancy modulation in gas vacuolate, freshwater cyanobacteria.

6.2 Challenges and limitations

Throughout the completion of this work there were a host a challenges. Derivatization conditions for the HPLC-MS/MS method for total BMAA were found to be insufficiently alkaline to facilitate complete derivatization of target compounds, which resulted in multiple sets of samples that had undergone complete sample workup and could not be quantified, due to variability in the SIL internal standard and standard curve quantification transitions. Further compounding the initial derivatization condition issues, and due to conditions that occur during workup for total BMAA, hydrogen/deuterium (H/D) exchange with the initial deuterated SIL internal standard is thought to have been an issue. As we were utilizing a data-dependent acquisition method for MS/MS quantification, H/D exchange would result in increased variability and decreased concentration of the SIL standard—as was shown to be the case. Following this realization, the OHSU Medicinal Chemistry Core was kind enough to synthesize a ^{15}N-labeled BMAA SIL standard at our request, which resolved variability issues and resulted in an order-of-magnitude increase in the area of the SIL standard quantification transition.

In regards to the pressure nephelometer, over the course of its design and development, I was required to develop a suite of electrical engineering or programming skills. I was able to perform all system design, fabrication, and integration; following many frustrating hours perusing electrical engineering resources and learning how to solder and assemble integrated circuits. This challenging endeavor resulted in the acquisition of a number of skills, and exposure to a diverse array of subject matters that I would have never otherwise needed to explore, including: computer programming, optoelectronics, machining and fabrication, file structure and

systems architecture—to name just a few. Over the course of 2017 and 2018, I collected, recorded, and processed over 65,000 nephelometric turbidity spectra, which would have been impossible had the pressure nephelometer and subsequent data analysis not been automated via a suite of programs.

Sampling for the Ross Island Lagoon time series, including depth casts, was conducted largely by canoe.

There were also a number of limitations. The hypothesis that BMAA was involved in buoyancy modulation in cyanobacteria arose before deciding to construct the pressure nephelometer. While the development of the nephelometer enhanced my skill set and resulted in a number of interesting findings, had it been a commercially available item more time would have been available to delve into the underpinnings of ecophysiological responses to BMAA we observed. Likewise, further molecular and genetic characterization of the samples and sites would have been at the top of the list of priorities.

6.3 Future directions

In early 2018 I was awarded a travel grant to attend a MS-proteomics workshop hosted by the SkyLine development team in response to a proposal similar to the following.

In both bio- and synthetic oligopeptides, transpeptidation via enzyme-mediated and spontaneous intramolecular processes has been known to occur, whereby transpeptidation is achieved through nucleophilic attack of a side-chain amino group on the N-carbonyl of the peptide linkage (Blodgett & Loudon, 1989; Pfammatter & Seebach, 1991; Wang & Gould, 1993; Seebach et al., 1994). Blodgett and Loudon (1989) succinctly demonstrated that spontaneous formation of isopeptide species is strongly catalyzed by bicarbonate buffering systems, with the formation of the isopeptide being pH dependent, as the side-chain amino group must be

deprotonated in order to act as a nucleophile. Seebach et al., (1994) observed that a small synthetic ogliopeptide containing an α,β-diamino-containing amino acid in the central position was completely converted to the corresponding isopeptide within 24 hours of treatment with base, and that the transpeptide was stable for prolonged periods but reverted to a native state under more acidic conditions.

Within gas vacuolate cyanobacteria GVs can account for up to 10% of the total protein complement, which is a startling concentration of functional β-amyloid protein, as gas vacuolate cells must possess a means of recycling GvpA monomers and preventing the irreversible aggregation of amyloid plaques (Walsby, 1994). The cyclic rearrangement of BMAA via an isoaspartate-like intermediate has been proposed and is known to occur in similar α,β-diamino-containing amino acids, with spontaneous isopeptide formation being strongly catalyzed by bicarbonate in a pH dependent fashion; conditions that occur under dense HAB states when cyanobacterial carbon concentrating mechanisms are fully induced (Blodgett & Loudon, 1989; Karle et al., 1991; Woodger et al., 2005; Downing & Downing, 2016). Spontaneous reversal of isopeptide species has also been demonstrated, where the isopeptide is stable for prolonged periods but reverts to a native state under more acidic conditions, as would occur within cells undergoing DVMs and distinct photosynthetic/respiratory cycles (Seebach et al., 1994; Badger et al., 2008). Reversal of α,β-diamino-containing amino acids to a native state via a cyclic intermediate has also been shown to act as a "β-breaker" element, allowing for the disruption of insoluble β-sheet aggregates; in this case proposed to allow collapsed GVs to be recycled via dispersal of the aggregated GvpA monomers (Nadimpally et al., 2014). This type of cycle receives further support from isotope labeling studies in *Anabaena flos-aquae* CCAP 1304/13*f*, which did not provide a mechanism but indicated that collapsed GVs are dispersed and that the

constituent GvpA monomers are reassembled into growing GVs, as opposed to being degraded (Hayes & Walsby, 1984). If BMAA is being produced as a breakdown product, with elevated concentrations generated in response to environmental stressors associated with nutrient limitation concurrent to strong UVR exposure, this would also act as a temporal control on buoyancy regulation and account for the increased relative GV content in BMAA treated cultures. Where if the stressors were removed and BMAA production decreased, continued GV growth would dilute the CCP effect and cells would return to a baseline, while continued production of the compound would continue to amplify the attenuation of CCP and result in faster buoyancy reversal, while limiting UVR exposure and nutrient stress.

Support for a BMAA role in the cellular regulation of amyloid β-proteins (Aβ) is also given by pharmacological studies. The equilibrium dynamics of BMAA-carbamate adducts have recently been implicated as important contributors to the endogenous function of the compound in cyanobacteria, and may be key aspects of the human neurodegenerative diseases associated with prolonged BMAA exposure (Downing & Downing, 2016). The primary human metabolite of the commonly prescribed, non-centrally acting angiotensin converting enzyme (ACE) inhibitor, imidapril, is the cyclic BMAA carbamate adduct (cycBMAA), 1-methyl-2oxoimidazolidine-4-carboxylic acid (Matsuoka et al., 1992). Moreover, human genetic data indicates a strong correlation between ACE and AD, and in vitro studies using ACE cloned from human neuroblastoma cells have demonstrated that it is able to degrade naturally secreted Aβ40 and Aβ42, with ACE inhibition—as results from cycBMAA—leading to increased accumulation of Aβ plaques in the media of Aβ precursor-protein expressing cells (Hemming & Selkoe, 2005).

Due to the insoluble nature of GvpA monomers, determination of structural elements via x-ray crystallography has to date been impossible. However, intact GVs can be isolated from

lysed cells and targeted proteomics of intact GVs with a labeling scheme similar to terminal-amine isotopic labeling of substrates (TAILS) and/or isobaric tag for relative and absolute quantitation (iTRAQ) has been identified as a means of addressing the above postulate, and would take advantage of the large disparity in the nucleophilicity of the BMAA amines. Such that if BMAA were associating with GvpA monomers, and if transpeptidation were occurring, labeling of the isopeptide-generated primary amine would be possible at near-physiological pH values, with resolution of the associated site being possible through protein MS.

7. Appendix A: Cyanobacteria metabolism and metabolite review

7.1 Carbon and Environmental Fluxes

7.1.1 Introduction of carbon into aquatic systems

Atmospheric carbon dioxide (CO_2) levels have continued to rise since the industrial revolution, due largely to increasing carbon intensity from anthropogenic emissions coupled to a decline in the efficiency of terrestrial and acquatic CO_2 sinks (Canadell et al., 2007). Henry's Law is generally used as the framework for rationalizing diffusive fluxes between gaseous and liquid states, with convention indicating that the dissolved concentration of a gas be based on the partial pressure of said gas in the space above the solvating liquid, as represented in the following equation:

1

$$C_x = K_H(p_x)$$

Where C_x denotes the dissolved concentration of gas *x*, K_H is the Henry's Law solubility constant, and p_x is the partial pressure of gas *x* in equilibrium with the solvating fluid. In the case of the Earth's aquatic systems care must be taken when considering the flux of CO_2 between aquatic systems and the atmosphere. When CO_2 is hydrolyzed, a kinetically slow reaction takes place to yield carbonic acid. Carbonic acid then undergoes a series of deprotonation reactions, yielding bicarbonate and carbonate anions, summarized in the following equation:

2

$$CO_2 + H_2O \leftrightarrow H_2CO_3 \leftrightarrow H^+ + HCO_3^- \leftrightarrow 2H^+ + CO_3^{2-}$$

The interconversion and equilibrium reactions between the various dissolved forms of CO_2 act as a pH buffering system, such that the dissolved concentration of Ci becomes the main determinant of pH in most aquatic systems. As the equilibrium vapor pressure of CO_2 is unaffected by the concentration of its charged derivatives, the total dissolved inorganic carbon content of aqueous systems will greatly exceed—except at the extremes of pH—the concentration of gaseous CO_2 as predicted by Henry's Law. Building on our considerations of partial pressure and CO_2 speciation, it becomes clear that the dissolved inorganic carbon content of Earth's sea-surfaces controls the atmospheric concentration of CO_2. Thus, the observed increase in atmospheric CO_2 over the last few centuries is just the tip of the iceberg; total dissolved inorganic carbon concentrations are increasing exponentially, and opportunistic microbes are taking note.

7.1.2 Carbon metabolism and eutrophication

In spite of exponential increases in the concentration of dissolved free inorganic carbon (Ci: HCO_3^- and CO_2) available to aquatic photoautotrophs, Liebig limitation due to [Ci]—especially in eutrophic waters—often controls the proliferation and speciation of phytoplankton assemblages (Ibelings and Maberly, 1998; Dervaux et al., 2015; Van de Waal et al., 2011). The Squaw Lake Basin experiments demonstrated that the annual formation of cyanobacterial climax communities occurs irrespective of large deviations in the dissolved Ci concentration, or resultant pH, while in prior experiments, comparisons between [Ci] and photosynthetic efficiency had been based on cultures smaller than 1-2 m^3. Validating the critique of King's hypothesis (King, 1970) put forth by Talling, (1976), the large differences in pH and [Ci] between the control, and CO_2-enriched lakes had little effect on the population dynamics, with

cyanobacteria becoming dominant in both lakes at approximately the same time and reaching the same total and relative abundances.

Alternately, the Squaw lake experiments served to verify the second part of King's hypothesis (King, 1970), demonstrating that the prevalence of cyanobacteria, especially in eutrophic waters with elevated pH, results from their very favorable CO_2 kinetics, allowing growth to continue past the CO_2 compensation point of other phytoplankton. In fact, the rate of Ci acquisition in the *flos-aquae* strains analyzed was sufficiently rapid to elicit diffusion limitations for CO_2, with cell-specific radiocarbon uptake decreasing markedly when colonies were dissociated into trichomes by disrupting the cell-to-cell adhesion provided by anionic EPS matrix interactions. Based on these considerations and supported by experimental observations, under specific conditions cyanobacteria benefit greatly from being as close to the surface of the water as possible, as the rate of diffusion of CO_2 in air is approximately five orders of magnitude more rapid than the rate of diffusion in water.

7.2 Carbon Concentrating Mechanisms in Cyanobacteria

7.2.1 Background

How have cyanobacteria eschewed the Ci limitations that occur in blooms? Through the evolution of various adaptations that coalesce to form a highly functional CO_2-concentrating-mechanism (CCM), resulting in a CO_2 compensation point that provides an intense selective advantage over green algae under carbon limiting conditions. The Squaw Lake basin experiments demonstrated, on a massive scale, that highly variable CO_2 concentrations had little effect on phytoplankton population dynamics until cyanobacterial populations reached a threshold, at which point cyanobacterial CCMs diminished the free carbon concentration to a level far below the CO_2 compensation point of other aquatic photoautotrophs (Shapiro, 1997).

The CCM is an active system of diverse transporters that accumulate Ci in cyanobacterial-specific, proteinaceous micro-compartments (carboxysomes). Sequestered within the carboxysomes, Rubisco is protected from photorespiration, and the active transport and accumulation of Ci in the carboxysome negates some of the rate retardation Ci binding to Rubisco inflicts on the Calvin-Benson-Bassham (CBB) Cycle. While convergent evolution has resulted in cyanobacterial carboxysomes that are ultrastructurally equivalent, as well as Rubisco variants possessing the same large subunit motif (L8S8) and catalytic function, further analysis allows us to divide cyanobacteria into two major groups based on the evolutionary lineage of their CCM components. Reviewed extensively elsewhere (Bek & Badger, 2008; Whitney et al., 2011), Form 1 Rubisco (L8S8 large subunit) can be phylogenetically subdivided into Form 1A or 1B, associated with α-cyanobacteria and β-cyanobacteria, respectively. Marine cyanobacteria chiefly contain Form 1A Rubisco, while freshwater taxa are almost exclusively β-cyanobacteria, possessing Form 1B Rubisco (Delwiche and Palmer, 1996; Watson & Tabita, 1999). In similar fashion, proteomic studies have shown that α-carboxysomes, found in α-cyanobacteria possessing Form 1A Rubisco, evolved independently of β-carboxysomes, found in β-cyanobacteria possessing Form 1B Rubisco (Badger et al., 2002). While such nitpicking nomenclature is at times only useful from a semantics perspective, in the case of Rubisco the various forms are quite distinct, and possess kinetic properties tailored to specific microbial niches. The ubiquitous presence of Rubisco—arguably the most abundant protein in the world (Ellis, 1979)—is rather remarkable, as Rubisco is a very poor catalyst. Responsible for the rate limiting reaction in carbon fixation, Rubisco possesses poor substrate specificity, poor substrate affinity, and an abysmally low turnover rate based on the carbon compensation point of photoautotrophs. Despite the apparent pitfalls of a Rubisco-dependent photoautotrophic lifestyle,

aquatic cyanobacteria account for >25% of global net primary production, with the metabolic malleability afforded by a diverse range of cyanobacterial CCMs playing a substantial role in their proliferation and evolutionary success.

7.2.2 Evolution of cyanobacterial CCMs

Kaneko et al., (2007) found that a total of 688 kb of the genome of *M. aeruginosa* NIES-843 (representing some 11.8% of the entire genome) is occupied by insertion sequences (ISs) and miniature inverted-repeat transposable elements (MITEs). The abundance of mobile repetitive elements results in a genome that is highly malleable, lending credence to the postulate that the ubiquitous presence of CCMs in modern cyanobacteria resulted from a rapid evolutionary event some 350 million years ago (mya), and was aided in part by the lateral transfer of large gene sets (Price et al., 2008). A marked decrease in atmospheric CO_2 during the late Devonian and early Carboniferous periods, in conjunction with rising oxygen levels, would have provided the evolutionary pressure for the appearance of CCMs, as photorespiration and the resulting decrease in photosynthate production would have necessitated that phytoplankton adapt, or migrate—a hard order for epipelagic phytoplankton restricted to diel vertical migrations (Walsby, 1994; Brookes and Ganf, 2001; Bhaya, 2004). The presence of cyanobacterial carboxysomes and negligible photorespiration also result in a higher nitrogen use efficiency. And despite the additional metabolic costs associated with active capture and mobilization of Ci—the accumulation and catabolism of photosynthate represents the largest nutrient flux cyanobacteria experience—it is easy to demonstrate the competitive advantages cyanobacteria gain from CCMs. The rate of photosynthate production is able to reach saturation at exogeneous CO_2 concentrations an order of magnitude lower than the Michaelis constant for CO_2 binding to Rubisco (Km > 150 µM CO_2) (Badger and Andrews, 1998; Falkowski and Raven, 2007).

7.2.3 Classification and framework of cyanobacterial CCMs

The CCMs of cyanobacteria contain a number of basic operational motifs: (i) active pumps for the acquisition of Ci; (ii) an energy source for the Ci pumps in the form of NTPs, high-energy electron donors, or electrochemically mediated cotransport; (iii) maintenance of HCO_3^- in disequilibrium against CO_2 through a lack of cytosolic-carbonic anhydrase activity (ionic forms of Ci are orders of magnitude less permeable to lipid membranes than their uncharged counterparts, allowing cyanobacteria to regularly generate peak Ci pools of up to 40 mM); (iv) systems for maintaining internal pH homeostasis; (v) generation of elevated CO_2 levels within the Rubisco-containing carboxysomes; (vi) carboxysome-localized carbonic anhydrase (CA) with catalytic turn-over closely matching the maximal rate of photosynthate production; (vii) prevention of CO_2 leakage from the carboxysomes; (viii) if leakage does occur, a means of recycling the errant CO_2 before it can escape from the cell; and (ix) deviation from a constitutive level of CCM activity through transcriptional and allosteric regulation of transporters and carboxysome components in response to exogenous Ci fluxes.

7.2.4 Constitutively expressed CO_2 uptake systems of the CCM

Analysis of the complete cyanobacterial genomes assembled to date indicates that, for both α- and β-cyanobacteria, CCM-associated Ci uptake is dependent on a limited number of highly conserved transport systems. As demonstrated by Wei et al., (1994), even in cultures subjected to hyper-normal CO_2 concentrations via vigorous aeration, a fully-functional basal state of the CCM is present, with cells actively accumulating both CO_2 and HCO_3^-. In this basal state, a specialized, plasma membrane-associated NAD(P)H dehydrogenase (NDH-I_4)—typified by and first identified in the freshwater β-cyanobacteria *Synechocystis* PCC 6803—is constitutively expressed (Ohkawa et al., 2000; Shibata et at., 2001). Separate efforts from the

Price and Ogawa laboratories resulted in the conclusion that the gene products of *ndhF4/ndhD4/chpX* comprise the NDH-I_4, low-affinity CO_2 uptake complex (Shibata et al., 2001; Maeda et al., 2002). The CO2 hydration proteins ChpX and ChpY, identified by Maeda et al., (2002) are analogous to those presented by Shibata et al., (2001) as CupA and CupB, respectively. While the NDH-I_4-associated complex functions as a CO_2 uptake system, it should be noted that the process does not rely on active transport of CO_2. Rather, passive diffusion of CO_2 into the cell is linked to its vectoral conversion to HCO_3^- within the cytoplasm, thereby establishing a form of active facilitated uptake that takes advantage of Le Chatelier's principle to increase the rate of CO_2 diffusion into the cell. This mechanism is still speculative, as nucleotide and protein queries indicate that the Chp/Cup proteins are distinct from the known cyanobacterial carbonic anhydrases (CA). However, multiple alignment studies of Chp/Cup proteins, from both α- and β-cyanobacteria, have identified a number of conserved histidine and serine residues capable of ligating Zn in a coordination site similar to that of traditional CA enzymes (Maeda et al., 2002; Price et al., 2008). Based on the assumption that Zn does coordinate to these residues in Chp/Cup proteins, the generation of a zinc-bound reactive hydroxyl (Zn-OH°) capable of nucleophilic attack on CO_2 is quite feasible—as has been proposed for traditional CA enzymes (Smith et al., 2000). Generation of the Zn-OH° species requires abstraction of a proton from water to a nearby amphoteric residue (presumably one of the Zn-ligating histidine residues), with subsequent transfer of the proton to a base in the complex that is generated through reduction by NAD(P)H or ferredoxin. A key feature of this mode of CO_2-uptake, which is essential for maintaining the disequilibrium between CO_2/HCO_3^-, is the redox-driven translocation of protons into a luminal space, resulting in a net reaction that is functionally irreversible in illuminated cells. While this mechanism requires additional

validation, and specification as to where the Chp/Cup proteins interact with the larger NDH-1 complex, the lack of a traditional cytosolic carbonic anhydrase, and negligible concentrations of CO_2 in the cytoplasm of cyanobacteria indicates that the general schemata is sound (Badger and Price, 2003).

It is interesting to note that the activities of NMDA and AMPA glutamate receptor and ion channel proteins are zinc dependent, and that BMAA-zinc coordination complexes are far more stable than the corresponding Glutamate-zinc complexes. Moreover, apart from histidine which forms coordination complexes with zinc and copper of similar stability to the corresponding BMAA complexes, BMAA is one of the few biosynthetic amino acids able to form stable 5- and 6-membered chelating rings through the α-amino group (Peters et al., 1987; Nunn et al., 1989; Glover et al., 2012). As the stereochemistry and coordination geometry of Zn/Cu-BMAA/His complexes are markedly different, and multiple protein and regulatory systems that are responsive to BMAA rely on cationic—zinc and other divalent cations in particular—cofactors ligated by histidine residues within the protein active sites (as well as glutamate or 2OG cofactors in many cases), it is entirely feasible that BMAA is acting as an unintended effector molecule on ionotropic and/or metabotropic transmembrane channels, or other similar regulatory systems. This hypothesis is bolstered by recent research from Liu et al., (2009), which indicated that in mammalian cells, BMAA acts directly on NMDA receptors in addition to activating the metabotropic glutamate receptor 5 (mGluR5), resulting in enhanced oxidative stress. Modulation in the activity and function of mGluR via glutamate binding is also involved in the regulation of protein kinase activity and Ca^{2+} release form intercellular stores (Xiao et al., 2006).

7.2.5 Constitutively expressed HCO_3^- uptake systems of the CCM

Building on the suggestion put forth by Espie and Kandasamy, (1994) that cyanobacteria possessed a constitutively expressed Na^+/HCO_3^- symporter, Shibata et al., (2002) were able to demonstrate that HCO_3- uptake via SbtA is Na^+-dependent, requiring approximately 1 mM Na^+ to achieve half-saturation for HCO_3^- uptake activity. The maximal activity of the NDH-I_4 complex remains stable during Ci stepdown and limitation, while proteomic analysis indicates that SbtA undergoes a marked increase in biosynthesis under Ci limitation (Zhang et al., 2004). This proteomic study also indicated that the functional SbtA transporter is a transmembrane homotetramer of approximately 160 kDa, with multiple cytoplasmic domains possessing helix-turn-helix (HTH) motifs. So far unabridged, it has been postulated that fast-induction of the high-affinity SbtA transporter under Ci limitation results from allosteric regulation via phosphorylation of one or more residues located on the cytoplasmic face of the SbtA HTHs via a serine-threonine protein kinase (Sultemeyer et al., 1998). Support for this mechanism of fast-induction comes from *Synechococcus* sp. PCC7002 cultures treated with known protein kinase inhibitors (K252a, staurosporine, or genistein). When culture samples were transitioned from a high CO_2 media to a low-CO_2 buffer containing a CA, no change in the rate of HCO_3^- uptake was observed for the protein kinase inhibitor-treated samples. Fast-induction of the high-affinity HCO_3^- transporters was also dependent on the Na^+ concentration of the media, further supporting posttranslational phosphorylation of SbtA as one mechanism of CCM regulation in response to Ci limitation (Amoroso et al., 2003).

7.2.6 Inducible Ci uptake systems

Apart from the constitutively expressed CCM genes coding for carboxysome components and low-affinity/high-flux Ci uptake systems, cyanobacteria possess a number of inducible, high-affinity/low-flux Ci uptake systems. Particularly abundant in β-cyanobacteria—due to exposure

to a broader range of, and more frequent limitations in, Ci concentration than α-cyanobacteria—these inducible, high-affinity Ci uptake systems are typified by the thylakoid membrane-associated CO_2 uptake facilitator NDH-I_3, as well as the plasma membrane-associated HCO_3^- transporters SbtA, BCT1, and BicA.

In addition to the constitutively expressed CO_2 transporter NDH-I_4, an inducible, high-affinity NDH-I-type complex (NDH-I_3) has been identified in all but one of the β-cyanobacteria examined to date, but is conspicuously absent from α-cyanobacteria with the exception of *Synechococcus* WH5701, which appears to possess a full complement of the known Ci-uptake systems (Price et al., 2008). The CO_2 transport activity of NDH-I_3 was originally attributed to the known NDH-1 complex responsible for cyclic electron flow within the photosynthetic electron transport chain (ETC) (Ogawa, 1992). However, genomic analysis of prototypical β-cyanobacteria identifies multiple gene copies of NDH-1 constituents, namely *ndhD* and *ndhF*, the products of which share little homology with their respective cohorts. Unsurprising based on the existence of multiple *ndhD/F* gene copies, phenomic support for the existence of a discrete high-affinity NDH-1 CO_2 transporter was garnered by the finding that the gene cluster *ndhF3/ndhD3/chpY/orf135* is necessary for the induction of high-affinity CO_2 uptake (Shibata et al., 2001). Moreover, proteomic analysis of crude thylakoid membrane fractions from wild-type and specific *ndh* gene knockout mutants of *Synechocystis* PCC6803 grown under varying CO_2 and pH regimes served to disambiguate NDH-I_4 from NDH-I_3, in addition to providing evidence for the cellular localization of the ndhF3/ndhD3/chpY/sll1735 complex within the thylakoid membrane (Zhang et al., 2004). While NDH-I_3 is distinct from the photosynthetic NDH-1 complexes, its localization within the thylakoid membrane is noteworthy and will be discussed in later sections.

Unique among the inducible Ci transporters, the plasma membrane-associated BCT1 complex is the only primary transporter for HCO_3^- uptake thus far identified in cyanobacteria, and functions as a traffic ATPase, characterized by the ATP binding cassette (ABC) transporter family (Omata et al., 1999). A number of excellent and exhaustive reviews focusing on the structure, function and regulation of traffic ATPases have been previously compiled (Higgins, 1992; Davidson et al., 2008). First characterized in *Synechococcus* PCC7942, close homologs of the BCT1 operon *cmpABCD* have been found in a number of cyanobacteria, and while thorough investigation of the function of these homologs is lacking they appear to act as HCO_3^- transport ATPases. Multiple alignment analysis using the cyanobase database also indicates that very close homologs of the substrate-binding protein CmpA exist in multiple *Synechococcus* sp. strains, and belong the nitrate/nitrite/cyanate ABC transporter (NitT) family (Allewalt et al., 2006). Other standouts with an appreciable degree of homology to CmpA include: (i) the Holliday junction DNA helicase *ruvA* in *Synechococcus* CC9605, (ii) a possible TIR-domain containing protein in *Prochlorococcus* sp. MIT9301, (iii) glycerol-3-phosphate dehydrogenase (GPDH) in *Synechococcus* sp RCC307 (GPDH is thought to maintain the redox potential across the mitochondrial inner membrane in glycolysis), (iv) a carboxyl-terminal processing protease in *Prochlorococcus* sp. MIT9303 (see Chapters 2/5 herein RE: ACE inhibition by BMAA), (v) a putative apolipoprotein n-acetyltransferase in *Prochlorococcus* sp. MIT9211, (vi) histidinol-phosphate aminotransferase in multiple *Synechococcus* sp. and *Prochlorococcus* sp. strains, (vii) as well as a number of glycosyl- and acyltransferases. Of the CmpA homologs mentioned, NitT and GPDH are of particular interest as GPDH serves as a link between lipid and carbohydrate metabolism, and NitT-type permeases often transport amines that arise from the decarboxylation of amino acids and their methylated derivatives, as well as nonproteogenic peptide-like

molecules synthesized by non-ribosomal peptide synthetases; similar metabolic roles and compound transformations have been reported for BMAA (Saier, 2000; Downing & Downing, 2016).

In addition to the constitutively expressed SbtA transporter, a number of α- and β-cyanobacteria possess a second inducible, Na^+-dependent HCO_3^- transporter. Originally reported by Kaneko et al., (1996) as ORF sll0834 in the freshwater cyanobacterium *Synechocystis* PCC6803, and classified as a low affinity sulfate transporter, it would be almost a decade before Price et al., (2004) demonstrated that the analogous gene product of *Synechococcus* PCC7002 functioned as an inducible HCO_3^- transporter. This ambiguity is unsurprising as BicA belongs to the broader sulfate permease (SulP/SLC26A) family and possesses many of the structural features found in other SulP-type anion transporters, most notably a cytoplasmic carboxy-terminal segment that contains a sulfate transporter and anti-sigma factor antagonist (STAS) domain, as well as a cytoplasmic loop between helices eight and nine that contains a highly conserved motif characteristic of the SulP family (Shelden et al., 2010). While the SulP family of anion transporters is highly conserved in organisms ranging from microbes to manatees, the functional roles of the STAS domains are highly variable and include: stimulation of bacterial RNA polymerase, derepression of inhibitory antisigma kinases, histidine and serine/threonine kinase activity, nucleotidase activity, as well as roles in sensory transduction and transport of nutrients such as amino acids, lipids, hydrocarbons, and vitamins (Sharma et al., 2011). Additionally, for other STAS domain-containing proteins, stress from temperature, pH, blue light, and osmolarity can all trigger a signaling cascade involving STAS regulation of RNA polymerase as part of a 'stressosome' system (Jurk et al., 2011). Recent work by Babu et al., (2010) demonstrated that bacterial YchM, another SulP family member, binds acyl carrier

protein (ACP) at the STAS domain in a 1:1 stoichiometry, and it was suggested that HCO_3^- taken up by YchM is channeled directly to a fatty acid biosynthesis complex localized at or near the cytoplasmic face of Ychm. If valid, this type of directed nutrient uptake for synthetic purposes indicates that the bacterial Ci uptake systems may serve a more substantial role in bacterial metabolons than is currently acknowledged.

7.2.7 Regulation of CO_2-responsive Ci transporters

Particularly for marine and euryhaline cyanobacterial species, there exists a dearth of evidence detailing the signaling cascade associated with CCM up-regulation under Ci-limiting conditions. But, various findings indicate an inverse relationship between expression of Ci-responsive genes and the size of intracellular Ci pools, as well as a dependence on oxygen for complete induction of CCM components under Ci limitation (Woodger et al., 2005). It is also acknowledged that Ci uptake is inactive in the dark (Price et al., 2008). For the β-cyanobacteria typified by *Synechocystis* PCC6803 and *Synechococcus* PCC7002, a more complete regulatory system has been identified, with both activation and repression of high-affinity CCM transporter genes occurring through interaction with one or more of the LysR-type transcriptional regulators (LTTRs) CcmR (see also: NdhR) and CmpR (Figge et al., 2001; Omata et al., 2001; Woodger et al., 2007). Within the broader LysR family a number of subfamilies have been established, with CcmR and CmpR falling under the proteobacterial CBB-cycle regulator category, typified by CbbR (Schell, 1993). Genome comparison utilizing the cyanobase database indicates that homologs of RbcR, another CbbR subfamily member, are present in all cyanobacterial genomes to date. Figge et al., (2001) and others have postulated that RbcR may regulate transcription of the constitutive CCM genes, but enumeration of the complete list of genes under RbcR control is stymied by the lethal phenotype that results from many of the CCM loss-of-function mutants.

Evidence from recent surface plasmon resonance (SPR) analysis indicates that 2OG and $NADP^+$ act as co-repressors in conjunction with CcmR, while ribulose-1,5-bisphosphate (RuBP) and 2-phosphoglycolate (2PG) were indicated as co-activators of CmpR—the transcriptional regulator of the ABC-type HCO_3^- transporter BCT1 (Daley et al., 2012). This finding substantiates the proposal by Woodger et al., (2007) that CcmR acts as a negative transcriptional regulator for all CO_2-responsive genes identified to date in *Synechococcus* sp. PCC7002—making it highly likely that regulation of Ci accumulation occurs through homologous systems in other β-cyanobacteria. Identification of 2OG as a specific CcmR co-repressor is exciting, as previous work by Hisbergues et al., (1999), utilizing PII (*glnB*) null mutants, speculated that nitrogen status—in conjunction with intracellular Ci concentrations and cellular redox state—could act as a signal in the regulation of CO_2-responsive genes.

In light of these findings, it is interesting to note that formation of a cyclic carbamate adduct of BMAA (cycBMAA) occurs spontaneously under conditions of elevated O_2 and pH, and has been shown to strongly inhibit LysR-family regulators (Matsuoka et al., 1992; Hemming & Selkoe, 2005; Downing & Downing, 2016). As multiple instances of LysR-type transcriptional regulators responding directly to small effector molecules have been reported (Schell, 1993), and BMAA has been shown to act on nitrogen regulatory systems responsive to 2OG, in addition to being produced under nitrogen starvation and eliciting massive glycogen accumulation, it is entirely plausible that BMAA competes with 2OG for binding sites in regulatory systems; or has been shown for other non-ribosomally synthesized peptides, disrupts the activity of regulatory phosphatases and kinases (Kamberov et al., 1995; Downing et al., 2011; Downing et al., 2012; Berntzon et al., 2013; Kaplan et al., 2012; Price et al., 2008; Babu et al., 2010).

7.3 Toxic Cyanobacterial Metabolites: Prevalence, Synthesis, and Environmental Drivers

7.3.1 Background

Despite their evolutionary importance as the progenitor of photosynthesis and their modern day importance to global biogeochemical cycling, many aspects of cyanobacterial metabolism and cellular life remain obscure; this is especially true for the diverse array of cyanotoxins that cyanobacteria produce. These pharmacologically active compounds were historically assumed to be secondary metabolites, but with recent omics advances and the development of annotated databases for cyanobacterial genome and metabolome exploration, it is becoming increasingly clear that many cyanotoxins have endogenous regulatory effects and are likely involved in both intra- and inter-species communication (Zimmer & Ferrer, 2007; Downing & Downing, 2016). Moreover, as the genera associated with cyanotoxin production are generally responsible for the formation of cyanoHABs, the development of a greater understanding of the ecophysiological drivers of toxin production is tantamount to mitigating threats to human populations (Cox et al., 2005; Strucken et al., 2010; Rantala-Tlinen et al., 2011).

Within the cyanotoxin umbrella, a first tier of compound classifications can be made on the basis of chemical similarity, resulting in groupings for peptide-, alkaloid-, lipopeptide-, and modified amino-based compounds, which can further be distinguished by the specific non-ribosomal peptide synthetase (NRPS)/polyketide synthatase (PKS) systems employed for synthesis.

7.3.2 Modified Ogliopeptide Cyanotoxins

7.3.2a Microcystin

The microcystins represent the most structurally diverse, and most well studied, class of cyanotoxins. These mixed NRPS/PKS derived compounds are based on a cyclic heptapeptide core, with varying degrees of hydroxylation, methylation, and tail-peptide-sequence giving rise to the more than 90 microcystin isoforms thus far isolated from various genera, including *Microcystis*, *Anabaena*, and *Planktothrix* (Welker and von Dohren, 2006; Steffen et al., 2015). While the microcystins vary in their degree of toxicity, they are uniformly hepatotoxic to humans, with ingestion being the dominant route of exposure and the observed hepatotoxic effects arising from protein phosphatase 1 and 2A inhibition, as is the case for the structurally related pentapeptide cyanotoxin, nodularin (Runnegar et al., 1995). While the microcystins have been shown to produce lethal effects in zooplankton, leading to the postulate that the compound evolved in response to grazing pressure from Metazoans, phylogenetic analysis comparing the divergence of the *myc* cluster to 16S rRNA and *rpoC1* signatures indicates that the *myc* genes were present in the last common ancestor of a large number of cyanobacteria; evolving in the late Archaean, far before the emergence of the earliest eukaryotic lineages (DeMott et al., 1991; Rantala et al., 2004; Rohrlack et al., 2013). The molecular characterization of the *myc* gene cluster, and the identification of a central, bidirectional promoter between *mycA and mycD* containing binding motifs for both the global nitrogen control (NtcA) and ferric uptake (Fur) transcriptional regulators are more indicative of a metabolic role for microcystin biosynthesis, with regulation occurring in response to nutrient (nitrogen/iron) and light (redox) stimuli (Martin-Luna et al., 2006; Ginn et al., 2010). With the latter receiving strong support from recent metabolomic studies (Meissner et al., 2015).

7.3.3 Alkaloid Cyanotoxins

7.3.3a Saxitoxin

Saxitoxin is recognized to be the most potent of the Paralytic Shellfish Toxins (PSTs) and has been deemed a "keystone metabolite" due to the pervasive and negative effects it elicits across multiple trophic levels (Zimmer & Ferrer, 2007). The PSTs differ from other cyanotoxin families in that they are also produced by certain eukaryotic dinoflagellates, and as has been proposed for other bioactive hydrophobic molecules within the phycosphere (e.g., AHLs), are thought to be involved in interkingdom signaling (Rumbaugh, 2007; Amin et al., 2012). The neurotoxic effects observed in vertebrates exposed to PSTs result from the inhibition of voltage-gated calcium, potassium, and sodium channels, with the degree of inhibition largely dependent on the strength of interaction between the C8 guanidinium ion of the PST and anionic groups within the outer ion-conduction pore of the voltage-gated channels affected (Strichartz, 1984).

7.3.3b Anatoxin

Prior to the compound being attributed to the cyanobacteria *Anabaena flos aquae*, anatoxin was known as very fast death factor (VFDF). First characterized by Peary and Gorham (1966) and shown to possess acute neurotoxic effects brought about by acetylcholinesterase inhibition, VFDF was later identified as one of the three anatoxin variants, which include the bicyclic, secondary alkaloid amines: anatoxin-a and homoanatoxin-a, as well as the cyclic, N-hydroxyguanidine containing alkaloid phosphoester, anatoxin-a(s). A biosynthetic route for the secondary amine derivatives was first presented by Méjean et al., (2009) with synthesis starting from proline adenylation as has been described for other biosynthetic pyrrole-containing secondary metabolites (Meiser et al., 2008). In agreement with the previous finding, while analyzing *Anabaena* sp. strain37 in an effort to develop genera identification tools based on restriction fragment length polymorphism analysis, Rantala-Ylinen et al., (2011) identified a highly homologous (81.6% to 89.2% based on nucleotide sequence) 29 kb DNA fragment that

contained the *anaA-G* gene cluster. However, operon organization differed between the two organisms, and the mode of regulation and potential transcriptional factors are, at present, assumed to be strain-specific.

7.3.3c Cylindrospermopsin

Joining the saxitoxin isoforms and anatoxin variants under the alkaloid toxin banner, the cylindrospermopsins are structurally characterized by a functional tricyclic guanidino group appended to a hydroxymethyluracil ring. The cylindrospermopsins deviate from the PSTs in that only two additional congeners have been identified (7-epicylindrospermopsin and 7-deoxycylindrospermopsin), and from both the PSTs and anatoxins in that 7-deoxycylindrospermosin is nontoxic; however, multiple studies have speculated that cylindrospermopsin biosynthesis proceeds via the hydroxylation of 7-deoxycylindrospermopsin as a precursor (Mihali et al., 2008; Mazmouz et al., 2010)

Cylindrospermopsin is a potent protein synthesis inhibitor that was originally isolated from *Cylindrospermopsis raciborskii*, and later identified as the causative agent of the endemic gastric distress that occurred on Palm Island, Australia in 1979 (Hawkins et al., 1985). However, it would take more than twenty years for Humpage et al., (2005) to elucidate the exact etiology of the hepatoenteritis that struck Palm Island, and attribute the acute nephrotoxic, hepatotoxic, cytotoxic, and genotoxic effects observed on Palm Island to cylindrospermopsin-derived, cytochrome p-450 (CYP450)-generated byproducts, indicating that the toxicity is predominantly enacted extracellularly. The genes for cylindrospermopsin synthesis (*cyr*) were first characterized in *C. raciborskii* AWT205 and later in *Oscillatoria* PCC6506, *Aphanizomenon sp.* 10E6, and various strains of *Raphidiopsis* (Shalev-Alon et al., 2008; Mazmouz et al., 2010; Soto-Liebe et al., 2010; Pierangelini, 2015).

7.3.4 Lipopeptide Cyanotoxins

7.3.4a Jamaicamide

Despite the astounding structural variability seen in the various cyanotoxins, the biosynthetic underpinnings are remarkably similar, with NRPS modules facilitating the condensation of amino acids and PKS modules extending and modifying compounds via the ligation of acetate building blocks. Further amendments to cyanotoxin structure are possible within mixed NRPS/PKS systems, with variability arising from multiple instances of oxidation, methylation, and halogenation—as is the case for the lipopeptide toxins, jamaicamideA-C, which contain both vinyl chloride and alkynyl bromide moities. As has been shown for other bioactive cyanobacterial metabolites (e.g. antillatoxin and kalkitoxin), the jamaicamides disrupt mammalian voltage-gated sodium channels, resulting in acute neuro- and cytotoxic effects (Manger et al., 1995). From stable isotope precursor feeding experiments in cultures of *Lyngbya majuscula*, Edwards et al., (2004) were able to identify a 58 kb gene cluster associated with the jamaicamide-A NRPS/PKS/mixed-synthetase system. This *jam* cluster contained 17 ORFs, where the predicted function of each gene product was shown to be collinear with the predicted synthetic route for jamaicamide-A, an exciting finding as NRPS/PKS systems and the atypical chemical structures they are able to produce are of great interest to the chemical synthesis and pharmaceutical industries.

6. References

1 Allen, M. M. & Stanier, R. Y. Growth and Division of Some Unicellular Blue-green Algae. *Microbiology* **51**, 199-202, doi:10.1099/00221287-51-2-199 (1968).

2 Allewalt, J. P., Bateson, M. M., Revsbech, N. P., Slack, K. & Ward, D. M. Effect of Temperature and Light on Growth of and Photosynthesis by Synechococcus Isolates Typical of Those Predominating in the Octopus Spring Microbial Mat Community of Yellowstone National Park. *Applied and Environmental Microbiology* **72**, 544-550, doi:10.1128/aem.72.1.544-550.2006 (2006).

3 Allison, E. M. & Walsby, A. E. The Role of Potassium in the Control of Turgor Pressure in a Gas-Vacuolate Blue-Green Alga. *Journal of Experimental Botany* **32**, 241-249, doi:10.1093/jxb/32.1.241 (1981).

4 Altermann, W. & Kazmierczak, J. Archean microfossils: a reappraisal of early life on Earth. *Res Microbiol* **154**, 611-617, doi:10.1016/j.resmic.2003.08.006 (2003).

5 Amin, S. A., Parker, M. S. & Armbrust, E. V. Interactions between diatoms and bacteria. *Microbiol Mol Biol Rev* **76**, 667-684, doi:10.1128/MMBR.00007-12 (2012).

6 Aminot, A., Kérouel, R. & Birot, D. A flow injection-fluorometric method for the determination of ammonium in fresh and saline waters with a view to in situ analyses. *Water Research* **35**, 1777-1785, doi:10.1016/S0043-1354(00)00429-2 (2001).

7 Amoroso, G., Seimetz, N. & Sültemeyer, D. The dc13 gene upstream of ictB is involved in rapid induction of the high affinity Na+ dependent HCO3− transporter in cyanobacteria. *Photosynthesis Research* **77**, 127, doi:10.1023/a:1025873718682 (2003).

8 Babu, M. *et al.* Structure of a SLC26 anion transporter STAS domain in complex with acyl carrier protein: implications for E. coli YchM in fatty acid metabolism. *Structure* **18**, 1450-1462, doi:10.1016/j.str.2010.08.015 (2010).

9 Badger, M. R. *et al.* The diversity and coevolution of Rubisco, plastids, pyrenoids, and chloroplast-based CO2-concentrating mechanisms in algae. *Canadian Journal of Botany* **76**, 1052-1071, doi:10.1139/b98-074 (1998).

10 Badger, M. R. & Price, G. D. CO2 concentrating mechanisms in cyanobacteria: molecular components, their diversity and evolution. *Journal of Experimental Botany* **54**, 609-622 (2003).

11 Banack, S. A. & Cox, P. A. Biomagnification of cycad neurotoxins in flying foxes. *Implications for ALS-PDC in Guam* **61**, 387-389, doi:10.1212/01.wnl.0000078320.18564.9f (2003).

12 Beard, S. J., Hayes, P. K., Pfeifer, F. & Walsby, A. E. The sequence of the major gas vesicle protein, GvpA, influences the width and strength of halobacterial gas vesicles. *FEMS Microbiology Letters* **213**, 149-157, doi:10.1016/S0378-1097(02)00774-7 (2002).

13 Beauzamy, L., Nakayama, N. & Boudaoud, A. Flowers under pressure: ins and outs of turgor regulation in development. *Annals of botany* **114**, 1517-1533, doi:10.1093/aob/mcu187 (2014).

14 Bek, E. J. & Badger, M. R. Multiple Rubisco forms in proteobacteria: their functional significance in relation to CO2 acquisition by the CBB cycle. *Journal of Experimental Botany* **59**, 1525-1541, doi:10.1093/jxb/erm297 (2008).

15 Belenky, M., Meyers, R. & Herzfeld, J. Subunit Structure of Gas Vesicles: A MALDI-TOF Mass Spectrometry Study. *Biophysical Journal* **86**, 499-505, doi:10.1016/S0006-3495(04)74128-4 (2004).

16 Bennett, V. & Lambert, S. The spectrin skeleton: from red cells to brain. The Journal of clinical investigation 87, 1483-1489, doi:10.1172/JCI115157 (1991).

17 Bentley, S. D. *et al.* Complete genome sequence of the model actinomycete Streptomyces coelicolor A3(2). *Nature* **417**, 141, doi:10.1038/417141a (2002).

18 Berntzon, L. *et al.* BMAA inhibits nitrogen fixation in the cyanobacterium Nostoc sp. PCC 7120. *Mar Drugs* **11**, 3091-3108, doi:10.3390/md11083091 (2013).

19 Bhaya, D. Light matters: phototaxis and signal transduction in unicellular cyanobacteria. *Molecular Microbiology* **53**, 745-754, doi:10.1111/j.1365-2958.2004.04160.x (2004).

20 Bin Omar, A. & Bin MatJafri, M. Turbidimeter Design and Analysis: A Review on Optical Fiber Sensors for the Measurement of Water Turbidity. *Sensors* **9**, 8311 (2009).

21 Blaurock, A. E. & Walsby, A. E. Crystalline structure of the gas vesicle wall from Anabaena flos-aquae. *Journal of Molecular Biology* **105**, 183-199, doi:10.1016/0022-2836(76)90106-6 (1976).

22 Blodgett, J. K. & Loudon, G. M. Direct cleavage versus transpeptidation in the autodecomposition of peptides containing 2,4-diaminobutanoic acid (DABA) and 2,3-diaminopropanoic acid (DAPA) residues. Specific cleavage of DAPA-containing peptides. *Journal of the American Chemical Society* **111**, 6813-6821, doi:10.1021/ja00199a049 (1989).

23 Boone, D. R., Castenholz, R. W. & Garrity, G. M. *Bergey's manual of systematic bacteriology*. (Springer, 2001).

24 Bouma-Gregson, K., Power, M. E. & Bormans, M. Rise and fall of toxic benthic freshwater cyanobacteria (Anabaena spp.) in the Eel river: Buoyancy and dispersal. *Harmful Algae* **66**, 79-87, doi:10.1016/j.hal.2017.05.007 (2017).

25 Bourdeau, R. W. *et al.* Acoustic reporter genes for noninvasive imaging of microorganisms in mammalian hosts. *Nature* **553**, 86, (2018).

26 Brand, L. E., Pablo, J., Compton, A., Hammerschlag, N. & Mash, D. C. Cyanobacterial blooms and the occurrence of the neurotoxin, beta-N-methylamino-l-alanine (BMAA), in South Florida aquatic food webs. *Harmful Algae* **9**, 620-635, doi:10.1016/j.hal.2010.05.002 (2010).

27 Breimer, L. H. & Lindahl, T. Thymine lesions produced by ionizing radiation in double-stranded DNA. *Biochemistry* 24, 4018-4022 (1985).

28 Brocks, J. J., Logan, G. A., Buick, R. & Summons, R. E. Archean Molecular Fossils and the Early Rise of Eukaryotes. *Science* **285**, 1033-1036, doi:10.1126/science.285.5430.1033 (1999).

29 Brookes, J. D. & Ganf, G. G. Variations in the buoyancy response of Microcystis aeruginosa to nitrogen, phosphorus and light. *Journal of Plankton Research* **23**, 1399-1411, doi:10.1093/plankt/23.12.1399 (2001).

30 Broome, B. M. & Hecht, M. H. Nature disfavors sequences of alternating polar and non-polar amino acids: implications for amyloidogenesis. J Mol Biol 296, 961-968, doi:10.1006/jmbi.2000.3514 (2000).

31 Buchholz, B. E. E., Hayes, P. k. & Walsby, A. E. The distribution of the outer gas vesicle protein, GvpC, on the Anabaena gas vesicle, and its ratio to GvpA. *Microbiology* **139**, 2353-2363, doi:10.1099/00221287-139-10-2353 (1993).

32 Butterfield, D. A. in Biological Magnetic Resonance: Volume 4 (eds Lawrence J. Berliner & Jacques Reuben) 1-78 (Springer US, 1982).

33 Butterfield, D. A., Hall, N. C. & Cross, S. J. Effects of .beta.-(N-methylamino)-L-alanine on cytoskeletal proteins of erythrocyte membranes. *Chemical Research in Toxicology* **6**, 417-420, doi:10.1021/tx00034a004 (1993).

34 Canadell, J. G. *et al.* Contributions to accelerating atmospheric CO2 growth from economic activity, carbon intensity, and efficiency of natural sinks. *Proceedings of the National Academy of Sciences* **104**, 18866-18870, doi:10.1073/pnas.0702737104 (2007).

35 Carneiro, R. L., Pacheco, A. B. & de Oliveira e Azevedo, S. M. Growth and saxitoxin production by Cylindrospermopsis raciborskii (cyanobacteria) correlate with water hardness. *Mar Drugs* **11**, 2949-2963, doi:10.3390/md11082949 (2013).

36 Casamayor, E. O., Schäfer, H., Bañeras, L., Pedrós-Alió, C. & Muyzer, G. Identification of and spatio-temporal differences between microbial assemblages from two neighboring sulfurous lakes: comparison by microscopy and denaturing gradient gel electrophoresis. *Applied and environmental microbiology* **66**, 499-508 (2000).

37 Castellani, R. J. *et al.* Active glycation in neurofibrillary pathology of Alzheimer disease: Nε-(Carboxymethyl) lysine and hexitol-lysine. *Free Radical Biology and Medicine* **31**, 175-180, doi:10.1016/S0891-5849(01)00570-6 (2001).

38 Castenholz, R. W. & Garcia-Pichel, F. in *Ecology of Cyanobacteria II: Their Diversity in Space and Time* (ed Brian A. Whitton) 481-499 (Springer Netherlands, 2012).

39 Cherin, E. *et al.* Acoustic Behavior of Halobacterium salinarum Gas Vesicles in the High-Frequency Range: Experiments and Modeling. *Ultrasound in Medicine & Biology* **43**, 1016-1030, doi:10.1016/j.ultrasmedbio.2016.12.020 (2017).

40 Chernoff, N. *et al.* A critical review of the postulated role of the non-essential amino acid, beta-N-methylamino-L-alanine, in neurodegenerative disease in humans. *J Toxicol Environ Health B Crit Rev* **20**, 1-47, doi:10.1080/10937404.2017.1297592 (2017).

41 Chien, A.-C., Hill, N. S. & Levin, P. A. Cell size control in bacteria. *Current biology: CB* **22**, R340-R349, doi:10.1016/j.cub.2012.02.032 (2012).

42 Cohen, S. A. Analytical techniques for the detection of α-amino-β-methylaminopropionic acid. *Analyst* **137**, 1991-2005, doi:10.1039/C2AN16250D (2012).

43 Cox, P. A., Banack, S. A. & Murch, S. J. Biomagnification of cyanobacterial neurotoxins and neurodegenerative disease among the Chamorro people of Guam. *Proceedings of the National Academy of Sciences* **100**, 13380-13383, doi:10.1073/pnas.2235808100 (2003).

44 Cox, P. A. *et al.* Diverse taxa of cyanobacteria produce beta-N-methylamino-L-alanine, a neurotoxic amino acid. *Proc Natl Acad Sci U S A* **102**, 5074-5078, doi:10.1073/pnas.0501526102 (2005).

45 Cox, P. A., Davis, D. A., Mash, D. C., Metcalf, J. S. & Banack, S. A. Dietary exposure to an environmental toxin triggers neurofibrillary tangles and amyloid deposits in the brain. *Proc Biol Sci* **283**, doi:10.1098/rspb.2015.2397 (2016).

46 Crumpton, W. G. A simple and reliable method for making permanent mounts of phytoplankton for light and fluorescence microscopy1. *Limnology and Oceanography* **32**, 1154-1159, doi:10.4319/lo.1987.32.5.1154 (1987).

47 Daley, S. M., Kappell, A. D., Carrick, M. J. & Burnap, R. L. Regulation of the cyanobacterial CO2-concentrating mechanism involves internal sensing of NADP+ and alpha-ketogutarate levels by transcription factor CcmR. *PLoS One* **7**, e41286, doi:10.1371/journal.pone.0041286 (2012).

48 Daley, S. M. E., Kappell, A. D., Carrick, M. J. & Burnap, R. L. Regulation of the Cyanobacterial CO2-Concentrating Mechanism Involves Internal Sensing of NADP+ and α-Ketogutarate Levels by Transcription Factor CcmR. *PLOS ONE* **7**, e41286, doi:10.1371/journal.pone.0041286 (2012).

49 Davidson, A. L., Dassa, E., Orelle, C. & Chen, J. Structure, Function, and Evolution of Bacterial ATP-Binding Cassette Systems. *Microbiology and Molecular Biology Reviews* **72**, 317-364, doi:10.1128/mmbr.00031-07 (2008).

50 Delwiche, C. F. & Palmer, J. D. Rampant horizontal transfer and duplication of rubisco genes in eubacteria and plastids. *Molecular Biology and Evolution* **13**, 873-882, doi:10.1093/oxfordjournals.molbev.a025647 (1996).

51 DeMott, W. R., Zhang, Q.-X. & Carmichael, W. W. Effects of toxic cyanobacteria and purified toxins on the survival and feeding of a copepod and three species of

Daphnia. *Limnology and Oceanography* **36**, 1346-1357, doi:10.4319/lo.1991.36.7.1346 (1991).

52 Dervaux, J., Mejean, A. & Brunet, P. Irreversible collective migration of cyanobacteria in eutrophic conditions. *PLoS One* **10**, e0120906, doi:10.1371/journal.pone.0120906 (2015).

53 Downing, S., Banack, S. A., Metcalf, J. S., Cox, P. A. & Downing, T. G. Nitrogen starvation of cyanobacteria results in the production of beta-N-methylamino-L-alanine. *Toxicon* **58**, 187-194, doi:10.1016/j.toxicon.2011.05.017 (2011).

54 Downing, S. & Downing, T. G. The metabolism of the non-proteinogenic amino acid beta-N-methylamino-L-alanine (BMAA) in the cyanobacterium Synechocystis PCC6803. *Toxicon* **115**, 41-48, doi:10.1016/j.toxicon.2016.03.005 (2016).

55 Downing, S., van de Venter, M. & Downing, T. G. The effect of exogenous beta-N-methylamino-L: -alanine on the growth of Synechocystis PCC6803. *Microb Ecol* **63**, 149-156, doi:10.1007/s00248-011-9958-9 (2012).

56 Duncan, M. W. Good mass spectrometry and its place in good science. *Journal of Mass Spectrometry* **47**, 795-809, doi:10.1002/jms.3038 (2012).

57 Dunlop, R. A., Cox, P. A., Banack, S. A. & Rodgers, K. J. The Non-Protein Amino Acid BMAA Is Misincorporated into Human Proteins in Place of l-Serine Causing Protein Misfolding and Aggregation. PLOS ONE 8, e75376, doi:10.1371/journal.pone.0075376 (2013).

58 Dunton, P. G., Mawby, W. J., Shaw, V. A. & Walsby, A. E. Analysis of tryptic digests indicates regions of GvpC that bind to gas vesicles of Anabaena flos-aquae. *Microbiology* **152**, 1661-1669, doi:10.1099/mic.0.28755-0 (2006).

59 Dunton, P. G. & Walsby, A. E. The diameter and critical collapse pressure of gas vesicles in Microcystis are correlated with GvpCs of different length. *FEMS Microbiology Letters* **247**, 37-43, doi:10.1016/j.femsle.2005.04.026 (2005).

60 Edwards, D. J. *et al.* Structure and biosynthesis of the jamaicamides, new mixed polyketide-peptide neurotoxins from the marine cyanobacterium Lyngbya majuscula. *Chem Biol* **11**, 817-833, doi:10.1016/j.chembiol.2004.03.030 (2004).

61 Eichler, B. & Pfennig, N. A new purple sulfur bacterium from stratified freshwater lakes, Amoebobacter purpureus sp. nov. *Archives of Microbiology* **149**, 395-400, doi:10.1007/bf00425577 (1988).

62 Elliott, J. A., Jones, I. D. & Thackeray, S. J. Testing the Sensitivity of Phytoplankton Communities to Changes in Water Temperature and Nutrient Load, in a Temperate Lake. *Hydrobiologia* **559**, 401-411, doi:10.1007/s10750-005-1233-y (2006).

63 Ellis, R. J. The most abundant protein in the world. *Trends in Biochemical Sciences* **4**, 241-244, doi:10.1016/0968-0004(79)90212-3 (1979).

64 Englert, C. & Pfeifer, F. Analysis of gas vesicle gene expression in Haloferax mediterranei reveals that GvpA and GvpC are both gas vesicle structural proteins. *Journal of Biological Chemistry* **268**, 9329-9336 (1993).

65 Enomoto, G., Ni-Ni-Win, Narikawa, R. & Ikeuchi, M. Three cyanobacteriochromes work together to form a light color-sensitive input system for c-di-GMP signaling of cell aggregation. *Proceedings of the National Academy of Sciences* **112**, 8082-8087, doi:10.1073/pnas.1504228112 (2015).

66 EPA. 1984a. Sample preservation. In methods for chemical analysis of water and wastewater. Cincinnati: Environmental Monitoring and Support Laboratory, Office of Research and Development, U.S. Environmental Protection Agency.

67 EPA. 1984b. Phosphorous, all forms method 365.1 (colorimetric, automated ascorbic acid). In methods for chemical analysis of water and wastewater. Cincinnati: Environmental Monitoring and Support Laboratory, Office of Research and Development, U.S. Environmental Protection Agency.

68 EPA. 1984c. Nitrogen, ammonium method 350.1 (colorimetric, automated phenate). In methods for chemical analysis of water and wastewater. Cincinnati: Environmental Monitoring and Support Laboratory, Office of Research and Development, U.S. Environmental Protection Agency.

69 Epstein, W. *et al.* The bacterial Kdp K+-ATPase and its relation to other transport ATPases, such as the Na+/K+ and Ca2+-ATPases in higher organisms. *Philosophical Transactions of the Royal Society of London. B, Biological Sciences* **326**, 479-487, doi:10.1098/rstb.1990.0026 (1990).

70 Ernst, A. & Böger, P. Glycogen Accumulation and the Induction of Nitrogenase Activity in the Heterocyst-forming Cyanobacterium Anabaena variabilis. *Microbiology* **131**, 3147-3153, doi:10.1099/00221287-131-12-3147 (1985).

71 Ezzeldin, H. M., Klauda, J. B. & Solares, S. D. Modeling of the major gas vesicle protein, GvpA: From protein sequence to vesicle wall structure. *Journal of Structural Biology* **179**, 18-28, doi:10.1016/j.jsb.2012.04.015 (2012).

72 Faassen, E. J. *et al.* A Collaborative Evaluation of LC-MS/MS Based Methods for BMAA Analysis: Soluble Bound BMAA Found to Be an Important Fraction. *Mar Drugs* **14**, doi:10.3390/md14030045 (2016).

73 Faassen, E. J., Gillissen, F. & Lürling, M. A Comparative Study on Three Analytical Methods for the Determination of the Neurotoxin BMAA in Cyanobacteria. *PLOS ONE* **7**, e36667, doi:10.1371/journal.pone.0036667 (2012).

74 Falkowski, P. G. & Raven, J. A. *Aquatic Photosynthesis (2nd Edition)*. (Princeton University Press, 2007).

75 Fawcett, E.H., & Acree, S.F. Stabilization of Boric Acid Buffers by Aeration. *National Institute of Science & Technology* **RP302**, 757-763, (1929).

76 Fazal, K., Perera, G., Khondoker, M., Howard, R. & Stewart, R. Associations of centrally acting ACE inhibitors with cognitive decline and survival in Alzheimer's disease. *BJPsych open* **3**, 158-164, doi:10.1192/bjpo.bp.116.004184 (2017).

77 Fewer, D. P. *et al.* Non-autonomous transposable elements associated with inactivation of microcystin gene clusters in strains of the genus Anabaena isolated from the Baltic Sea. *Environmental Microbiology Reports* **3**, 189-194, doi:10.1111/j.1758-2229.2010.00207.x (2011).

78 Figge, R. M., Cassier-Chauvat, C., Chauvat, F. & Cerff, R. Characterization and analysis of an NAD(P)H dehydrogenase transcriptional regulator critical for the survival of cyanobacteria facing inorganic carbon starvation and osmotic stress. *Molecular Microbiology* **39**, 455-469, doi:10.1046/j.1365-2958.2001.02239.x (2001).

79 Flombaum, P. *et al.* Present and future global distributions of the marine Cyanobacteria Prochlorococcus and Synechococcus. *Proceedings of the National Academy of Sciences* **110**, 9824-9829, doi:10.1073/pnas.1307701110 (2013).

80 Flores, E. & Herrero, A. Nitrogen assimilation and nitrogen control in cyanobacteria. Biochemical Society transactions 33, 164-167, doi:10.1042/bst0330164 (2005).

81 Foss, A. J., Chernoff, N. & Aubel, M. T. The analysis of underivatized β-Methylamino-L-alanine (BMAA), BAMA, AEG & 2,4-DAB in Pteropus mariannus mariannus specimens using HILIC-LC-MS/MS. *Toxicon* **152**, 150-159, doi:10.1016/j.toxicon.2018.07.028 (2018).

82 Frenken, T. *et al.* Fungal parasites of a toxic inedible cyanobacterium provide food to zooplankton. *Limnology and Oceanography* **63**, 2384-2393, doi:10.1002/lno.10945 (2018).

83 Fujisawa, T. et al. CyanoBase: a large-scale update on its 20th anniversary. *Nucleic Acids Res* 45, D551-D554, doi:10.1093/nar/gkw1131 (2017).

84 Gajdusek , D. C. Motor-Neuron Disease in Natives of New Guinea. *New England Journal of Medicine* **268**, 474-476, doi:10.1056/nejm196302282680906 (1963).

85 Gao, H. *et al.* pH-dependent gas vesicle formation in Microcystis. *FEBS Letters* **590**, 3195-3201, doi:10.1002/1873-3468.12370 (2016).

86 Garcia-Pichel, F. Solar Ultraviolet and the Evolutionary History of Cyanobacteria. Origins of life and evolution of the biosphere 28, 321-347, doi:10.1023/a:1006545303412 (1998).

87 George, S. E. & Ramani, A. K. Monensin Inhibition of Na^+-Dependent HCO_3^- Transport Distinguishes It from Na^+-Independent HCO_3^- Transport and Provides

Evidence for Na^+/HCO_3^- Symport in the Cyanobacterium Synechococcus UTEX 625. *Plant Physiology* **104**, 1419-1428 (1994).

88 Ginn, H. P., Pearson, L. A. & Neilan, B. A. NtcA from Microcystis aeruginosa PCC 7806 is autoregulatory and binds to the microcystin promoter. *Appl Environ Microbiol* **76**, 4362-4368, doi:10.1128/AEM.01862-09 (2010).

89 Glover, W. B., Baker, T. C., Murch, S. J. & Brown, P. Determination of β-N-methylamino-L-alanine, N-(2-aminoethyl)glycine, and 2,4-diaminobutyric acid in Food Products Containing Cyanobacteria by Ultra-Performance Liquid Chromatography and Tandem Mass Spectrometry: Single-Laboratory Validation. *J AOAC Int* **98**, 1559-1565, doi:10.5740/jaoacint.15-084 (2015).

90 Glover, W. B. *et al.* Reactivity of beta-methylamino-L-alanine in complex sample matrixes complicating detection and quantification by mass spectrometry. *Anal Chem* **84**, 7946-7953, doi:10.1021/ac301691r (2012).

91 Gómez-Casati, D. F., Cortassa, S., Aon, M. A. & Iglesias, A. A. Ultrasensitive behavior in the synthesis of storage polysaccharides in cyanobacteria. *Planta* **216**, 969-975, doi:10.1007/s00425-002-0949-4 (2003).

92 Gorl, M., Sauer, J., Baier, T. & Forchhammer, K. Nitrogen-starvation-induced chlorosis in Synechococcus PCC 7942: adaptation to long-term survival. Microbiology 144 (Pt 9), 2449-2458, doi:10.1099/00221287-144-9-2449 (1998).

93 Gros, C. & Labouesse, B. Study of the Dansylation Reaction of Amino Acids, Peptides and Proteins. *European Journal of Biochemistry* **7**, 463-470, doi:10.1111/j.1432-1033.1969.tb19632.x (1969).

94 Gugger, M. F. & Hoffmann, L. Polyphyly of true branching cyanobacteria (Stigonematales). *International Journal of Systematic and Evolutionary Microbiology* **54**, 349-357, doi:10.1099/ijs.0.02744-0 (2004).

95 Guyoneaud, R. *et al.* Taxonomic rearrangements of the genera Thiocapsa and Amoebobacter on the basis of 16S rDNA sequence analyses, and description of Thiolamprovum gen. nov. *International Journal of Systematic and Evolutionary Microbiology* **48**, 957-964, doi:10.1099/00207713-48-3-957 (1998).

96 Guz, N., Dokukin, M., Kalaparthi, V. & Sokolov, I. If cell mechanics can be described by elastic modulus: study of different models and probes used in indentation experiments. *Biophysical journal* **107**, 564-575, doi:10.1016/j.bpj.2014.06.033 (2014).

97 Hawkins, P. R., Runnegar, M. T., Jackson, A. R. & Falconer, I. R. Severe hepatotoxicity caused by the tropical cyanobacterium (blue-green alga) Cylindrospermopsis raciborskii (Woloszynska) Seenaya and Subba Raju isolated from a domestic water supply reservoir. *Applied and Environmental Microbiology* **50**, 1292-1295 (1985).

98 Hayes, P. K. & Walsby, A. E. An Investigation into the Recycling of Gas Vesicle Protein Derived from Collapsed Gas Vesicles. *Microbiology* **130**, 1591-1596, doi:10.1099/00221287-130-6-1591 (1984).

99 Hayes, P. K. & Walsby, A. E. The inverse correlation between width and strength of gas vesicles in cyanobacteria. *British Phycological Journal* **21**, 191-197, doi:10.1080/00071618600650221 (1986).

100 Heimbecher, S., Lee, Y.-C., Esmail Tabibi, S. & Yalkowsky, S. H. Derivatization and high-performance liquid chromatographic analysis of pentaazapentacosane pentahydrochloride. *Journal of Chromatography B: Biomedical Sciences and Applications* **691**, 173-178, doi:10.1016/S0378-4347(96)00452-5 (1997).

101 Heimbecher, S., Lee, Y.-C., Tabibi, S. E. & Yalkowsky, S. H. Mechanism of dansylation of the polyamine pentaazapentacosane ·5 HCl. *International Journal of Pharmaceutics* **160**, 21-29, doi:10.1016/S0378-5173(97)00315-3 (1998).

102 Hemming, M. L. & Selkoe, D. J. Amyloid beta-protein is degraded by cellular angiotensin-converting enzyme (ACE) and elevated by an ACE inhibitor. *The Journal of biological chemistry* **280**, 37644-37650, doi:10.1074/jbc.M508460200 (2005).

103 Hickman, J. W. *et al.* Glycogen synthesis is a required component of the nitrogen stress response in Synechococcus elongatus PCC 7942. *Algal Research* **2**, 98-106, doi:10.1016/j.algal.2013.01.008 (2013).

104 Higgins, C. F. ABC Transporters: From Microorganisms to Man. *Annual Review of Cell Biology* **8**, 67-113, doi:10.1146/annurev.cb.08.110192.000435 (1992).

105 Hisbergues, M., Jeanjean, R., Joset, F., Tandeau de Marsac, N. & Bédu, S. Protein PII regulates both inorganic carbon and nitrate uptake and is modified by a redox signal in Synechocystis PCC 6803. *FEBS Letters* **463**, 216-220, doi:10.1016/S0014-5793(99)01624-5 (1999).

106 Holland, A. & Kinnear, S. Interpreting the possible ecological role(s) of cyanotoxins: compounds for competitive advantage and/or physiological aide? *Mar Drugs* **11**, 2239-2258, doi:10.3390/md11072239 (2013).

107 Holland, D. P. & Walsby, A. E. Digital recordings of gas-vesicle collapse used to measure turgor pressure and cell–water relations of cyanobacterial cells. *Journal of Microbiological Methods* **77**, 214-224, doi:10.1016/j.mimet.2009.02.005 (2009).

108 Humpage, A. R., Fontaine, F., Froscio, S., Burcham, P. & Falconer, I. R. Cylindrospermopsin genotoxicity and cytotoxicity: role of cytochrome P-450 and oxidative stress. *Journal of Toxicology and Environmental Health, Part A* **68**, 739-753 (2005).

109 Ibelings, B. W., Kroon, B. M. A. & Mur, L. R. Acclimation of photosystem II in a cyanobacterium and a eukaryotic green alga to high and fluctuating photosynthetic photon flux densities, simulating light regimes induced by mixing in lakes. *New Phytologist* **128**, 407-424, doi:10.1111/j.1469-8137.1994.tb02987.x (1994).

110 Ibelings, B. W. & Maberly, S. C. Photoinhibition and the availability of inorganic carbon restrict photosynthesis by surface blooms of cyanobacteria. *Limnology and Oceanography* **43**, 408-419, doi:10.4319/lo.1998.43.3.0408 (1998).

111 ISO. Water quality—Determination of turbidity—part 1: Quantitative methods. International Standards Organization 7027-1:2016.

112 Jain, I. H., Vijayan, V. & O'Shea, E. K. Spatial ordering of chromosomes enhances the fidelity of chromosome partitioning in cyanobacteria. *Proceedings of the National Academy of Sciences* **109**, 13638-13643, doi:10.1073/pnas.1211144109 (2012).

113 Jarrell, K. F. & McBride, M. J. The surprisingly diverse ways that prokaryotes move. *Nature Reviews Microbiology* **6**, 466 (2008).

114 Jian Wei, Y., Price, G. & Badger, M. R. *Characterisation of CO2 and HCO3- uptake during steady-state photosynthesis in the cyanobacterium Synechococcus PCC7942*. Vol. 21 (1994).

115 Jiang, L., Kiselova, N., Rosén, J. & Ilag, L. L. Quantification of neurotoxin BMAA (β-N-methylamino-L-alanine) in seafood from Swedish markets. *Scientific Reports* **4**, 6931, doi:10.1038/srep06931 (2014).

116 Jiao, Y. *et al.* Occurrence and transfer of a cyanobacterial neurotoxin β-methylamino-l-alanine within the aquatic food webs of Gonghu Bay (Lake Taihu, China) to evaluate the potential human health risk. *Science of The Total Environment* **468-469**, 457-463, doi:10.1016/j.scitotenv.2013.08.064 (2014).

117 Jöhnk, K. D. *et al.* Summer heatwaves promote blooms of harmful cyanobacteria. *Global Change Biology* **14**, 495-512, doi:10.1111/j.1365-2486.2007.01510.x (2008).

118 Jonasson, S. *et al.* Transfer of a cyanobacterial neurotoxin within a temperate aquatic ecosystem suggests pathways for human exposure. *Proceedings of the National Academy of Sciences* **107**, 9252-9257, doi:10.1073/pnas.0914417107 (2010).

119 Jones, D. T. Protein secondary structure prediction based on position-specific scoring matrices. J Mol Biol 292, 195-202, doi:10.1006/jmbi.1999.3091 (1999).

120 Jurk, M., Dorn, M. & Schmieder, P. Blue Flickers of Hope: Secondary Structure, Dynamics, and Putative Dimerization Interface of the Blue-Light Receptor YtvA from Bacillus subtilis. *Biochemistry* **50**, 8163-8171, doi:10.1021/bi200782j (2011).

121 Kaebernick, M., Neilan, B. A., Börner, T. & Dittmann, E. Light and the Transcriptional Response of the Microcystin Biosynthesis Gene Cluster. *Applied and Environmental Microbiology* **66**, 3387-3392 (2000).

122 Kamberov, E. S., Atkinson, M. R. & Ninfa, A. J. The Escherichia coli PII Signal Transduction Protein Is Activated upon Binding 2-Ketoglutarate and ATP. *Journal of Biological Chemistry* **270**, 17797-17807, doi:10.1074/jbc.270.30.17797 (1995).

123 Kamennaya, N., Ajo-Franklin, C., Northen, T. & Jansson, C. Cyanobacteria as Biocatalysts for Carbonate Mineralization. Minerals 2, 338-364, doi:10.3390/min2040338 (2012).

124 Kaneko, T. *et al.* Complete genomic structure of the bloom-forming toxic cyanobacterium Microcystis aeruginosa NIES-843. *DNA research* **14**, 247-256, doi:10.1093/dnares/dsm026 (2007).

125 Kaneko, T. *et al.* Sequence analysis of the genome of the unicellular cyanobacterium Synechocystis sp. strain PCC6803. II. Sequence determination of the entire genome and assignment of potential protein-coding regions. *DNA Res* **3**, 109-136 (1996).

126 Kaplan, A. *et al.* The languages spoken in the water body (or the biological role of cyanobacterial toxins). *Front Microbiol* **3**, 138, doi:10.3389/fmicb.2012.00138 (2012).

127 Karle, I. L., Flippen-Anderson, J. L., Agarwalla, S. & Balaram, P. Crystal structure of [Leu1]zervamicin, a membrane ion-channel peptide: implications for gating mechanisms. *Proceedings of the National Academy of Sciences* **88**, 5307-5311, doi:10.1073/pnas.88.12.5307 (1991).

128 Kashyap, S., Sundararajan, A. & Ju, L.-K. Flotation characteristics of cyanobacterium Anabaena flos-aquae for gas vesicle production. *Biotechnology and Bioengineering* **60**, 636-641, (1998).

129 Kanehisa, M. & Goto, S. KEGG: kyoto encyclopedia of genes and genomes. *Nucleic Acids Res* 28, 27-30 (2000).

a. “Glutamate metabolism.” <https://www.kegg.jp/kegg-bin/show_pathway?mar00471> (2019).
b. “Cyanoamino acid metabolism.” <https://www.kegg.jp/kegg-bin/show_pathway?mar00460> (2018).
c. “Glyoxylate metabolism.” <https://www.kegg.jp/kegg-bin/show_pathway?mar00630> (2018).
d. “Methane metabolism.” <https://www.kegg.jp/kegg-bin/show_pathway?mar00680> (2018).
e. “Arginine biosynthesis.” <https://www.kegg.jp/kegg-bin/show_pathway?mar00220> (2017).

130 Kiil, F. Molecular mechanisms of osmosis. *American Journal of Physiology-Regulatory, Integrative and Comparative Physiology* **256**, R801-R808, doi:10.1152/ajpregu.1989.256.4.R801 (1989).

131 Kim, Y. H. & Lim, B. U. A novel tautomerism in alkyl dihydropyrimidines: observation of tautomerism by H-D exchange of 2- and/or 4-methyl protons of dihydropyrimidines in CD3OD. *Tetrahedron Letters* **32**, 2057-2060, doi:10.1016/S0040-4039(00)78907-6 (1991).

132 King, D. L. The Role of Carbon in Eutrophication. *Journal (Water Pollution Control Federation)* **42**, 2035-2051 (1970).

133 Kinsman, R., Ibelings, B. W. & Walsby, A. E. Gas vesicle collapse by turgor pressure and its role in buoyancy regulation by Anabaena flos-aquae. *Microbiology* **137**, 1171-1178, doi:10.1099/00221287-137-5-1171 (1991).

134 Klausmeier, C. A., Litchman, E. & Levin, S. A. Phytoplankton growth and stoichiometry under multiple nutrient limitation. *Limnology and Oceanography* **49**, 1463-1470, doi:10.4319/lo.2004.49.4_part_2.1463 (2004).

135 Klotz, A., Reinhold, E., Doello, S. & Forchhammer, K. Nitrogen Starvation Acclimation in Synechococcus elongatus: Redox-Control and the Role of Nitrate Reduction as an Electron Sink. *Life (Basel)* **5**, 888-904, doi:10.3390/life5010888 (2015).

136 Knitsch, R., Schneefeld, M., Weitzel, K. & Pfeifer, F. Mutations in the major gas vesicle protein GvpA and impacts on gas vesicle formation in Haloferax volcanii. *Molecular Microbiology* **106**, 530-542, doi:10.1111/mmi.13833 (2017).

137 Koenig, J. H., Goto, J. J. & Ikeda, K. Novel NMDA receptor-specific desensitization/inactivation produced by ingestion of the neurotoxins, beta-N-methylamino-L-alanine (BMAA) or beta-N-oxalylamino-L-alanine (BOAA/beta-ODAP). *Comp Biochem Physiol C Toxicol Pharmacol* **167**, 43-50, doi:10.1016/j.cbpc.2014.08.006 (2015).

138 Kopf, M., Möke, F., Bauwe, H., Hess, W. R. & Hagemann, M. Expression profiling of the bloom-forming cyanobacterium Nodularia CCY9414 under light and oxidative stress conditions. *The Isme Journal* **9**, 2139 (2015).

139 Kuo-Dahab, W. C. *et al.* Investigation of the Fate and Dynamics of Extracellular Polymeric Substances (EPS) during Sludge-Based Photogranulation under

Hydrostatic Conditions. *Environmental Science & Technology* **52**, 10462-10471, doi:10.1021/acs.est.8b03033 (2018).

140 Lage, S. *et al.* BMAA extraction of cyanobacteria samples: which method to choose? *Environmental Science and Pollution Research* **23**, 338-350, doi:10.1007/s11356-015-5266-0 (2016).

141 Larkin, M. A. et al. Clustal W and Clustal X version 2.0. Bioinformatics 23, 2947-2948, doi:10.1093/bioinformatics/btm404 (2007).

142 Li, N. & Cannon, M. C. Gas Vesicle Genes Identified in Bacillus megaterium and Functional Expression in Escherichia coli. *Journal of Bacteriology* **180**, 2450-2458 (1998).

143 Ling, J. & Söll, D. Severe oxidative stress induces protein mistranslation through impairment of an aminoacyl-tRNA synthetase editing site. Proceedings of the National Academy of Sciences 107, 4028-4033, doi:10.1073/pnas.1000315107 (2010).

144 Littler, D. R. *et al.* The Intracellular Chloride Ion Channel Protein CLIC1 Undergoes a Redox-controlled Structural Transition. *Journal of Biological Chemistry* **279**, 9298-9305, doi:10.1074/jbc.M308444200 (2004).

145 Liu, H. *et al.* Phycobilisomes Supply Excitations to Both Photosystems in a Megacomplex in Cyanobacteria. *Science* **342**, 1104-1107, doi:10.1126/science.1242321 (2013).

146 Liu, X., Rush, T., Zapata, J. & Lobner, D. beta-N-methylamino-l-alanine induces oxidative stress and glutamate release through action on system Xc(-). *Exp Neurol* **217**, 429-433, doi:10.1016/j.expneurol.2009.04.002 (2009).

147 Lo, H. C., Iron, M. A., Martin, J. M. L. & Keinan, E. Proton Walk in the Aqueous Platinum Complex [TpPtMeCO] via a Sticky σ-Methane Ligand. *Chemistry – A European Journal* **13**, 2812-2823, doi:10.1002/chem.200600709 (2007).

148 Lund, J. W. G., Kipling, C. & Le Cren, E. D. The inverted microscope method of estimating algal numbers and the statistical basis of estimations by counting. *Hydrobiologia* **11**, 143-170, doi:10.1007/BF00007865 (1958).

149 Machnicka, B. et al. Spectrins: A structural platform for stabilization and activation of membrane channels, receptors and transporters. Biochimica et Biophysica Acta (BBA) - Biomembranes 1838, 620-634, doi:https://doi.org/10.1016/j.bbamem.2013.05.002 (2014).

150 Maeda, S.-i., Badger, M. R. & Price, G. D. Novel gene products associated with NdhD3/D4-containing NDH-1 complexes are involved in photosynthetic CO2 hydration in the cyanobacterium, Synechococcus sp. PCC7942. *Molecular Microbiology* **43**, 425-435, doi:10.1046/j.1365-2958.2002.02753.x (2002).

151 Manger, R. L. *et al.* Detection of sodium channel toxins: directed cytotoxicity assays of purified ciguatoxins, brevetoxins, saxitoxins, and seafood extracts. *J AOAC Int* **78**, 521-527 (1995).

152 Manolidi, K., Triantis, T. M., Kaloudis, T. & Hiskia, A. Neurotoxin BMAA and its isomeric amino acids in cyanobacteria and cyanobacteria-based food supplements. *Journal of Hazardous Materials* **365**, 346-365, doi:10.1016/j.jhazmat.2018.10.084 (2019).

153 Marles-Wright, J. *et al.* Molecular architecture of the "stressosome," a signal integration and transduction hub. *Science* **322**, 92-96, doi:10.1126/science.1159572 (2008).

154 Martin-Luna, B. *et al.* Fur from Microcystis aeruginosa binds in vitro promoter regions of the microcystin biosynthesis gene cluster. *Phytochemistry* **67**, 876-881, doi:10.1016/j.phytochem.2006.02.005 (2006).

155 Matsuoka, M., Horimoto, S., Mabuchi, M. & Banno, K. Determination of three metabolites of a new angiotensin-converting enzyme inhibitor, imidapril, in plasma and urine by gas chromatography—mass spectrometry using multiple ion detection. *Journal of Chromatography B: Biomedical Sciences and Applications* **581**, 65-73, doi:10.1016/0378-4347(92)80448-Y (1992).

156 Mazmouz, R. *et al.* Biosynthesis of cylindrospermopsin and 7-epicylindrospermopsin in Oscillatoria sp. strain PCC 6506: identification of the cyr gene cluster and toxin analysis. *Appl Environ Microbiol* **76**, 4943-4949, doi:10.1128/AEM.00717-10 (2010).

157 McMaster, T. J., Miles, M. J. & Walsby, A. E. Direct observation of protein secondary structure in gas vesicles by atomic force microscopy. *Biophysical Journal* **70**, 2432-2436, doi:10.1016/S0006-3495(96)79813-2 (1996).

158 Meiser, P. *et al.* DKxanthene Biosynthesis—Understanding the Basis for Diversity-Oriented Synthesis in Myxobacterial Secondary Metabolism. *Chemistry & Biology* **15**, 771-781, doi:10.1016/j.chembiol.2008.06.005 (2008).

159 Meissner, S., Steinhauser, D. & Dittmann, E. Metabolomic analysis indicates a pivotal role of the hepatotoxin microcystin in high light adaptation of Microcystis. *Environ Microbiol* **17**, 1497-1509, doi:10.1111/1462-2920.12565 (2015).

160 Méjean, A. *et al.* Evidence that Biosynthesis of the Neurotoxic Alkaloids Anatoxin-a and Homoanatoxin-a in the Cyanobacterium Oscillatoria PCC 6506 Occurs on a Modular Polyketide Synthase Initiated by l-Proline. *Journal of the American Chemical Society* **131**, 7512-7513, doi:10.1021/ja9024353 (2009).

161 Meriluoto, J., Spoof, L., & Codd, G., (Eds.) Handbook of Cyanobacterial Monitoring and Cyanotoxin analysis. Wiley, Chichester, UK (2017).

162 Metcalf, J. S. *et al.* Analysis of BMAA enantiomers in cycads, cyanobacteria, and mammals: in vivo formation and toxicity of D-BMAA. *Amino Acids* **49**, 1427-1439, doi:10.1007/s00726-017-2445-y (2017).

163 Meyer, K. A. *et al.* Genome sequences of lower Great Lakes Microcystis sp. reveal strain-specific genes that are present and expressed in western Lake Erie blooms. *PloS one* **12**, e0183859-e0183859, doi:10.1371/journal.pone.0183859 (2017).

164 Michalak, A. M. *et al.* Record-setting algal bloom in Lake Erie caused by agricultural and meteorological trends consistent with expected future conditions. *Proceedings of the National Academy of Sciences* **110**, 6448-6452, doi:10.1073/pnas.1216006110 (2013).

165 Mihali, T. K., Kellmann, R., Muenchhoff, J., Barrow, K. D. & Neilan, B. A. Characterization of the gene cluster responsible for cylindrospermopsin biosynthesis. *Appl Environ Microbiol* **74**, 716-722, doi:10.1128/AEM.01988-07 (2008).

166 Mlouka, A., Comte, K., Castets, A.-M., Bouchier, C. & Tandeau de Marsac, N. The Gas Vesicle Gene Cluster from Microcystis aeruginosa and DNA Rearrangements That Lead to Loss of Cell Buoyancy. *Journal of Bacteriology* **186**, 2355-2365, doi:10.1128/jb.186.8.2355-2365.2004 (2004).

167 Molot, L. A. *et al.* A novel model for cyanobacteria bloom formation: the critical role of anoxia and ferrous iron. *Freshwater Biology* **59**, 1323-1340, doi:10.1111/fwb.12334 (2014).

168 Monismith, S. G., Imberger, J. & Morison, M. L. Convective motions in the sidearm of a small reservoir. *Limnology and Oceanography* **35**, 1676-1702, doi:10.4319/lo.1990.35.8.1676 (1990).

169 Monson, C. S., Banack, S. A. & Cox, P. A. Conservation Implications of Chamorro Consumption of Flying Foxes as a Possible Cause of Amyotrophic Lateral Sclerosis–Parkinsonism Dementia Complex in Guam. *Conservation Biology* **17**, 678-686, doi:10.1046/j.1523-1739.2003.02049.x (2003).

170 Moon, Y. J., Kim, S. I. & Chung, Y. H. Sensing and responding to UV-A in cyanobacteria. *Int J Mol Sci* **13**, 16303-16332, doi:10.3390/ijms131216303 (2012).

171 Morse, J. W., Arvidson, R. S. & Lüttge, A. Calcium Carbonate Formation and Dissolution. Chemical Reviews 107, 342-381, doi:10.1021/cr050358j (2007).

172 Murch, S. J., Cox, P. A. & Banack, S. A. A mechanism for slow release of biomagnified cyanobacterial neurotoxins and neurodegenerative disease in Guam. *Proc Natl Acad Sci U S A* **101**, 12228-12231, doi:10.1073/pnas.0404926101 (2004).

173 Muro-Pastor, M. I., Reyes, J. C. & Florencio, F. J. Cyanobacteria perceive nitrogen status by sensing intracellular 2-oxoglutarate levels. J Biol Chem 276, 38320-38328, doi:10.1074/jbc.M105297200 (2001).

174 Murzin, A. G. Metamorphic Proteins. *Science* **320**, 1725-1726, doi:10.1126/science.1158868 (2008).

175 Nadimpally, K. C., Paul, A. & Mandal, B. Reversal of Aggregation Using β-Breaker Dipeptide Containing Peptides: Application to Aβ(1–40) Self-Assembly and Its Inhibition. *ACS Chemical Neuroscience* **5**, 400-408, doi:10.1021/cn500064z (2014).

176 Neilan, B. A., Pearson, L. A., Muenchhoff, J., Moffitt, M. C. & Dittmann, E. Environmental conditions that influence toxin biosynthesis in cyanobacteria. *Environmental Microbiology* **15**, 1239-1253, doi:10.1111/j.1462-2920.2012.02729.x (2013).

177 Nelson, D. L., Cox, M. M. & Lehninger, A. L. *Lehninger principles of biochemistry*. (W.H. Freeman, 2013).

178 NOAA. 2019. Local climatological data daily summary: July-September 2017. National Oceanic & Atmospheric Administration: National Environmental Satellite, Data, and Information Service.

179 Nozaki, H. *et al.* Cyanobacterial genes transmitted to the nucleus before divergence of red algae in the Chromista. *J Mol Evol* **59**, 103-113, doi:10.1007/s00239-003-2611-1 (2004).

180 Nunn, P. B. & Codd, G. A. Metabolic solutions to the biosynthesis of some diaminomonocarboxylic acids in nature: Formation in cyanobacteria of the neurotoxins 3-N-methyl-2,3-diaminopropanoic acid (BMAA) and 2,4-diaminobutanoic acid (2,4-DAB). Phytochemistry 144, 253-270, doi:https://doi.org/10.1016/j.phytochem.2017.09.015 (2017).

181 Nunn, P. B., O'Brien, P., Pettit, L. D. & Pyburn, S. I. Complexes of zinc, copper, and nickel with the nonprotein amino acid L-alpha-amino-beta-methylaminopropionic

acid: a naturally occurring neurotoxin. *J Inorg Biochem* **37**, 175-183, doi:10.1016/0162-0134(89)80040-6 (1989).

182 Oakley, H. B. & Young, F. G. The osmotic pressure of glycogen solutions. *The Biochemical journal* **30**, 868-876 (1936).

183 ODEQ. Northwest Regional Department of Environmental Quality memorandum on DEQ Consent Order No. WMCVC-NWR-99-09: ECSI#2409 (2011).

184 Ogawa, T. Identification and Characterization of the ictA/ndhL Gene Product Essential to Inorganic Carbon Transport of Synechocystis PCC6803. *Plant Physiology* **99**, 1604-1608, doi:10.1104/pp.99.4.1604 (1992).

185 Ohkawa, H., Pakrasi, H. B. & Ogawa, T. Two Types of Functionally Distinct NAD(P)H Dehydrogenases inSynechocystis sp. Strain PCC6803. *Journal of Biological Chemistry* **275**, 31630-31634, doi:10.1074/jbc.M003706200 (2000).

186 Oliver, R. L. & Walsby, A. E. Direct evidence for the role of light-mediated gas vesicle collapse in the buoyancy regulation of Anabaena flos-aquae (cyanobacteria)1. *Limnology and Oceanography* **29**, 879-886, doi:10.4319/lo.1984.29.4.0879 (1984).

187 Omata, T. *et al.* Identification of an ATP-binding cassette transporter involved in bicarbonate uptake in the cyanobacterium Synechococcus sp. strain PCC 7942. *Proceedings of the National Academy of Sciences* **96**, 13571-13576, doi:10.1073/pnas.96.23.13571 (1999).

188 Otten, T. G., Graham, J. L., Harris, T. D. & Dreher, T. W. Elucidation of Taste- and Odor-Producing Bacteria and Toxigenic Cyanobacteria in a Midwestern Drinking Water Supply Reservoir by Shotgun Metagenomic Analysis. *Applied and Environmental Microbiology* **82**, 5410-5420, doi:10.1128/aem.01334-16 (2016).

189 Ouellette, A. J. & Wilhelm, S. W. Toxic cyanobacteria: the evolving molecular toolbox. *Frontiers in Ecology and the Environment* **1**, 359-366, doi:10.1890/1540-9295(2003)001[0359:TCTEMT]2.0.CO;2 (2003).

190 Paerl, H. W. & Huisman, J. Blooms Like It Hot. *Science* **320**, 57-58, doi:10.1126/science.1155398 (2008).

191 Paerl, H. W. & Ustach, J. F. Blue-green algal scums: An explanation for their occurrence during freshwater blooms1. *Limnology and Oceanography* **27**, 212-217, doi:10.4319/lo.1982.27.2.0212 (1982).

192 Pané-Farré, J., Lewis, R. J. & Stülke, J. The RsbRST Stress Module in Bacteria: A Signalling System That May Interact with Different Output Modules. *Journal of Molecular Microbiology and Biotechnology* **9**, 65-76 (2005).

193 Pearson, L. A. *et al.* The genetics, biosynthesis and regulation of toxic specialized metabolites of cyanobacteria. *Harmful Algae* **54**, 98-111, doi:10.1016/j.hal.2015.11.002 (2016).

194 Peary, J. & Gorham, P. in *Journal of Phycology.* 3.

195 Peng, G. W., Gadalla, M. A., Peng, A., Smith, V. & Chiou, W. L. High-pressure liquid-chromatographic method for determination of gentamicin in plasma. *Clinical Chemistry* **23**, 1838-1844 (1977).

196 Peters, S., Koh, J. & Choi, D. Zinc selectively blocks the action of N-methyl-D-aspartate on cortical neurons. *Science* **236**, 589-593, doi:10.1126/science.2883728 (1987).

197 Pfeifer, F. in *Complex Intracellular Structures in Prokaryotes* (ed Jessup M. Shively) 115-140 (Springer Berlin Heidelberg, 2006).

198 Pfeifer, F. Distribution, formation and regulation of gas vesicles. *Nature Reviews Microbiology* **10**, 705, doi:10.1038/nrmicro2834 (2012).

199 Pfammatter, E. & Seebach, D. Preparation of (R)- and (S)-2-alkyl-2-amino-3-(methylamino)propanoic and other 2,3-diaminoalkanoic acid derivatives from a chiral imidazoline. *Liebigs Annalen der Chemie* 1991, 1323-1336, doi:10.1002/jlac.1991199101227 (1991).

200 Phillips, G. N., Jr. Construction of an atomic model for tropomyosin and implications for interactions with actin. J Mol Biol 192, 128-131 (1986).

201 Pierangelini, M. *et al.* Constitutive Cylindrospermopsin Pool Size in Cylindrospermopsis raciborskii under Different Light and CO2 Partial Pressure Conditions. *Applied and Environmental Microbiology* **81**, 3069-3076, doi:10.1128/aem.03556-14 (2015).

202 Pip, E., Munford, K. & Bowman, L. Seasonal Nearshore Occurrence of the Neurotoxin β N methylamino L alanine (BMAA) in Lake Winnipeg, Canada. *Environment and Pollution* **5**, 110, doi:10.5539/ep.v5n1p110 (2016).

203 Pomati, F., Rossetti, C., Manarolla, G., Burns, B. P. & Neilan, B. A. Interactions between intracellular Na+ levels and saxitoxin production in Cylindrospermopsis raciborskii T3. *Microbiology* **150**, 455-461, doi:10.1099/mic.0.26350-0 (2004).

204 Popova, A. A., Rasmussen, U., Semashko, T. A., Govorun, V. M. & Koksharova, O. A. Stress effects of cyanotoxin β-methylamino-L-alanine (BMAA) on cyanobacterial heterocyst formation and functionality. Environmental Microbiology Reports 10, 369-377, doi:doi:10.1111/1758-2229.12647 (2018).

205 Price, G. D., Badger, M. R., Woodger, F. J. & Long, B. M. Advances in understanding the cyanobacterial CO2-concentrating-mechanism (CCM): functional components, Ci transporters, diversity, genetic regulation and prospects for engineering into plants. *J Exp Bot* **59**, 1441-1461, doi:10.1093/jxb/erm112 (2008).

206 Price, G. D., Woodger, F. J., Badger, M. R., Howitt, S. M. & Tucker, L. Identification of a SulP-type bicarbonate transporter in marine cyanobacteria. *Proceedings of the National Academy of Sciences* **101**, 18228-18233, doi:10.1073/pnas.0405211101 (2004).

207 Puente-Sánchez, F. *et al.* Viable cyanobacteria in the deep continental subsurface. *Proceedings of the National Academy of Sciences* **115**, 10702-10707, doi:10.1073/pnas.1808176115 (2018).

208 PyMol. The PyMOL Molecular Graphics System, Version 2.0 Schrödinger, LLC (2019).

209 Ramsay, J. P., Williamson, N. R., Spring, D. R. & Salmond, G. P. C. A quorum-sensing molecule acts as a morphogen controlling gas vesicle organelle biogenesis and adaptive flotation in an enterobacterium. *Proceedings of the National Academy of Sciences* **108**, 14932-14937, doi:10.1073/pnas.1109169108 (2011).

210 Rantala, A. *et al.* Phylogenetic evidence for the early evolution of microcystin synthesis. *Proc Natl Acad Sci U S A* **101**, 568-573, doi:10.1073/pnas.0304489101 (2004).

211 Rantala-Ylinen, A. *et al.* Anatoxin-a synthetase gene cluster of the cyanobacterium Anabaena sp. strain 37 and molecular methods to detect potential producers. *Appl Environ Microbiol* **77**, 7271-7278, doi:10.1128/AEM.06022-11 (2011).

212 Reed, R. H. & Walsby, A. E. Changes in turgor pressure in response to increases in external NaCl concentration in the gas-vacuolate cyanobacterium Microcystis sp. *Archives of Microbiology* **143**, 290-296, doi:10.1007/bf00411252 (1985).

213 Rehman, A. U., Cser, K., Sass, L. & Vass, I. Characterization of singlet oxygen production and its involvement in photodamage of Photosystem II in the cyanobacterium Synechocystis PCC 6803 by histidine-mediated chemical trapping. Biochim Biophys Acta 1827, 689-698, doi:10.1016/j.bbabio.2013.02.016 (2013).

214 Reynolds, C. S., Oliver, R. L. & Walsby, A. E. Cyanobacterial dominance: The role of buoyancy regulation in dynamic lake environments. *New Zealand Journal of Marine and Freshwater Research* **21**, 379-390, doi:10.1080/00288330.1987.9516234 (1987).

215 RHESSI. 2019. Reuven Ramaty High Energy Solar Spectroscopic Imager. Goddard Space Flight Center, Greenbelt, MD, USA. National Aeronautics and Space Administration.

216 Rivière, M.-E. *et al.* in *Methods in Enzymology* Vol. 167 691-700 (Academic Press, 1988).

217 Roche, S., Rey, F. A., Gaudin, Y. & Bressanelli, S. Structure of the Prefusion Form of the Vesicular Stomatitis Virus Glycoprotein G. *Science* **315**, 843-848, doi:10.1126/science.1135710 (2007).

218 Rogers, R. S. & Rapoport, H. The pKa's of saxitoxin. *Journal of the American Chemical Society* **102**, 7335-7339, doi:10.1021/ja00544a030 (1980).

219 Rohrlack, T., Christiansen, G. & Kurmayer, R. Putative antiparasite defensive system involving ribosomal and nonribosomal oligopeptides in cyanobacteria of the genus

Planktothrix. *Appl Environ Microbiol* **79**, 2642-2647, doi:10.1128/AEM.03499-12 (2013).

220 Rojas, E. R. & Huang, K. C. Regulation of microbial growth by turgor pressure. *Current Opinion in Microbiology* **42**, 62-70, doi:10.1016/j.mib.2017.10.015 (2018).

221 Rose, K. C., Neale, P. J., Tzortziou, M., Gallegos, C. L. & Jordan, T. E. Patterns of spectral, spatial, and long-term variability in light attenuation in an optically complex sub-estuary. *Limnology and Oceanography* **0**, doi:10.1002/lno.11005 (2018).

222 Rosén, J. & Hellenäs, K.-E. Determination of the neurotoxin BMAA (β-N-methylamino-l-alanine) in cycad seed and cyanobacteria by LC-MS/MS (liquid chromatography tandem mass spectrometry). *Analyst* **133**, 1785-1789, doi:10.1039/B809231A (2008).

223 Rosén, J., Westerberg, E., Schmiedt, S. & Hellenäs, K.-E. BMAA detected as neither free nor protein bound amino acid in blue mussels. *Toxicon* **109**, 45-50, doi:10.1016/j.toxicon.2015.11.008 (2016).

224 Roy-Lachapelle, A., Solliec, M. & Sauve, S. Determination of BMAA and three alkaloid cyanotoxins in lake water using dansyl chloride derivatization and high-resolution mass spectrometry. *Anal Bioanal Chem* **407**, 5487-5501, doi:10.1007/s00216-015-8722-2 (2015).

225 Rumbaugh, K. P. Convergence of hormones and autoinducers at the host/pathogen interface. *Anal Bioanal Chem* **387**, 425-435, doi:10.1007/s00216-006-0694-9 (2007).

226 Runnegar, M., Berndt, N., Kong, S. M., Lee, E. Y. C. & Zhang, L. F. In Vivo and in Vitro Binding of Microcystin to Protein Phosphatase 1 and 2A. *Biochemical and*

Biophysical Research Communications **216**, 162-169, doi:10.1006/bbrc.1995.2605 (1995).

227 Sader, M. Turbidity instrumentation-an overview of today's available technology. *Turbidity and Other Sediment Surrogates* (2002).

228 Saier, J., Milton H. Families of transmembrane transporters selective for amino acids and their derivatives. *Microbiology* **146**, 1775-1795, doi:10.1099/00221287-146-8-1775 (2000).

229 Sakai, N. & Ohfune, Y. Total synthesis of galantin I. Acid-catalyzed cyclization of galantinic acid. Journal of the American Chemical Society 114, 998-1010, doi:10.1021/ja00029a031 (1992).

230 Salomonsson, L., Hansson, A. & Bondesson, U. Development and in-house validation of a method for quantification of BMAA in mussels using dansyl chloride derivatization and ultra performance liquid chromatography tandem mass spectrometry. *Analytical Methods* **5**, 4865-4874, doi:10.1039/C3AY40657A (2013).

231 Santer, B. D. *et al.* Celebrating the anniversary of three key events in climate change science. *Nature Climate Change* **9**, 180-182, doi:10.1038/s41558-019-0424-x (2019).

232 Schell, M. A. Molecular Biology of the LysR Family of Transcriptional Regulators. *Annual Review of Microbiology* **47**, 597-626, doi:10.1146/annurev.mi.47.100193.003121 (1993).

233 Schirrmeister, B. E., de Vos, J. M., Antonelli, A. & Bagheri, H. C. Evolution of multicellularity coincided with increased diversification of cyanobacteria and the Great Oxidation Event. *Proc Natl Acad Sci U S A* **110**, 1791-1796, doi:10.1073/pnas.1209927110 (2012).

234 Schirrmeister, B. E., Gugger, M. & Donoghue, P. C. Cyanobacteria and the Great Oxidation Event: evidence from genes and fossils. *Palaeontology* **58**, 769-785, doi:10.1111/pala.12178 (2015).

235 Schladitz, C., Vieira, E. P., Hermel, H. & Möhwald, H. Amyloid–β-Sheet Formation at the Air-Water Interface. *Biophysical Journal* **77**, 3305-3310, doi:10.1016/S0006-3495(99)77161-4 (1999).

236 Schwarz, R. & Grossman, A. R. A response regulator of cyanobacteria integrates diverse environmental signals and is critical for survival under extreme conditions. Proceedings of the National Academy of Sciences 95, 11008-11013 (1998).

237 Scott, C. et al. Tracing the stepwise oxygenation of the Proterozoic ocean. Nature 452, 456-459, doi:10.1038/nature06811 (2008).

238 Scott, L. L. & Downing, T. G. A Single Neonatal Exposure to BMAA in a Rat Model Produces Neuropathology Consistent with Neurodegenerative Diseases. *Toxins* **10**, 22, doi:10.3390/toxins10010022 (2018).

239 Seebach, D., Studer, A., Pfammatter, E. & Widmer, H. Synthesis of Tri-, Penta-, and Heptapeptides Containing and (R)-2-alkyl-2-amino-3-(methylamino)-propionic acid residue in the central position. *Helvetica Chimica Acta* **77**, 2035-2050, doi:10.1002/hlca.19940770728 (1994).

240 Shalev-Malul, G. *et al.* An AbrB-like protein might be involved in the regulation of cylindrospermopsin production by Aphanizomenon ovalisporum. *Environmental Microbiology* **10**, 988-999, doi:10.1111/j.1462-2920.2007.01519.x (2008).

241 Shapiro, J. The role of carbon dioxide in the initiation and maintenance of blue-green dominance in lakes. *Freshwater Biology* **37**, 307-323, doi:10.1046/j.1365-2427.1997.00164.x (1997).

242 Sharma, A. K., Rigby, A. C. & Alper, S. L. STAS domain structure and function. *Cellular physiology and biochemistry : international journal of experimental cellular physiology, biochemistry, and pharmacology* **28**, 407-422, doi:10.1159/000335104 (2011).

243 Shelden, M. C., Howitt, S. M. & Price, G. D. Membrane topology of the cyanobacterial bicarbonate transporter, BicA, a member of the SulP (SLC26A) family. *Molecular Membrane Biology* **27**, 12-22, doi:10.3109/09687680903400120 (2010).

244 Shibata, M. *et al.* Genes Essential to Sodium-dependent Bicarbonate Transport in Cyanobacteria: Function and Phylogenetic Analysis. *Journal of Biological Chemistry* **277**, 18658-18664, doi:10.1074/jbc.M112468200 (2002).

245 Shibata, M. *et al.* Distinct constitutive and low-CO2-induced CO2 uptake systems in cyanobacteria: genes involved and their phylogenetic relationship with homologous genes in other organisms. *Proc Natl Acad Sci U S A* **98**, 11789-11794, doi:10.1073/pnas.191258298 (2001).

246 Silaev, A. B., Baratova, L. A. & Katrukha, G. S. Quantitative determination of alpha- and gamma-2,4-dinitrophenyl-isomers of alpha,gamma-diaminobutyric acid with an automatic amino acid analyzer as a method of studying N-alpha--N-gamma migration in peptides of alpha,gamma-diaminobutyric acid and polymyxin M. *Journal of chromatography* 24, 61-67 (1966).

247 Sinha, R. P., Singh, S. P. & Häder, D.-P. Database on mycosporines and mycosporine-like amino acids (MAAs) in fungi, cyanobacteria, macroalgae, phytoplankton and animals. *Journal of Photochemistry and Photobiology B: Biology* **89**, 29-35, doi:10.1016/j.jphotobiol.2007.07.006 (2007).

248 Sivertsen, A. C., Bayro, M. J., Belenky, M., Griffin, R. G. & Herzfeld, J. Solid-State NMR Evidence for Inequivalent GvpA Subunits in Gas Vesicles. *Journal of Molecular Biology* **387**, 1032-1039, doi:10.1016/j.jmb.2009.02.015 (2009).

249 Sivertsen, A. C., Bayro, M. J., Belenky, M., Griffin, R. G. & Herzfeld, J. Solid-State NMR Characterization of Gas Vesicle Structure. *Biophysical Journal* **99**, 1932-1939, doi:10.1016/j.bpj.2010.06.041 (2010).

250 Smith, K. S., Cosper, N. J., Stalhandske, C., Scott, R. A. & Ferry, J. G. Structural and Kinetic Characterization of an Archaeal β-Class Carbonic Anhydrase. *Journal of Bacteriology* **182**, 6605-6613, doi:10.1128/jb.182.23.6605-6613.2000 (2000).

251 Soto-Liebe, K. *et al.* Reassessment of the toxin profile of Cylindrospermopsis raciborskii T3 and function of putative sulfotransferases in synthesis of sulfated and sulfonated PSP toxins. *Toxicon* **56**, 1350-1361, doi:10.1016/j.toxicon.2010.07.022 (2010).

252 Spencer, P. S. et al. Guam amyotrophic lateral sclerosis-parkinsonism-dementia linked to a plant excitant neurotoxin. Science 237, 517-522 (1987).

253 Spencer, P. S., Palmer, V. S. & Ludolph, A. C. On the decline and etiology of high-incidence motor system disease in West Papua (southwest New Guinea). *Mov Disord* **20**, S119-126, doi:10.1002/mds.20552 (2005).

254 Steffen, M. M. *et al.* Metatranscriptomic evidence for co-occurring top-down and bottom-up controls on toxic cyanobacterial communities. *Appl Environ Microbiol* **81**, 3268-3276, doi:10.1128/AEM.04101-14 (2015).

255 Sterner, R. W. in *Plankton Ecology: Succession in Plankton Communities* (ed Ulrich Sommer) 107-170 (Springer Berlin Heidelberg, 1989).

256 Strichartz, G. Structural determinants of the affinity of saxitoxin for neuronal sodium channels. Electrophysiological studies on frog peripheral nerve. *The Journal of General Physiology* **84**, 281-305, doi:10.1085/jgp.84.2.281 (1984).

257 Strunk, T. *et al.* Structural model of the gas vesicle protein GvpA and analysis of GvpA mutants in vivo. *Molecular Microbiology* **81**, 56-68, doi:10.1111/j.1365-2958.2011.07669.x (2011).

258 Stucken, K. *et al.* The smallest known genomes of multicellular and toxic cyanobacteria: comparison, minimal gene sets for linked traits and the evolutionary implications. *PLoS One* **5**, e9235, doi:10.1371/journal.pone.0009235 (2010).

259 Sültemeyer, D., Klughammer, B., Badger, M. R. & Dean Price, G. Fast Induction of High-Affinity HCO(3)(−) Transport in Cyanobacteria. *Plant Physiology* **116**, 183-192 (1998).

260 Sundararajan, A. & Ju, L.-K. Glutaraldehyde Treatment of Proteinaceous Gas Vesicles from Cyanobacterium Anabaenaflos-aquae. *Biotechnology Progress* **16**, 1124-1128, doi:10.1021/bp000123n (2000).

261 Takada, H., Esaki, N., Tanaka, H. & Soda, K. The C3-N Bond Cleavage of 2-Amino-3-(N-substituted-amino)-propionic Acids Catalyzed byl-Methionine γ-Lyase.

Agricultural and Biological Chemistry **52**, 2897-2901, doi:10.1080/00021369.1988.10869133 (2014).

262 Talling, J. The depletion of carbon dioxide from lake water by phytoplankton. *The Journal of Ecology*, 79-121 (1976).

263 Tan, Z. S. *et al.* Thyroid function and the risk of Alzheimer disease: the Framingham Study. *Archives of internal medicine* **168**, 1514-1520, doi:10.1001/archinte.168.14.1514 (2008).

264 Tang, X. *et al.* Seasonal Gene Expression and the Ecophysiological Implications of Toxic Microcystis aeruginosa Blooms in Lake Taihu. *Environmental Science & Technology* **52**, 11049-11059, doi:10.1021/acs.est.8b01066 (2018).

265 Te, S. H., Chen, E. Y. & Gin, K. Y.-H. Comparison of Quantitative PCR and Droplet Digital PCR Multiplex Assays for Two Genera of Bloom-Forming Cyanobacteria, Cylindrospermopsis and Microcystis. *Applied and Environmental Microbiology* **81**, 5203-5211, doi:10.1128/aem.00931-15 (2015).

266 Tuinstra, R. L. *et al.* Interconversion between two unrelated protein folds in the lymphotactin native state. *Proceedings of the National Academy of Sciences* **105**, 5057-5062, doi:10.1073/pnas.0709518105 (2008).

267 USEPA. 2016. Contaminant Information Sheets (CISs) for the Final Fourth Contaminant Candidate List (CCL 4). EPA 815-R-16-003.

268 Van de Waal, D. B. *et al.* Reversal in competitive dominance of a toxic versus non-toxic cyanobacterium in response to rising CO2. *ISME J* **5**, 1438-1450, doi:10.1038/ismej.2011.28 (2011).

269 Van de Waal, D. B. *et al.* Reversal in competitive dominance of a toxic versus non-toxic cyanobacterium in response to rising CO2. *The Isme Journal* **5**, 1438, doi:10.1038/ismej.2011.28 (2011).

270 van Keulen, G. in *Complex Intracellular Structures in Prokaryotes* (ed Jessup M. Shively) 349-357 (Springer Berlin Heidelberg, 2006).

271 van Onselen, R. & Downing, T. G. BMAA-protein interactions: A possible new mechanism of toxicity. *Toxicon* **143**, 74-80, doi:10.1016/j.toxicon.2018.01.011 (2018).

272 Vázquez-Bermúdez, M. a. F., Herrero, A. & Flores, E. 2-Oxoglutarate increases the binding affinity of the NtcA (nitrogen control) transcription factor for the Synechococcus glnA promoter. *FEBS Letters* **512**, 71-74, doi:10.1016/S0014-5793(02)02219-6 (2002).

273 Walker, J. E., Hayes, P. K. & Walsby, A. E. Homology of Gas Vesicle Proteins in Cyanobacteria and Halobacteria. *Microbiology* **130**, 2709-2715, doi:10.1099/00221287-130-10-2709 (1984).

274 Walsby, A. E. The pressure relationships of gas vacuoles. *Proceedings of the Royal Society of London. Series B. Biological Sciences* **178**, 301-326, doi:10.1098/rspb.1971.0067 (1971).

275 Walsby, A. E. A portable apparatus for measuring relative gas vacuolation, the strength of gas vacuoles, and turgor pressure in planktonic blue-green algae and bacteria1. *Limnology and Oceanography* **18**, 653-658, doi:10.4319/lo.1973.18.4.0653 (1973).

276 Walsby, A. E. Water relations of gas-vacuolate prokaryotes. *Proceedings of the Royal Society of London. Series B. Biological Sciences* **208**, 73-102, doi:10.1098/rspb.1980.0043 (1980).

277 Walsby, A. E. Gas vesicles. *Microbiological Reviews* **58**, 94-144 (1994).

278 Walsby, A. E. & Bleything, A. The Dimensions of Cyanobacterial Gas Vesicles in Relation to Their Efficiency in Providing Buoyancy and Withstanding Pressure. *Microbiology* **134**, 2635-2645, doi:10.1099/00221287-134-10-2635 (1988).

279 Walter, J. M. *et al.* Ecogenomics and Taxonomy of Cyanobacteria Phylum. *Frontiers in microbiology* **8**, 2132-2132, doi:10.3389/fmicb.2017.02132 (2017).

280 Watanabe, S. *et al.* Light-dependent and asynchronous replication of cyanobacterial multi-copy chromosomes. *Molecular Microbiology* **83**, 856-865, doi:10.1111/j.1365-2958.2012.07971.x (2012).

281 Waterhouse, A. M., Martin, D. M. A., Barton, G. J., Procter, J. B. & Clamp, M. Jalview Version 2—a multiple sequence alignment editor and analysis workbench. Bioinformatics 25, 1189-1191, doi:10.1093/bioinformatics/btp033 (2009).

282 Watson, G. M. F. & Tabita, F. R. Microbial ribulose 1,5-bisphosphate carboxylase/oxygenase: a molecule for phylogenetic and enzymological investigation. *FEMS Microbiology Letters* **146**, 13-22, doi:10.1111/j.1574-6968.1997.tb10165.x (1997).

283 Weissman, K. J. The structural biology of biosynthetic megaenzymes. *Nature Chemical Biology* **11**, 660, doi:10.1038/nchembio.1883 (2015).

284 Welker, M. & von Dohren, H. Cyanobacterial peptides - nature's own combinatorial biosynthesis. *FEMS Microbiol Rev* **30**, 530-563, doi:10.1111/j.1574-6976.2006.00022.x (2006).

285 Whatmore, A. M. & Reed, R. H. Determination of turgor pressure in Bacillus subtilis: a possible role for K+ in turgor regulation. *Microbiology* **136**, 2521-2526, doi:10.1099/00221287-136-12-2521 (1990).

286 Whitney, S. M., Houtz, R. L. & Alonso, H. Advancing Our Understanding and Capacity to Engineer Nature's CO₂-Sequestering Enzyme, Rubisco. *Plant Physiology* **155**, 27-35, doi:10.1104/pp.110.164814 (2011).

287 Wiese, M., D'Agostino, P. M., Mihali, T. K., Moffitt, M. C. & Neilan, B. A. Neurotoxic Alkaloids: Saxitoxin and Its Analogs. *Marine Drugs* **8**, 2185 (2010).

288 Wilbanks, E. G. *et al.* The Green Berry Consortia of the Sippewissett Salt Marsh: Millimeter-Sized Aggregates of Diazotrophic Unicellular Cyanobacteria. *Frontiers in Microbiology* **8**, doi:10.3389/fmicb.2017.01623 (2017).

289 Wood, J. M. Bacterial responses to osmotic challenges. *The Journal of General Physiology* **145**, 381-388, doi:10.1085/jgp.201411296 (2015).

290 Woodger, F. J., Badger, M. R. & Price, G. D. Sensing of inorganic carbon limitation in Synechococcus PCC7942 is correlated with the size of the internal inorganic carbon pool and involves oxygen. *Plant Physiol* **139**, 1959-1969, doi:10.1104/pp.105.069146 (2005).

291 Woodger, F. J., Bryant, D. A. & Price, G. D. Transcriptional regulation of the CO2-concentrating mechanism in a euryhaline, coastal marine cyanobacterium,

Synechococcus sp. Strain PCC 7002: role of NdhR/CcmR. *J Bacteriol* **189**, 3335-3347, doi:10.1128/JB.01745-06 (2007).

292 Xiao, M.-Y., Gustafsson, B. & Niu, Y.-P. Metabotropic Glutamate Receptors in the Trafficking of Ionotropic Glutamate and GABA(A) Receptors at Central Synapses. *Current Neuropharmacology* **4**, 77-86 (2006).

293 Yang, J. & Zhang, Y. Protein Structure and Function Prediction Using I-TASSER. Current protocols in bioinformatics 52, 5.8.1-5.8.15, doi:10.1002/0471250953.bi0508s52 (2015).

294 Yosuke, T., Monson, R. E., Ramsay, J. P. & Salmond, G. P. C. Molecular genetic and physical analysis of gas vesicles in buoyant enterobacteria. *Environmental Microbiology* **18**, 1264-1276, doi:10.1111/1462-2920.13203 (2016).

295 Zhang, P. *et al.* Expression and functional roles of the two distinct NDH-1 complexes and the carbon acquisition complex NdhD3/NdhF3/CupA/Sll1735 in Synechocystis sp PCC 6803. *Plant Cell* **16**, 3326-3340, doi:10.1105/tpc.104.026526 (2004).

296 Zilliges, Y. *et al.* The cyanobacterial hepatotoxin microcystin binds to proteins and increases the fitness of microcystis under oxidative stress conditions. *PLoS One* **6**, e17615, doi:10.1371/journal.pone.0017615 (2011).

297 Zimmer, R. K. & Ferrer, R. P. Neuroecology, Chemical Defense, and the Keystone Species Concept. *Biological Bulletin* **213**, 208-225, doi:10.2307/25066641 (2007).

298 Zimmerman, D., Goto, J. J. & Krishnan, V. V. Equilibrium Dynamics of beta-N-Methylamino-L-Alanine (BMAA) and Its Carbamate Adducts at Physiological Conditions. *PLoS One* **11**, e0160491, doi:10.1371/journal.pone.0160491 (2016).

299 Zimmerman, D., Goto, J. J. & Krishnan, V. V. Equilibrium Dynamics of β-N-Methylamino-L-Alanine (BMAA) and Its Carbamate Adducts at Physiological Conditions. *PloS one* **11**, e0160491-e0160491, doi:10.1371/journal.pone.0160491 (2016).

300 Zoltewicz, J. A. & Kandetzki, P. E. Kinetics and mechanism of hydrogen-deuterium exchange in the methyl groups of pyridines in dilute aqueous acid. Factors influencing the degree of catalysis. *Journal of the American Chemical Society* **93**, 6562-6567, doi:10.1021/ja00753a039 (1971).